APPEARANCE POTENTIAL SPECTROSCOPY OF LAYER MATERIALS

by

Christopher Webb

A thesis submitted for the degree of
Doctor of Philosophy, University of London

Department of Chemical Engineering and Chemical Technology,
Imperial College, London

October, 1975

To my Mother and Father

ACKNOWLEDGEMENTS

For the supply of crystals I am very grateful to: Dr. A.W. Moore (Union Carbide), Dr. F. Levy (Ecole Polytechnique, Lausanne), Dr. A.H. Thompson (Exxon Research, New Jersey), Dr. A.D. Yoffe (Cavendish Laboratory, Cambridge) and Dr. R.H. Williams (School of Physical Sciences, Coleraine).

It is a pleasure also to thank all those friends and colleagues who have contributed in any way to this work. In particular my thanks are due to Mrs. B.A. Robinson for aid with electron microscopy, Mr. R. Wood for help and advice in all electronic matters, Dr. P.J. Page who devised the MCS computer programme, Dr. P.J. Statham for some useful comments on deconvolution and Miss S.F. Tolley for her patient preparation of the typescript. Most of all I am indebted to Dr. P.M. Williams, my supervisor, whose help and guidance throughout the last three years have been invaluable.

Finally I thank the Science Research Council for financial support.

ERRATA

Page	Line	
8	24	proportional
10	26	VIG 21
19	7	producing
22	10	having
36	18	as that in XPS
37	12	analysis
58	14	Redhead
58	29	than Sn
66	11	general
66	19	small
66	20	errors
72	21	An
82	20	spectra
82	30	were
112	3	Sonntag
153	17	read 'striking' for 'spectacular'

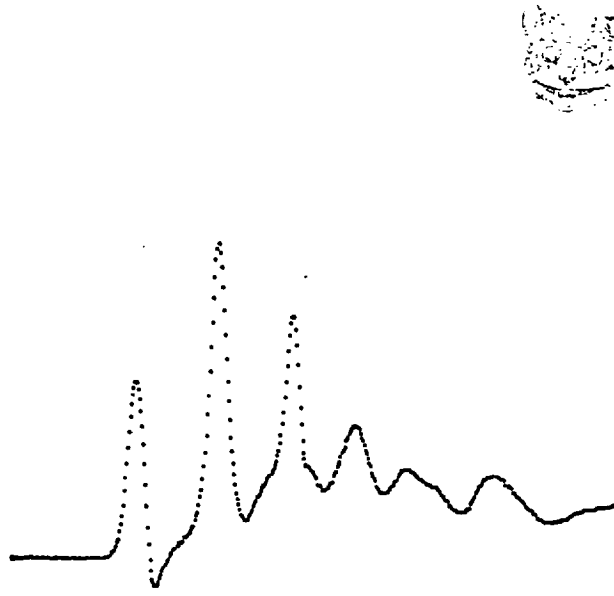

I wish (said Alice) you wouldn't *keep on* appearing ....

ABSTRACT

Appearance Potential Spectroscopy has been applied to a study of a number of materials having layered structures. Complex and varied spectra have been found generally explicable in terms of a conduction band self-convolution model, as previously proposed. Basic ideas on deconvolution are discussed and a method which has been devised is shown to be very useful in interpreting AP spectra, enabling information relating to the conduction band density of states to be derived.

Crystal field splitting of d orbitals, particularly in octahedrally co-ordinated transition metal dichalcogenides, gives rise to strong effects in AP spectra, consistent with a self-convolution interpretation. The sub-band separation in a number of compounds has been determined and, for TiS_2, where other experimental data are available, excellent agreement is found.

A similarly-based interpretation is successfully applied in correlating the remarkable graphite spectrum with experimental data from other techniques and arriving at a form for the conduction band d.o.s. in graphite which is in qualitative accord with the band scheme of Painter and Ellis. Previous APS studies of graphite, involving lower resolution, had invoked a simple plasmon coupling argument to explain the results. A comparison with the isoelectronic and isostructural boron nitride is useful in demonstrating the inapplicability of such an interpretation.

CONTENTS

CHAPTER 1

INTRODUCTION

In its most usual form the technique of Appearance Potential Spectroscopy (APS) involves the irradiation of a surface with electrons and the detection of the total soft X-ray yield (I) as a function of the incident electron energy (E_1). The advent of variations on this theme (see section 4.2) has led to the increasing use of 'Soft X-ray Appearance Potential Spectroscopy' (SXAPS) in describing the type of experiment referred to above.

The basic concept of measuring the 'critical potentials' for atomic excitations to occur these being signalled by the 'appearance' of characteristic decay products, can be traced back to the well known experiment of Franck and Hertz. Their work was on gases, but the extension to the solid state attracted the attention of a number of workers[1] in the 1920's; these early experiments were, however, fraught with difficulties. The subtle changes in the X-ray yield curve, $I(E_1)$, occurring at the critical potentials were difficult to detect experimentally due to the large background of bremsstrahlung radiation. Moreover, the extreme surface sensitivity and the required degree of surface cleanliness were not appreciated, leading to an abundance of critical potentials which was found 'bewildering'. An idea of the extent of the early problems is given in a paper[2] by C.H. Thomas in 1925 who resumed observations on iron 'since spring weather conditions interfered with earlier work on this metal'. One noteworthy effort, however, was by Skinner[3] who not only recognised the value of differentiating (by graphical

means) the $I(E_1)$ curve, but also prepared his lithium sample by in situ evaporation.

Nonetheless, the method lost favour, and it was not until a few years ago that Park, Houston and Schreiner[4] demonstrated that the potential modulation technique could be applied to obtain the derivative spectrum direct, with dramatic enhancement of the small, but sharp, changes that occur at the thresholds for exciting core electrons. Refinements of their original design both in respect of the in vacuum arrangement[5,6] and the exterior electronics[7] swiftly followed. Interest immediately focussed, not so much on the numerical values of the 'critical' or 'appearance' potentials, but on the detailed shape of the dI/dE_1 spectrum at and above threshold. This was shown[8] to depend upon the chemical environment of the atoms and it was proposed on the basis of a simple one electron model that the observed derivative spectrum could be taken to represent the derivative of the self-convoluted one-electron density of states above the Fermi level. The self-convolution arises because two electrons, both the incident and excited core, must be accommodated in the unfilled states above the Fermi level (see figure 1a).

Appearance Potential Spectroscopy thus provides yet another method that can be used to obtain information related to electronic energy band structures which are of central importance in understanding the physical behaviour of solids. The self-convolution model, however, represents a somewhat idealised situation. It neglects the fact that APS probes only the outermost few atomic layers of a solid where electronic states may differ significantly from those in the 'bulk'. It must also be borne in mind that because excitations occur from localised core electrons it is a 'local' density of states as seen by the core electron which is measured. While this really serves only to complicate the comparison of APS results with theory

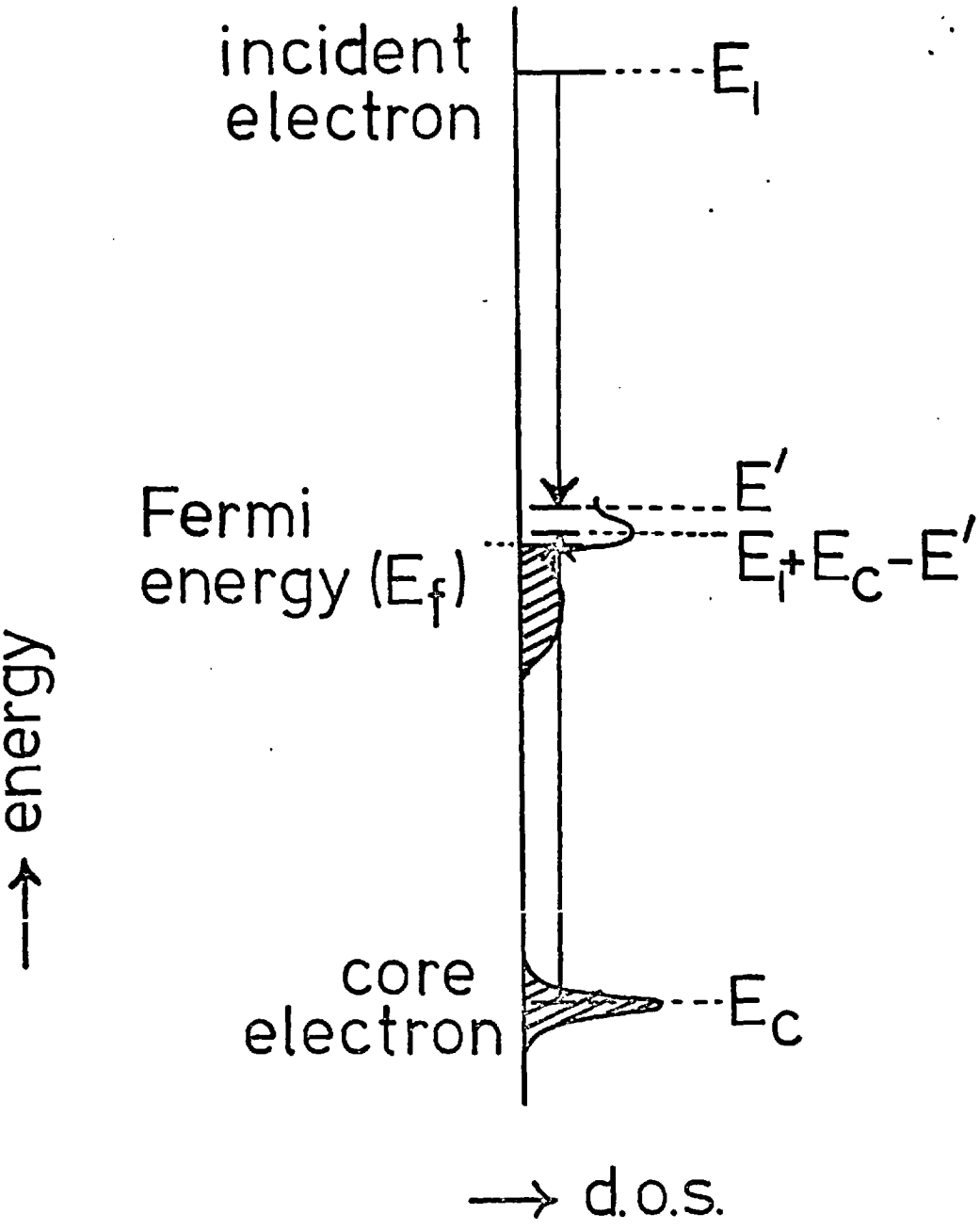

excitation rate

$$\propto \int_{E_f}^{E+E_C} N(E')N(E_I+E_C-E')dE'$$

1a

for a monatomic solid such as graphite it also means that information is available specific to the local environment of each atomic species in the case of compounds. This is also true of gases adsorbed on solid surfaces where advantage may also be taken of the surface sensitivity of APS in applying it to such systems with their relevance to an understanding of catalytic behaviour.

However, two or three years ago, when this work was beginning, the self-convolution interpretation was largely conjectural. Theoreticians suggested[9,10,11] that many electron effects may also influence the threshold shape but said little to indicate the extent to which such processes are important. At this time experiment seems more likely to answer this question. In layer materials the inherent two dimensional nature (as well as the atomic co-ordination type in layered compounds) may lead to splittings of energy bands; they thus represent ideal materials for study since the sharp features expected in the conduction band densities of states may be compared with APS observations. The two dimensional character also tends to nullify the role of the surface sensitivity of APS. While interest in graphite, probably the best known of all layer materials, continues, considerable interest[12,13] has been aroused during the last few years in the layered transition metal dichalcogenides. These materials thus provided the natural targets for study with the knowledge that any information on their band structures which may be gleaned would be of considerable interest to other workers concerned with their properties.

In the chapters that follow a description of the experimental arrangement and an informal discussion of the theory is given. Some of the other work in the field of APS is reviewed and then the problems involved in numerical deconvolution considered. Finally the results that have been obtained are presented and discussed.

CHAPTER 2

EXPERIMENTAL

Much of the effort in achieving a satisfactory experimental arrangement was expended during an M.Sc. project[14]. A number of modifications to the details have since been made as well as a link-up to the existing PDP8-based data handling facilities. The set-up used in obtaining the present results is described below and a complete block diagram given in figure 2a.

Electrons are thermionically emitted from a filament at constant potential ($\sim$ 20 volts w.r.t. earth) and attracted to the positively biased sample placed 2-3 mms. away; the magnitude of the sample potential thus determines the incident electron energy. A simple feedback device[15] holds the emission current constant. The resulting X-rays are detected by means of a photocathode arrangement, the ejected photoelectrons being picked up on the positively biased collector wire.

2.1 Potential Modulation

Superimposed on the sample potential is a small oscillatory voltage which also supplies the lock-in amplifier with a reference frequency. The mode of action of the lock-in amplifier is to give an analogue output voltage proportional to the amplitude of this frequency component in the applied signal. This gives a direct measure of the first derivative of the yield as is illustrated in figure 2b. Harmonics of the reference frequency give an approximate measure of higher derivatives[14], but these have not been utilised to any extent in

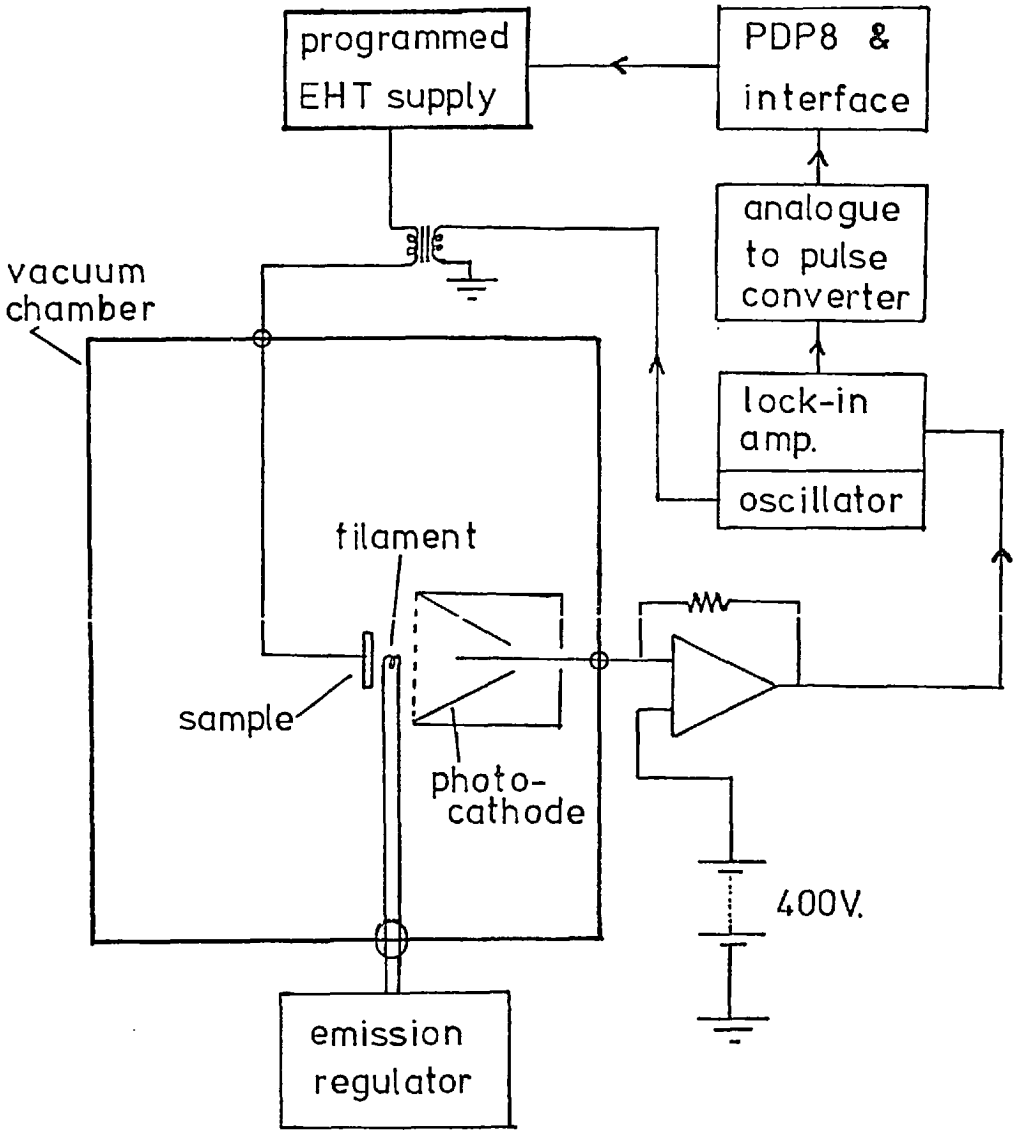

SXAPS block diagram

2a

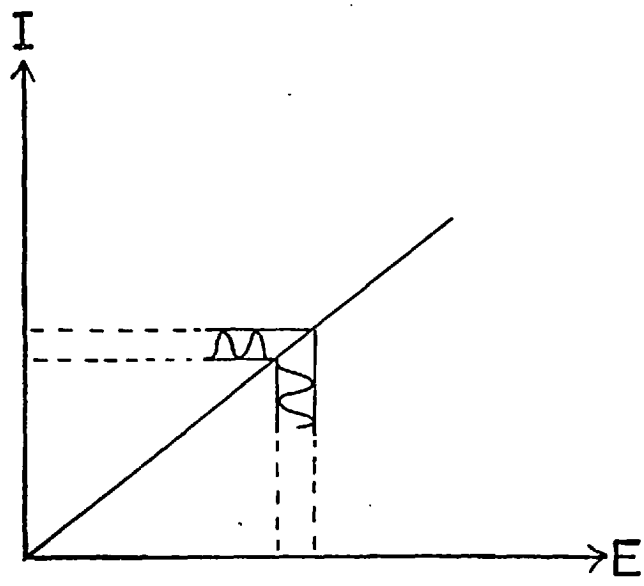

2b Potential modulation

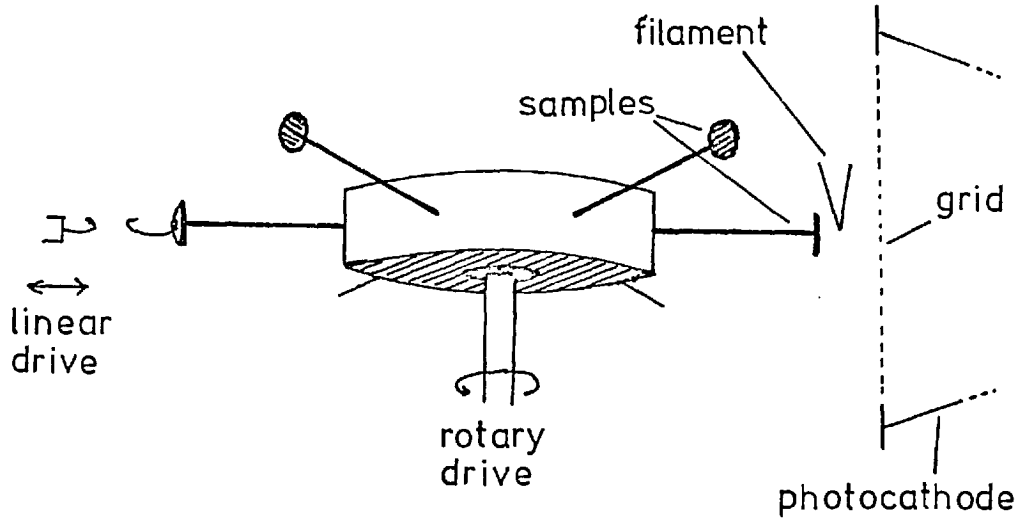

2c Vacuum components

the present work.

2.2 Vacuum Components

The in-vacuum part is shown in figure 2c. The sample holder is mounted on to a rotary motion drive feedthrough whose axis is horizontal and perpendicular to that of the spectrometer tube. Samples are mounted on to tungsten or molybdenum rods (∿ 30 mms. long) and screwed to a stainless steel cylinder (diameter approximately 40 mms. and thickness 12 mms.) co-axial with and electrically isolated from the rotary drive. This enables any of six samples to be positioned adjacent to the filament which has a centrally thinned region to localise electron emission. The operating voltage across the filament assembly was measured to be 0.94 volts. It should be noted that this figure would represent the maximum full-width of the energy distribution in the electron beam, if the thermal energy distribution (∿ 0.2-0.3 eV) is insignificant. It thus seems likely that the two effects are comparable (see also section 2.7), and the resolution is near the limit imposed by the temperature of the tungsten filament.

A 'micromesh' earthed grid separates the filament from the photocathode and prevents electrons passing direct from filament to collector. The photocathode consists of a nickel cone coated with KCl to increase the photo-yield (by a factor ∿ 10), and the photo-emitted electrons are collected on the positively biased (∿ 400 volts) central tungsten rod. Since the noise limitation of the device is shot noise in the collector current the S/N ratio is proportioned to the square root of the collector current, and a high photo-yield is thus desirable. An electron multiplier serves no purpose provided noise contributed by exterior electronics is less than this shot noise.

One difficulty encountered during early experiments was that

the KCl photocathode rapidly contaminated with an accompanying reduction of signal. This was overcome by the introduction of a shutter which was attached by means of a pivot to the photocathode housing. A thin copper wire, attached to the shutter, was passed over a suitable fixing and anchored to the rotary drive shaft. This enables the shutter to be opened or closed by 4 or 5 complete revolutions of the rotary drive while being sufficiently insensitive to the precise position of the rotary drive so as still to allow any of the six samples to be studied. Filament outgassing procedures etc. were carried out with the shutter closed and this greatly extended the life of the photocathode.

2.3 Electronics

The collected photocurrent is fed direct to the input of an integrated circuit (National Semiconductors LH0042CD). This device has FET input and very low input noise current (negligible cf. shot noise in the collector current). A feedback resistor of 100 MΩ was used; a large value is required to minimise the effect of Johnson noise to give the shot noise limited condition under normal operation[14]. The integrated circuit is operated at the collector potential and shielded by an aluminium box also at this potential to reduce microphonic interference. A further earthed aluminium box encloses this and is attached direct on to the vacuum flange where the signal-carrying electrical feedthrough is mounted.

The output from the integrated circuit is taken to the input of the lock-in amplifier which is the Brookdeal 401A. This device has an internal oscillator, the 1.17 KHz output being used for the modulation frequency. This is connected to the primary of the isolating transformer via a potentiometer which sets the modulation level. The transformer secondary is connected in series with the

EHT ramp voltage and beam current monitoring meter.

The analogue output from the lock-in amplifier is taken to an analogue-to-pulse converter (Dynamic Measurements Corp. 801-A). This device gives a train of output pulses with frequency proportional to the analogue input; and this procedure enables the existing PDP8-based data system for the photoelectron spectrometer to be used without modification since it accepts a pulse input. The Multi-Channel Scaler programme ('MCS' due to P.J. Page) allows accumulation of data by repeatedly scanning over the selected voltage range and gives an altogether more flexible means of obtaining and displaying data. There are 1024 data channels with the facility available to vary continuously the number of data channels scanned over as well as the voltage range. The dwell time per channel per scan is approximately 40 ms.; thus for a typical 'half-memory' (512 channels) scan the time taken is $\sim$ 20 seconds. Data can be displayed at the end of any scan on an oscilloscope and a tape cassette system enables data to be stored or retrieved in seconds.

2.4 Vacuum System

The original vacuum apparatus was the Vacuum Generators CHV12 which gave an operating pressure of 10^{-8} Torr. Many of the earlier results which were obtained with this system have been recently repeated under much better vacuum conditions. These were achieved by replacing the viton sealed pyrex jar with a gold wire sealed stainless steel chamber. After a relatively mild bake to $\sim$ 150°C. the ion/sublimation pumped system attains a pressure $< 2 \times 10^{-10}$ Torr, this being the X-ray limit of the ion gauge (V1G10).

2.5 Cleaving Arrangements

Various methods for cleaving crystals in vacuo were tried; the main difficulty comes from having to hold the crystal firmly to a holder while in electrical contact, but without in any way infringing on the front surface. The method eventually adopted was found to be very reliable and is illustrated in figure 2d.

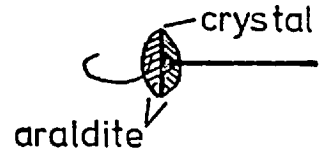

2d

Electrical contact is made between the crystal and tungsten rod by means of a tiny blob of Wood's metal (melting point < 100°C.). A sound mechanical contact was then ensured by adding a small quantity of araldite which, on heating in an oven (∿ 70°C.) for about half an hour, becomes initially liquid flowing to the edges and then hardens to form an ideal holder. The 'araldite sandwich' is then completed, embedding a wire in the front surface layer which can be used to pull the crystal apart. The surface for study was prepared by cleaving in vacuo immediately before running, either by hooking the above-described wire with a linear motion drive or, when this was not available, a 'trip-wire' arrangement to pull off the top araldite layer together with part of the crystal.

The in-vacuum cleaving approach to surface preparation has proved to give very satisfactory results yielding a clean and, for the t.m.d.'s optically flat surface. Thus the SXAPS for pyrolitic graphite given in a later chapter shows considerably better resolution than previously published data[16,17] where different surface preparation procedures were adopted.

2.6 Experimental Procedure

After bakeout and outgassing of various filaments (including

the main operating filament which when 'new' was outgassed overnight and on subsequent occasions by operating for several hours at a filament current larger than that used in operation) a pressure $\lesssim 2 \times 10^{-10}$ Torr was achieved. When operating, sample heating was probably responsible for the slight rise in pressure though usually still within the 10^{-10} Torr range, or occasionally in the low 10^{-9} Torr range. The sample temperature during operation has been measured to be 80°C. for a typical situation. Transition metal dichalcogenides are quite stable at such temperatures and the heating effect may, if anything, be advantageous by helping to keep the surface clean for a longer period of time. In the more recent UHV experiments on TiS_2 and $TiSe_2$ for example even the fine detail remained unchanged with time over a period $\sim$ 30-60 minutes. For the most significant spectra obtained in these studies precise reproduceability has been obtained for separate UHV cleaves.

As described above data is accumulated in 20 second scans and can be stored on cassette tape. This set-up allows an essentially constant monitoring of the spectrum since the accumulated data can be periodically stored on tape and the process restarted. This, in fact was the procedure adopted and, provided no deterioration was in evidence, the sets of data could subsequently be added together. Except for cases of very weak signals the essential outline was clear within only 2 or 3 scans lacking only the statistical conviction that greater lengths of time allow.

2.7 Pulsing the Filament

As noted above, a factor which is expected to influence resolution is the voltage drop along the emitting region of the filament. One possible method of eliminating this effect is to heat the filament by pulses and accept data only while the voltage drop

along the filament is zero. Such an arrangement was tried (though not adopted), a small modification to the filament emission regulator enabling the filament current to be switched on and off by the computer, which was then programmed to accept counts only while the filament was off. It was, however, found necessary to have a relatively large proportion of the time with the filament current on; and this combined with the fact that emission falls off rapidly as the filament cools meant that there was a considerable sacrifice of signal (by a factor $\sim$ 20 or more). Nevertheless, very noisy spectra were obtained from graphite, but any improvement in resolution was too small to be observed in the noisy conditions. A filament of larger thermal capacity would probably be more useful for this mode of operation, but would have involved some rebuilding of the emission regulator to cope with a much larger filament current. This was not attempted since the spectra obtained suggested that there was little improvement to be had in this direction and that the voltage drop along the filament was not a serious broadening effect for the particular filament used in these experiments.

2.8 Work Function Correction

In order to obtain the incident electron energy (in eV) w.r.t. the sample Fermi level it is necessary to add to the potential difference between sample and filament (in volts) the work function of the tungsten filament (taken to be 4.5 eV). This arises because an electron has to have at least this energy w.r.t. the filament Fermi level in order to be thermionically emitted. Figure 2e illustrates this.

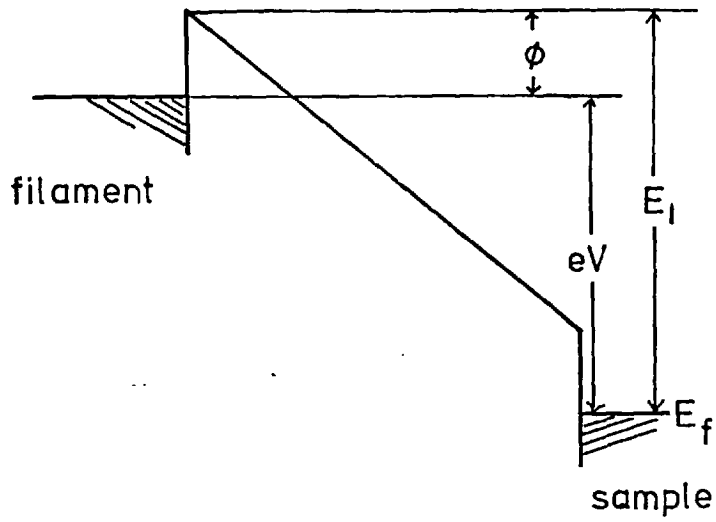

2e Work function correction

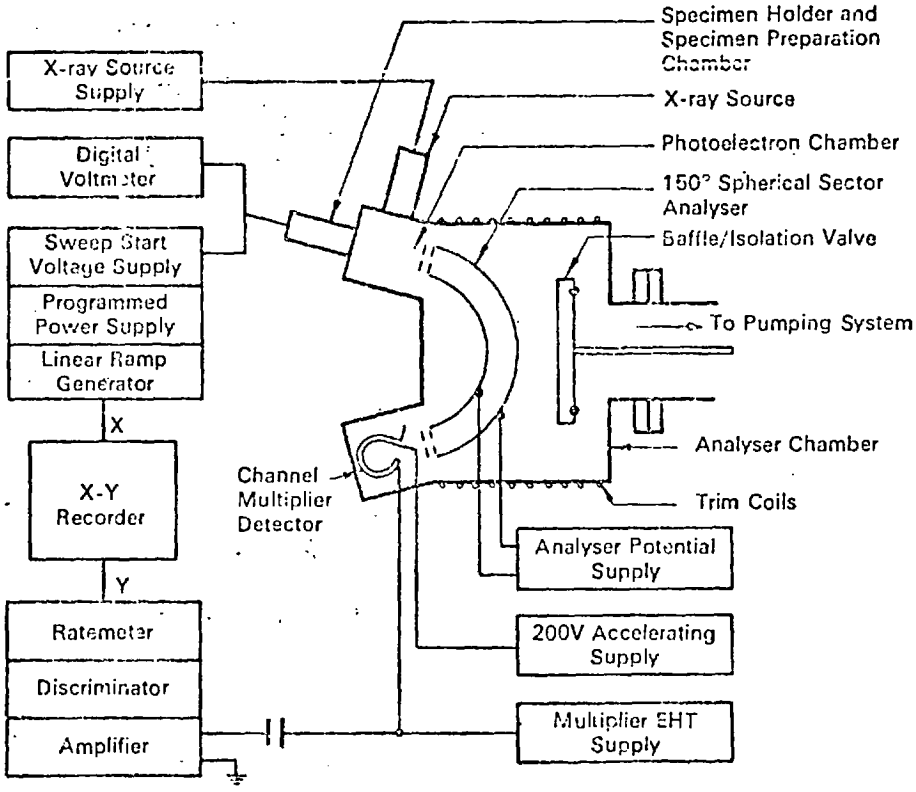

2f ESCA schematic

2.9 ESCA Measurements

The technique of X-ray Photoelectron Spectroscopy (XPS) was also utilised during the present studies. The apparatus used for these experiments (Vacuum Generators Ltd. ESCA 3) is shown schematically in figure 2f. In this technique the surface is irradiated by monochromatic X-radiation and the energy distribution of the photo-emitted electrons determined. Core electrons of binding energy E_B are emitted with energy given essentially by $(hw - E_B)$ while the ejected electrons with highest kinetic energy are expected to reflect the one-electron density of valence band states[18].

CHAPTER 3

THEORETICAL CONSIDERATIONS OF SXAP PROCESSES

3.1 The Self-convolution Model

In Soft X-ray Appearance Potential Spectroscopy the total soft X-ray intensity emitted from a surface is measured when the surface is bombarded with electrons. As the energy of the incident electrons is continuously varied there occur sharp increases in the X-ray yield at energies corresponding to the binding energies of core electrons. At the threshold for the excitation of core electrons, both the incident and excited core electrons are scattered to states immediately above the Fermi level. The allowed combinations of final states for the two electrons are limited to those which fulfill the requirements of energy conservation; and, on assuming slowly varying matrix elements for the transitions and sharp initial states, the excitation probability is found to be proportional to a self-convolution of the conduction band density of states.

$$\text{i.e. } P(E) \alpha \int N(E') N(E-E') dE'$$

{N(E') = density of states at E' and E is the excess energy of the incident electron over and above the binding energy of the core electron}.

This relationship forms the basis for the interpretation of spectra in later chapters where strict adherence is assumed for the purpose of arriving at a form of N(E'). The accuracy of this procedure clearly depends upon the validity of the approximations made in arriving

at the self-convolution integral. As will be seen in many cases the spectra obtained are certainly qualitatively in agreement with the predictions of the self-convolution model. Nevertheless its quantitative application must contain errors and it is instructive to consider the processes involved in the SXAP experiment so that the limitations of this interpretation are brought out.

In the absence of any truly satisfactory analysis in the literature a number of sources have been called upon in what follows, but a comprehensive treatment is clearly beyond the scope of the present work. The intention is rather to derive the self-convolution equation and consider briefly some of the assumptions it is necessary to make, but without entering into a detailed consideration of them.

3.1.1 Emission Products

We follow Park and Houston[19] initially in formulating a description of emission products from an electron bombarded surface. It is assumed that we are dealing with incident electrons of energy (E_1) close to the binding energy (E_B) of a particular singlet core state. Any core level of lower binding energy is neglected which in practice means that it must be sufficiently far removed energetically to provide only a structureless background in the APS at the energy considered.

The incoming electrons can be supposed to divide between two channels (figure 3a) i.e. those which lose energy mainly by scattering

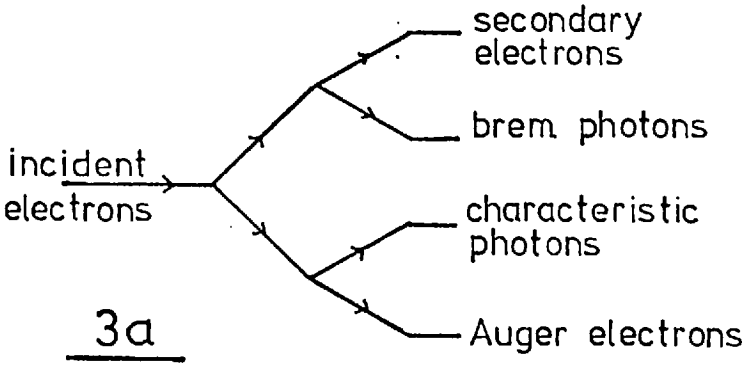

3a

due to valence electrons and those which cause excitation of core electrons. The two channels are assumed to be mutually exclusive which may oversimplify, but this is adequate for present purposes. The former case, where electrons lose energy by scattering from valence electrons, lead to the occupation of excited states over a range of energies. For those which have energy above the vacuum level the possibility exists that they will be emitted, possibly after further scattering events, as 'secondary electrons'. Classically whenever a charged particle accelerates it emits radiation. Quantum mechanically there is actually only a small probability that a photon will be emitted when an electron collides with another particle, but both calculations give similar results for the intensity of radiation emitted. Such radiation which has a continuous energy distribution is called bremsstrahlung.

For electrons which take the core excitation channel the resulting emission consists of the de-excitation products of the core holes having energies related to the particular core state. These are the Auger electrons and characteristic photons.

3.1.2 Soft X-ray Yield

Suppose now the probability that an electron, energy E_1, entering the solid will cause excitation of a core electron is $P(E_1)$ ($P(E_1) = 0$ for $E_1 < E_B$). The intensity of the bremsstrahlung radiation (BR) must then be proportional to $\{1 - P(E_1)\}$, this being the fraction of the incident electrons taking the upper channel. The fraction (α_B) of the incident energy flux which is emitted as BR has been determined[20] to be

$$\alpha_B = kZE_1$$

where k is a constant $\simeq 7 \times 10^{-10}$ eV^{-1}, and Z is the atomic number. Thus the intensity ($I_B = \alpha_B N E_1$ where N is the number of electrons incident in unit time) varies as the square of the energy of incident electrons. (An alternative expression[21] includes another term which predicts a linear variation at very low energies but the precise form is unimportant here). Since the effective number of electrons producting BR is reduced by a factor $P(E_1)$ we write:

$$\alpha_B' = k Z E_1 \{1 - P(E_1)\}$$

The fraction of the incident energy flux (α_C) which is emitted in the form of characteristic photons can be given in terms of the total fluorescence yield ω defined by

$$\omega = \sum_i \omega_i$$

where ω_i is the probability that the core hole will relax with the emission of a photon energy E_i. The mean photon energy can also be defined as:

$$E_\nu = \frac{1}{\omega} \sum_i E_i \omega_i$$

Hence we see that

$$\alpha_C = P(E_1) \times \omega \times \frac{E_\nu}{E_1}$$

The total fraction (α) of the incident energy flux which emerges as photons is given by:

$$\alpha = \alpha_B' + \alpha_C$$

$$= kZE_1 \{1 - P(E_1)\} + \omega \frac{E_\nu}{E_1} P(E_1)$$

$$= kZE_1 + P(E_1) \{\omega \frac{E_\nu}{E_1} - kZE_1\}$$

Below threshold $P(E_1) = 0$ and α is determined only by the BR. Above threshold, however, characteristic photons are emitted increasing α, but the intensity of BR actually decreases as the core excitation channel opens. The net effect on α is determined by the sign of $\{....\}$ which experimentally is observed to be positive. The assumption here that the BR behaves at threshold the same as when far removed is not always true (see section 3.3.4).

3.1.3 Relation to the Observed Spectrum

The intensity (energy/unit time) of the radiation emitted should then be given by:

$$I = k Z N E_1^2 + N P(E_1) \{\omega E_\nu - kZE_1^2\}$$

Then superimposed on the background due to BR which varies as E_1^2 there is a small jump proportional to $\{....\}$. An order of magnitude calculation for a typical 3d transition element taking $\omega \sim 10^{-3}$ shows that the first term is some two orders of magnitude greater than the second which we neglect. On taking the derivative as in APS we expect to see a linearly increasing background. In fact for strong thresholds the background can be assumed flat and so the APS threshold shape, $A(E_1)$, can be approximated to

$$A(E_1) = K \frac{dP(E_1)}{dE_1}$$

where K includes a constant depending on the photo-yield of the photo-cathode. Although the latter quantity may vary with photon energy it will not modify the threshold shape since this is signalled by characteristic photons. It could, however, cause deviations from the

linear background depending upon the energy distribution of the BR and the yield of the photocathode as a function of photon energy. But as noted above the background is found experimentally to be essentially flat though Tracy[7] observed a weak Ti 'threshold' in APS when using a Ti photocathode. This occurs as the bremsstrahlung cut-off sweeps across the threshold for excitation of Ti $L_{3,2}$ levels and is the basis for the photon appearance potential (PAPS) experiment described later. No such effect is observed, however, for a KCl photocathode.

3.1.4 Excitation Rate

Having shown within the limits of the above model that the SXAP threshold should be proportional to the derivative of the excitation probability we now require to calculate this. We use the result from time dependent perturbation theory for the transition probability per unit time[22] for the incident electron in state $\psi_1(\underline{r}_1)$ and core electron in state $\psi_2(\underline{r}_2)$ to final states $\psi_3(\underline{r}_1)$ and $\psi_4(\underline{r}_2)$

$$\text{i.e.} \quad W(E_1) = \frac{2\pi}{h} |M|^2 \, \delta(E_1 + E_2 - E_3 - E_4) \qquad \ldots.(1)$$

where E_1, E_2, E_3, E_4 are the respective energies of the electrons in their initial and final states and the delta function ensures conservation of energy. M is the matrix element for the transition given by

$$M = \int \langle \psi_1(\underline{r}_1) \; \psi_2(\underline{r}_2) \; | \; V \; | \; \psi_3(\underline{r}_1) \; \psi_4(\underline{r}_2) \rangle \; d\underline{r}_1 \; d\underline{r}_2 \qquad \ldots.(2)$$

V is the interaction potential between them namely the screened Coulomb potential given by

$$V = \frac{e^2}{4\pi\varepsilon\varepsilon_o |\underline{r}_1 - \underline{r}_2|} \qquad \ldots.(3)$$

and ε is the complex dielectic function. (A more complex expression[23] for $|M|^2$ is arrived at upon including the exchange interaction but this is omitted here since we are to assume an average value for $|M|^2$).

By writing the initial and final state wave functions as the product of two one-electron wave functions we are implicitly assuming that no other electron is affected by the transition. 'Many electron effects' can give rise to such phenomena as threshold singularities and plasmon loss satellites. These will be considered later.

To obtain the total transition probability per unit time we must weight (1) by the probability of the core electron have the specified energy and sum over all such possible states as well as over all possible final states. In addition we note that momentum must be conserved which gives the requirement we sum only over such combinations as satisfy:

$$\underline{k}_1 + \underline{k}_2 = \underline{g} + \underline{k}_3 + \underline{k}_4 \qquad \ldots.(4)$$

where $\underline{g}$ is any reciprocal lattice vector. But since the core electron is spatially localised $\underline{k}_2$ is not well defined for the core state. Thus (4) would not be expected to impose any strong limitation, and to simplify the calculation it is ignored - 'the random - $\underline{k}$ approximation'. This step was apparently first taken by Berglund and Spicer[18] and with some success by Kane[23]. We assume that the probability of finding the core electron with energy $E_2 \rightarrow E_2 + dE_2$ is given by

$$P_i = N_i (E_2)\, dE_2$$

and the probability of either final state having energy $E_{3,4} \rightarrow E_{3,4} + dE_{3,4}$ is

$$P_f = N (E_{3,4})\, dE_{3,4}$$

Here N_i and N are the density of states functions per unit energy

per atom. To avoid having to include the Fermi function, N is defined as the density of unfilled states and we assume N = 0 for $E_{3,4} < E_f$.

So, with the summations over initial and final states replaced by integrations, we have for the total transition probability per unit time

$$W_T(E_1) = \frac{2\pi}{h} |M_{av}|^2 \int N_i(E_2)\, N(E_3)\, N(E_4) \times \delta(E_1+E_2-E_3-E_4)\, dE_2 dE_3 dE_4 \quad \ldots.(5)$$

It is assumed that M is sufficiently slowly varying to enable it to be taken outside the integration using some average value $|M_{av}|^2$.

Finally it is assumed that the core level is sharp enough to take $N_i(E_2) \simeq \delta(E_C - E_2)$. The delta function in (6) obviates the need to keep both final state energies explicitly stated and we denote the other as E', writing also $E \equiv E_1 + E_C$. The integrals reduce to

$$\int_o^E N(E')\, N(E-E')\, dE'$$

$W_T(E_1)$ is simply proportional to $P(E_1)$ via some mean lifetime of the hot electron $\tau(E_1)$ and the SXAP threshold is evidently given by:

$$A(E) \alpha \frac{d}{dE} \int_0^E N(E')\, N(E-E')\, dE' \quad \ldots.(6)$$

which is the required result. The Fermi energy is taken to be zero and the limits were inserted by recalling that N(E') = 0 for E' < 0.

Equation (6) then shows that to the extent that our assumptions are justified the SXAP threshold shape should be given by the derivative of the self-convolution of the conduction band density of states. We have, in particular, assumed we are dealing with sharp core level states and essentially constant matrix elements. It should be noted, however, that because of the spatial localisation

of the core state it will overlap only part of the conduction band states so that we shall 'see' a 'localised' density of states. This is a somewhat intangible quantity and we shall assume in general the N(E') can be regarded as the 'total' density of states when comparing APS with other data.

3.2 Surface Sensitivity

So far the interaction between an incoming electron, energy E_1, with an isolated core state, energy E_C, has been considered. Clearly the energy distribution of the incoming electron beam may also influence the threshold shape, and this will be a function of depth into the solid. The energy spread in the initial beam is generally small (see section 2.2) cf. the width of SXAP thresholds. In the solid the electrons are subject to various inelastic scattering mechanisms. The dominant processes are electron-electron scattering and electron-plasmon scattering. The effect of the latter is simply to give an image of the elastic peak at energy lower by the plasmon energy. Electron-electron scattering is probably the more important[24] and its effects are not so obvious and so is considered more fully.

3.2.1 Inelastic Scattering of Electrons

Kane[23] following Berglund and Spicer[18] calculated the scattering rate for pair production in silicon using the 'random-k' approach and found agreement with calculations allowing for $\underline{k}$ conservation within the statistical accuracy of the 'Monte-Carlo' method used for evaluating the integrals. Kane's calculations, however, extend only to a few eV above the Fermi level. For much higher energy electrons ($\sim$ keV) energy losses can be correlated with optical measurements. The dielectric response function $\varepsilon(q,\omega)$ can be used

to describe the many electron response of the solid to the incident electron where hq and hω are the momentum and energy of the excitation produced. The function $\varepsilon(0,\omega)$ is obtained from optical measurements so provided the momentum change of the electron is small or zero as for long wavelength plasmons or direct interband transitions this description should hold. Experimentally it works very well for electrons in the keV range but Bauer[25] points out that its inapplicability for slower electrons may be correlated with the fact that the inelastic scattering is less peaked in the forward direction. Bauer derives equations describing the interaction of slow (∿ few hundred eV) electrons with a crystal but draws only 'general conclusions' from them. Essentially he obtains a 'generalised' (i.e. dropping the condition $\Delta\underline{k} = 0$) joint density of states function. This is essentially also the result of Berglund and Spicer[18] using the random-k approach. They obtained for the probability per second, P(E',E) dE, that an electron, energy E', is scattered to energy E to E + dE is given by

$$P(E',E) = \int \frac{2\pi}{h} |M_s|^2 N_u(E) N_f(E_o) N_u(E_o + E' - E) \, dE_o$$

omitting their Fermi functions and using N_f and N_u for filled and unfilled density of states functions. If it is assumed that the energy loss is small so that $E >> 0$ as is E' then N(E) can be taken as constant and the above reduces to a fold of the filled with unfilled states.

This suggests that scattering due to valence electrons in general involves an energy loss of several eV on average so that such processes will tend to 'damp' rather than 'broaden' the elastic peak as a function of depth into the solid. The implication is that APS is sensitive only to the surface region determined by the penetration depth of the electrons but the threshold shape is not seriously affected by inelastic scattering.

3.2.2 Analogy between SXAPS and XPS

XPS can in some respects be regarded as the inverse of SXAPS. Whereas the surface sensitivity of SXAPS is determined by the 'penetration' depth of the elastic beam, in XPS it is the 'escape' depth which is of importance. Accordingly we should expect the same degree of surface sensitivity in both techniques in so far as the kinetic energies of the electrons are similar, which is generally true. It is, of course being assumed that the inelastic mean free path of the electrons is sufficiently small that no appreciable X-ray absorption occurs within this depth. Langer[26] has collected experimental data on the escape depth from various sources and plotted this as a function of electron energy. This diagram is reproduced in figure 3b, and shows a broad minimum of $\sim$ 10 Å close to the sort of energy we are concerned with. Thus SXAPS and XPS are sensitive only to the topmost few atomic layers where it is possible that differences occur from the bulk electronic structure. Nevertheless bulk interpretations, particularly for layer materials[27], generally seem to be applicable even for UPS (ultra-violet photoelectron spectroscopy) which is even more surface sensitive.

By means of an argument due to Turtle and Liefeld[28] the analogy between XPS and SXAPS can be carried further (they were actually concerned with X-ray isochromats but it applies equally well for SXAPS). Assuming negligible X-ray absorption we define a function $f\{x, (E_1-E)\}$ such that the probability that an electron incident at the surface in SXAPS with energy E_1 reaches depth $x \rightarrow x + dx$ with energy $E \rightarrow E + dE$ is given by $f\{x, (E_1-E)\}\, dx\, dE$ (see figure 3c).

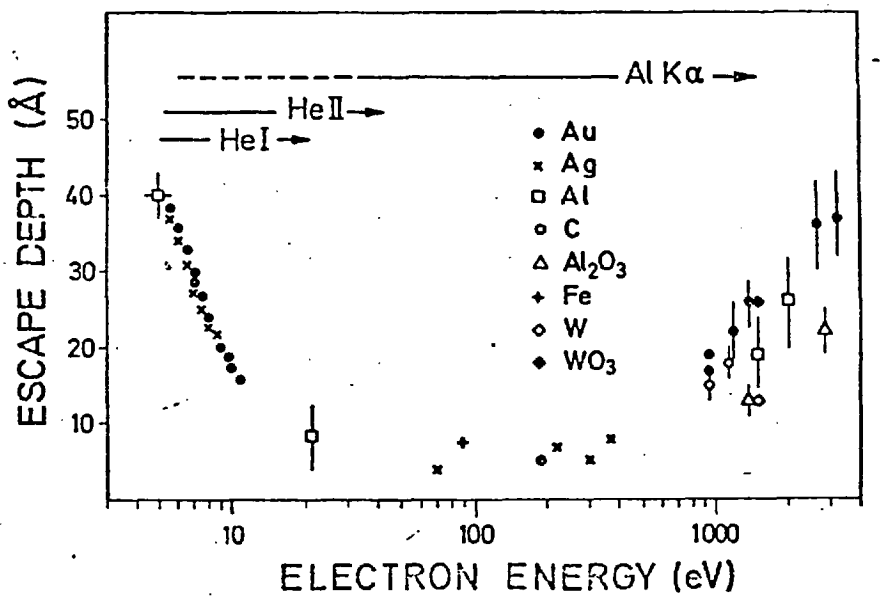

Energy dependence of
electron escape (penetration) depth

3b (Langer)

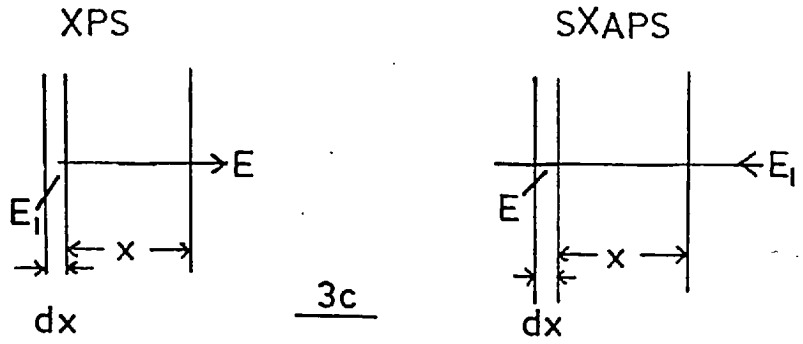

3c

We suppose that the same function describes the probability that an electron excited to energy E_1 at depth $x \to x + dx$ in XPS escapes from the solid with energy $E \to E + dE$. Actually, of course, this is an approximation since we have reduced the problem to one dimension by means of some sort of average over the initial angle of the electron trajectory with the surface normal. Although this average will not be the same in both cases since there is probably a smaller range of angles in SXAPS, it should at least be good for a first approximation.

Suppose then that the core hole excitation rate in SXAPS is $W_T(E)$ giving for the total excitation rate as observed

$$A_o(E_1) \alpha \int_{E=0}^{E_1} \int_{x=0}^{\infty} W_T(E)\ f\{x,\ (E_1-E)\}\ dx\ dE \qquad \ldots.(1)$$

For a sharp core level the observed energy distribution in XPS would then be given by

$$X(E) \alpha \int_{x=0}^{\infty} f\{x,\ (E_1-E)\}\ dx \qquad \ldots.(2)$$

In principle, we could allow for the effects of inelastic scattering in SXAPS by unfolding the XPS core function from the SXAPS threshold function. Such a deconvolution is of rather dubious value, however, since core peaks in XPS are generally not much broader than the X-ray line width. In many cases also XPS peaks show no appreciable asymmetry indicating that inelastic scattering is not a serious consideration. That asymmetries do occur in other instances has

been correlated[29] with a high local density of states and is thus dependent upon mechanisms intrinsic to the excitation[30]. This evidence would tend to invalidate Turtle and Liefeld's deconvolution, but also serve to indicate more usefully that it is unnecessary in accord with the conclusions of 3.2.1.

3.3 Limitations of the One-Electron Model - Many Body Effects

In 3.1 several assumptions necessary to avoid involvement with many electron processes were noted. In particular it was assumed that the de-excitation process was independent of the mode of excitation. One-electron wavefunctions made the calculations tenable and any influence that the core hole potential may have on the final states was neglected.

Although there has been considerable interest in the role of many body effects in X-ray spectroscopy there has been no detailed consideration of their influence on SXAPS and we rely largely on the less formal discussions of the X-ray spectroscopy case by March[31] and Hedin[32] and attempt to pick out some points of relevance to the SXAPS case.

3.3.1 Core Hole Potential

Stott and March[33] drew attention to the work of Catterall and Trotter[34], where the satellite emission was studied and found to have essentially the same shape as the principal X-ray emission. Stott and March observed that if, as had previously been suggested[35], the core hole potential strongly influences the shape of the emission spectrum then it would be expected that two core holes would have a greater effect and appreciably modify the satellite emission cf. the main line.

3.3.2 Threshold Singularities

A particular feature of some X-ray emission and absorption spectra not readily explicable by one electron models is an unexpected peak at the edge. (For a summary of such observations see Park, Houston and Laramore[36]). It appears that Mahan[37] first gave a description of this. He found that 'threshold singularities' could arise due to the interactions between the suddenly created (absorption) or annihalated (emission) core hole with the conduction electrons. Nozieres and de Dominicis[38] solved a simplified model by means of a 'time dependent one body' approach considering the conduction electrons to be scattered in the potential of the core hole. Laramore[10], following Nozieres and de Dominicis, showed that threshold singluarities were to be expected in SXAPS. He found, because there are no strong selection rules in SXAPS, that it is possible for stronger divergences to occur than for the X-ray case, for transitions involving s-state core levels.

3.3.3 Incomplete Relaxation

For sufficiently energetic incident particles the initial state can be multiply ionised and this gives rise to the the X-ray satellite emission. Multiple ionisation can occur either through Auger emission or 'shake-up'[32] and Hedin[32] observes that the same processes can give rise to low energy electron hole pairs. In this case the Auger process would have to involve closely spaced core levels such as the L_2 and L_3 such processes usually being referred to as Coster-Kroning transitions. In cases where the core hole lifetime is sufficiently short that the electron hole pairs do not have time to decay, then we should see a high energy tail in the X-ray emission. Hedin further points out that the effect, observed for light metals as long ago as 1940 by Skinner[39], may be more pronounced for transition

elements with their shorter core lifetimes. The importance of such effects in SXAPS can only really be assessed from near threshold X-ray emission spectra, very few of which seem to exist. However, Hanzeley and Liefeld[40] reported high energy structure for iron which changed as a function of the incident electron energy, and this is shown in figure 3d (Corrections were made, however to the actual data).

3d

(Hanzeley & Liefeld)

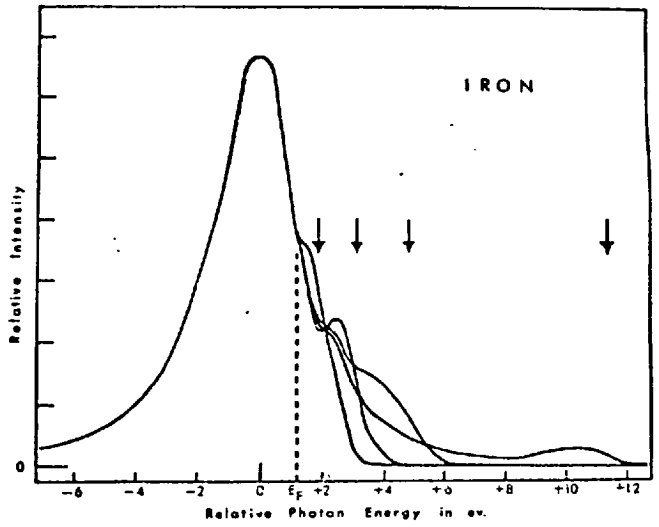

Shape of the threshold level iron L_{III} line as a function of the incident electron energies indicated by the arrows.

Hanzeley and Liefeld actually give a different explanation (see following section). However the changing spectral shape as a function of incident energy E_1 indicates some coupling between excitation and de-excitation processes. In 3.1 it was assumed that the X-ray intensity $I(E_1)$ is proportional to the excitation probability $P_x(E_1)$ which requires that the de-excitation probability $P_D(E_1)$ is a more slowly varying function of E_1. That the independent emission dominates suggests that this is a reasonable approximation in the case of iron.

3.3.4 Bremsstrahlung Resonance

An evident breakdown of this condition, however, occurs in the SXAPS of rare earth elements (see section 4.7). X-ray emission spectra for near-threshold excitation of lanthanum[41] and cerium[42]

have been obtained by Liefeld, Burr and Chamberlain (LBC). For lanthanum they observe a moving peak in the X-ray spectrum whose energy is consistently 5.5 eV less that the incident electron energy and which resonates as the electron energy sweeps through the threshold for the excitation of the M_5 and M_4 levels. A series of these spectra is reproduced in figure 3e. The characteristic Mα line is seen increasing in intensity at the threshold but overshadowed by the resonance of the variable energy peak which actually appears to become significant at sub-threshold energies.

These phenomena are explained[41] with reference to the continuum limit and continuum isochromat spectra of lanthanum both of which are expected to reflect the density of states above the Fermi level. These show a sharp peak some 5.5 eV above the Fermi level due to the unfilled 4f states in lanthanum. This peak co-incides with the one observed in the X-ray spectra and would indeed be expected to track the electron energy but its resonance at threshold was not expected. LBC suggest an explanation of this in terms of a resonance of the cross-section for scattering incident electrons to the unoccupied 4f levels, and further propose that the mechanism by which the resonance occurs involves the formation of an intermediate bound ejected electron (BEE) state. This subsequently decays radiatively with the filling of the core vacancy and the other electron scattered to a 4f state.

This phenomenon is effectively a resonance of the bremsstrahlung background and the failing of the model in 3.1 may alternatively be considered that it assumes the BR to obey the same simple power law at threshold as at other energies. The much weaker structure seen for iron in figure 3d was explained[40] in a similar way but the model of 3.1 should still be applicable for transition elements.

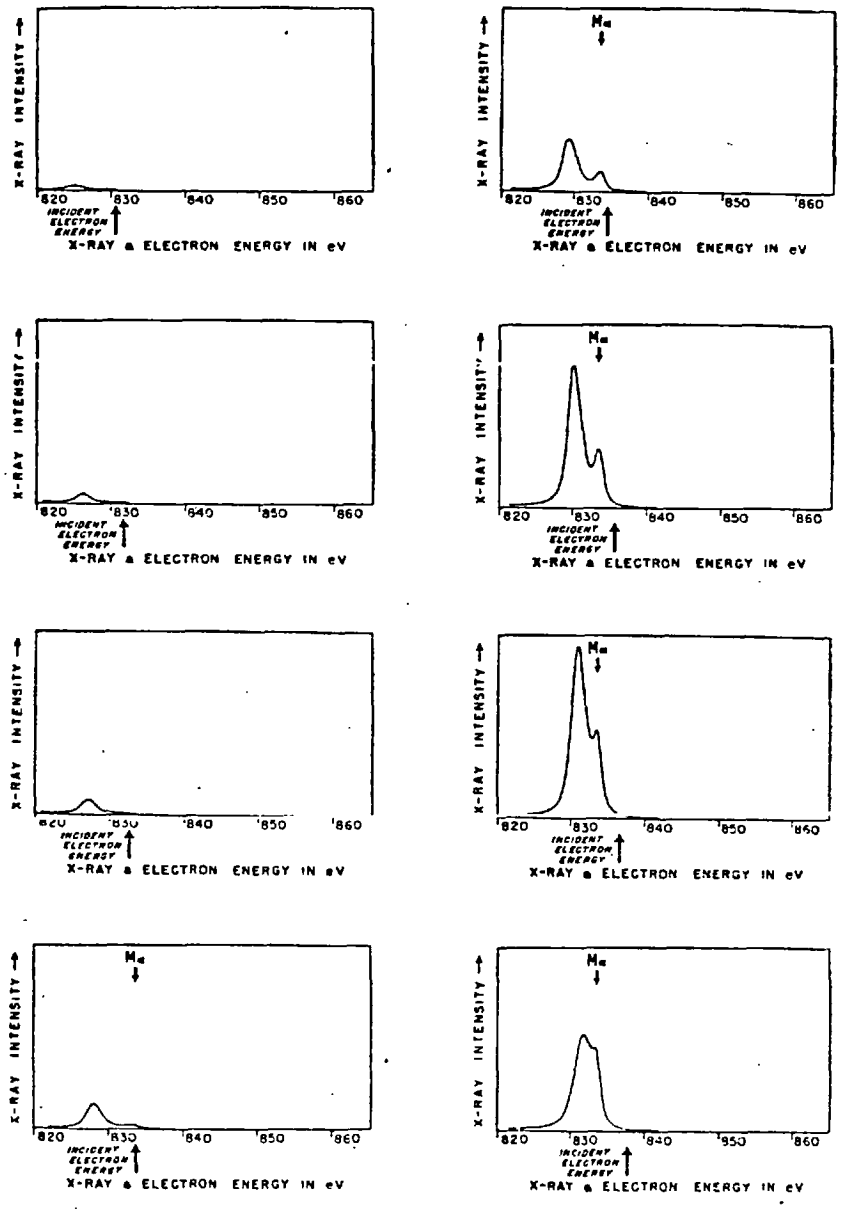

La X-ray emission

3e (Liefeld et al)

3.3.5 Plasmon Emission

If the valence electrons of a solid are regarded as free then it is found[43] for the long wavelength limit that self sustaining oscillations of the electron gas can occur at a frequency given by

$$\omega_p = \left(\frac{ne^2}{m\varepsilon_o} \right)^{\frac{1}{2}}$$

where n is the electron density. The energy associated with such 'collective' oscillations is quantised in units $h\omega_p$, which typically may be $\sim$ 10-20 eV, called the plasmon energy.

3.3.5.1 Role in Core Level Spectroscopies

In SXAPS the incident electron may lose energy $nh\omega_p$ by exciting an integral number of plasmons prior to exciting a core electron with probability $P_n P_x(E_1 - nh\omega_p)$ where P_n is the probability that the incident electron excites n plasmons essentially before any other inelastic scattering event. Thus $P_n = P_1^n$.
In addition to the main threshold structure we should see 'satellites' displaced by amounts $nh\omega_p$ with intensities decreasing by a factor P_1 for each successive one. Clearly the threshold shape is not modified at energies which exceed the binding energy by an amount less that $h\omega_p$ and plasmon emission is not normally an important process in SXAPS since only weak satellites are observed (Reference 44 and section 6.6.1). The process described above can be referred to as 'extrinsic' plasmon emission where the incident electron loses energy $h\omega_p$ before continuing its passage through the crystal with the possibility of subsequent core level excitation. By the argument of 3.2 extrinsic processes should affect SXAPS to the same extent as XPS where again the first plasmon satellite is generally rather weak.

Plasmon emission can alternatively occur due to the 'shock'

on the valence electrons when a core hole is suddenly created. Such processes are referred to as intrinsic and intensities are expected[44] to follow a Poisson distribution ($P_1^n/n!$). In X-ray spectroscopies calculations first predicted much stronger satellites than were observed experimentally; but much better agreement was found when it was pointed out that it is not the core hole potential alone that acts but the change in potential occurring during the electronic transition. Langreth[9] generalised this with the statement that where the number of 'slow' electrons is not conserved during the transition coupling to plasmons should be larger than where there is conservation. Here 'slow' electrons are conduction electrons or core electrons. It is readily seen that for both SXAPS and XPS slow electrons are not conserved, and similar plasmon satellite intensities are expected for intrinsic processes also. A much-quoted apparent contradiction of this occurs for graphite where it has been suggested[16,17] that strong plasmon coupling occurs in SXAPS (but not XPS). Bradshaw et al.[45] proposed a model to explain this, but as we shall see in chapter 7, the details of the graphite SXAP spectrum are in better agreement with a simple conduction band self-convolution model.

3.3.5.2 Relation to Band Structure

Plasmon energies can be predicted from a knowledge of the band structure via the frequency dependent dielectric function $\varepsilon(\omega)$. For $\varepsilon(\omega) \rightarrow 0$ we can have finite polarization $\underline{P}$ for zero applied field $\underline{E}$ which is the condition that self-sustaining oscillations can occur. A useful result is found[46] when the valence band is made up of two separated groups of bands. Two plasma resonances can be found corresponding to oscillations involving (a) those electrons in the upper group only i.e. the most loosely bound and (b) all the

valence electrons. Suppose the number of electrons in the upper and lower groups to be n_u and n_l per atom respectively. The free electron plasma frequencies are

$$\omega_{P1} = \left(\frac{n_u Ne^2}{m\varepsilon_o} \right)^{\frac{1}{2}}$$

$$\omega_{P2} = \left(\frac{(n_u + n_l) Ne^2}{m \varepsilon_o} \right)^{\frac{1}{2}}$$

where N is the atomic density. Such a splitting of bands occurs for example in graphite (see section 7.2) where there are three σ electrons per atom which form the covalent bonds and one loosely bound π electron per atom in the p_z orbital. Thus $n_u = 1$ and $n_l = 3$ giving for the π and σ resonances values of 12.5 and 25.1 eV cf. observed values[46] of 7.2 and 26.8. This poor/reasonable agreement for π/σ resonances is typical[46] and is interpreted as mainly due to the screening effect in the π resonance by the σ electrons.

3.4 Summary

In 3.1 the conduction band self-convolution model for the SXAP threshold shape was derived assuming sharp core levels and slowly varying matrix elements. The surface sensitivity of SXAPS was discussed in 3.2 and found to be the same as the in XPS to the extent that the kinetic energies of electrons involved are similar. In the last section a qualitative discussion was given of some of the many-electron processes which may cause deviations from the self-convolution model. At present, however, the best test of the conduction band interpretation remains with experiment and as will be seen in chapters 6 and 7 observations are in excellent agreement with the model of 3.1.

CHAPTER 4

DEVELOPMENT AND APPLICATIONS OF APS

Since the initial activity by Park and Houston, many of whose papers are referred to at various points, a number of other groups have undertaken work on APS. There have been several interesting results within the last year or so and it seems likely that the field will continue to expand. It is the intention here to concentrate on these the more recent developments.

4.1 Variations in the Experimental Set-up

4.1.1 The Detector

A 'low noise' SXAP spectrometer has been described by Andersson, Hammarqvist and Nyberg[47]. They gave an anlysis of noise in SXAPS though a subsequent correction[48] was necessary. They observed that the shot noise limitation in the collector current mentioned previously is itself fundamentally limited by the statistical variations in the actual photon flux. Defining a conversion factor η such that N_γ photons produce a detector flux N_d given by

$$N_d = \eta N_\gamma$$

they demonstrated that this ideal limitation is approached for $\eta \simeq 1$. For $\eta << 1$, however, the S/N ratio is reduced by a factor $(2\eta)^{-\frac{1}{2}}$. (For the KCl photocathode used in the present work it is likely that $\eta \sim 0.1$). In order to achieve the 'ideal' shot noise

limitation Andersson et al.[47] used a liquid nitrogen cooled silicon surface-barrier diode detector where photons produce electron hole pairs. This device also apparently gives some in situ amplification which although, like an electron multiplier, is not necessary, it does enable smaller beam currents to be used while still shot noise limited. For such applications as Andersson et al. had in mind, i.e. chemisorption of gases, this is useful.

4.1.2 X-ray Filters

Although it is characteristic photons that are responsible for the structure seen in APS, photons of other energies are also detected and these only add to the noise. The Characteristic Isochromat Technique involves the use of a grating monochromator to accept only the characteristic photons but because this has a small acceptance angle the S/N ratio is apparently[19] worse than APS. A compromise which works well was suggested by Baun et al.[49]; an aluminium (or beryllium) foil ($\sim$ 6μ) is placed in front of the photocathode. This attenuates the X-ray intensity at all frequencies, but discriminates against the low energy photons of the BR background. The value of this depends upon the energy of the characteristic photons involved; for a samarium sample, with M_5 level $\sim$ 1100 eV, they noted a decrease in the characteristic emission by a factor of 3 while attenuating the total d.c. background by a factor $\sim$ 1000 thus improving the S/N by a factor $\sqrt{1000}/3 \simeq 10$. The advantage is reduced for shallower core levels, however, and may be detrimental. Park and Houston[19] suggest a twin arrangement with the optional use of the X-ray filter. Andersson et al.[47] also used an X-ray filter. For the present studies, with core levels 200 - 450 eV, the improvement is probably marginal[19].

4.2 Related Techniques - AEAPS, PAPS, DAPS

There are several other possible arrangements similar to SXAPS (where the electron excited X-ray yield is detected). The electron excited Auger electron yield can also be measured (AEAPS) as well as the photon induced electron yield (PAPS) though neither of these has been utilised to nearly the same extent as SXAPS. Larger yields are obtained in AEAPS though an electron gun is really necessary; Park and Houston[50] used a simple arrangement but they noted structure due to diffraction effects. PAPS, in fact, can be achieved with the same arrangement as SXAPS but with the 'photocathode' actually consisting of the sample material. A suitable target, usually a transition element, when electron bombarded gives a bremsstrahlung cut-off which serves as a pseudo-monochromatic X-ray source[51]. The PAPS of graphite was, in fact, obtained and is discussed in chapter 7.

The most interesting development is due to Kirschner and Staib[52](KS). They note that the elastically reflected current from an electron bombarded sample exhibits sharp decreases when the energy sweeps through the core level binding energy. This is due to the removal from the reflected beam of those electrons which have excited core electrons. KS have named this appropriately 'Disappearance Potential Spectroscopy' (DAPS). Simple theory suggest that DAPS thresholds would be identical to SXAPS ones since they are determined by the same excitation probability. KS note, however, that DAPS measures the excitation probability more directly without involving fluorescence yields etc. In addition, they point out that DAPS should be more surface sensitive (by a factor $\sim$ 2) since the electron has both to penetrate and escape from the solid after being elastically scattered. Despite these differences, spectra obtained by KS[53] are remarkably similar to SXAPS ones (e.g. for

graphite contamination on a metal surface), and thus provides some justification for the assumption that SXAPS threshold shapes are independent of the de-excitation process. KS[53] have used AEAPS in conjunction with DAPS to study the oxidation of titanium and demonstrate the increased surface sensitivity. They also observe that because of the similar experimental arrangements in DAPS and AES (Auger electron spectroscopy) it is possible to change from one to the other by the 'flick of a switch'. This does not imply, however, that it will necessarily be trivial to convert existing AES set-ups for DAPS because of the requirement to be able to ramp the incoming electron energy, though this should not present any major difficulty.

Unlike SXAPS a dispersive analyser is required for DAPS but this experimental complication is probably offset by the fact that there are many AES set-ups already in existence. DAPS is very much in its infancy but may even be favoured over SXAPS in the future. It does, however, suffer from the same drawback as SXAPS in that it exhibits a lack of sensitivity to some elements. In particular KS mention palladium; they observe that the suggestion of Tracy[7] - that SXAPS's insensitivity to this element is due to a low fluorescence yield - cannot be correct.

4.3 Elemental Analysis

4.3.1 Variations in Sensitivity

The application of SXAPS to surface analysis is hampered, as noted above, by its insensitivity to some elements. Park and Houston (PH) have drawn up an SXAPS periodic table of the elements indicating those for which good SXAP spectra have been observed, and

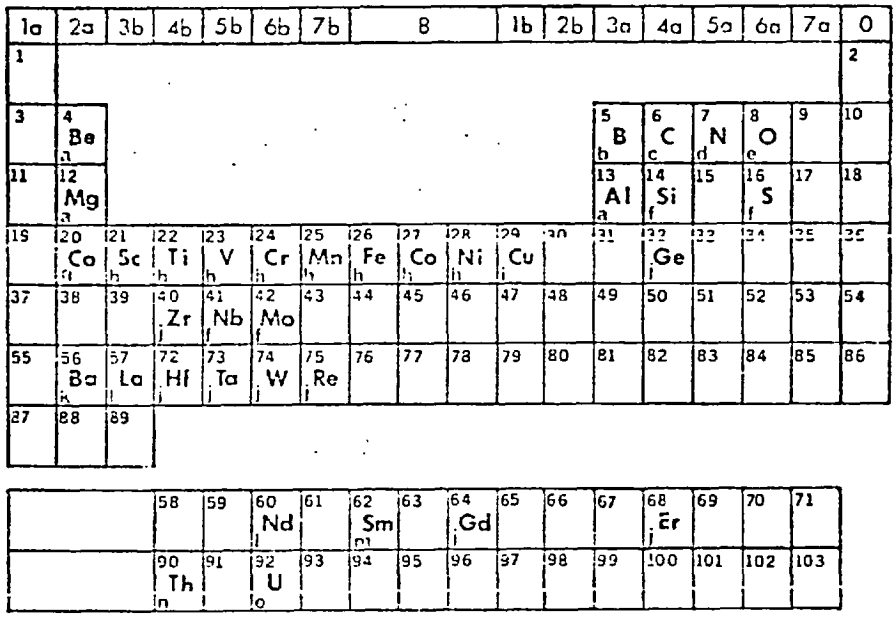

Elements for which good AP spectra have been obtained

4a (Park and Houston)

this is reproduced in figure 4a, an omission from this being lithium[3]. In addition most of the transition and rare earth elements apparently not yet studied could probably be pencilled in.

Among the observable elements, however, there are large variations in sensitivity. The 3d transition elements give peak heights in the first derivative spectrum which are comparable with the background and are readily detected. Rare earth elements have been reported[54] to give much more intense thresholds than the 3d transition series but during the present studies uranium was found to give only comparable sensitivity.

There seems to be a quite general trend of decreasing sensitivity as we descend columns of the periodic table. Thus for transition elements the strength of signal observed goes as 3d > 4d > 5d. As mentioned above Tracy[7] found APS insensitive to palladium which lies immediately below nickel in the periodic table; he deduced that the palladium threshold was less than the 3d elements by a factor > 50. PH confirm[19] that palladium cannot be readily detected with APS (the only other element for which they admit defeat is gold). PH asserted that there is a high density of unfilled 4d states in palladium though the electronic configuration of this element is listed as $4d^{10}5S^{0}$. Although below nickel it may thus be better compared with copper ($3d^{10}4s^{1}$) which gives only weak APS signals[7]; and the insensitivity of APS seems likely to be due to the completely filled d band and a relatively small density of states at the Fermi level.

Typical 4d transition elements give $M_{4,5}$ ($\sim$ 200-300 eV) spectra which are weaker than 3d $L_{2,3}$ by a factor probably something rather less than an order of magnitude. The $L_{2,3}$ levels of the 4d's ($\sim$ 2.5 keV) give spectra which are similar in magnitude to the $M_{4,5}$

ones, an accurate comparison being complicated by the increased background and noise levels. Spectra for molybdenum are shown in figure 4b. The $M_{4,5}$ levels of 5d elements ($\sim$ 2 keV) also probably give the most useful spectra, but the spectrum for tantalum shown in figure 4b took about twenty minutes to obtain. (Better statistics are achieved for 3d elements in a single twenty second scan.)

4.3.2 Excitation X-sections and Fluorescence Yields

The observed sensitivities cannot be simply explained since there are several trends which must be taken into account. In general the sensitivity will depend upon the product $p_x p_d$ where p_x is the threshold excitation probability and p_d is the probability that the de-excitation process involves the emission of a photon i.e. the fluorescence yield (if no Coster-Kronig processes are active).

Data on excitation x-sections near threshold have not been found, but, since we are concerned with the trend between elements rather than absolute magnitudes, those available relating to higher energy electrons may give a reasonable picture. Vrakking and Meyer[55] plot K-shell ionisation x-sections (σ) as a function of binding energy (E_B) for different elements (with a fixed ratio E_1 to E_B) and show that the classical law $\sigma \alpha E_B^{-2}$ is obeyed. Their experimental data give for L-shell x-sections $\sigma \alpha E_B^{-1.56}$.

McGuire has published a series of papers[56,57] listing calculated values for fluorescence yields (ω). For a particular level there is a general increase in ω with atomic number. The overall trend in the product $p_x p_d$ is thus determined by two competing trends in p_x and p_d. The observed general decrease in sensitivity with atomic number for APS suggests that it is the decrease in p_x which predominates.

Sensitivity to 4d and 5d transition elements

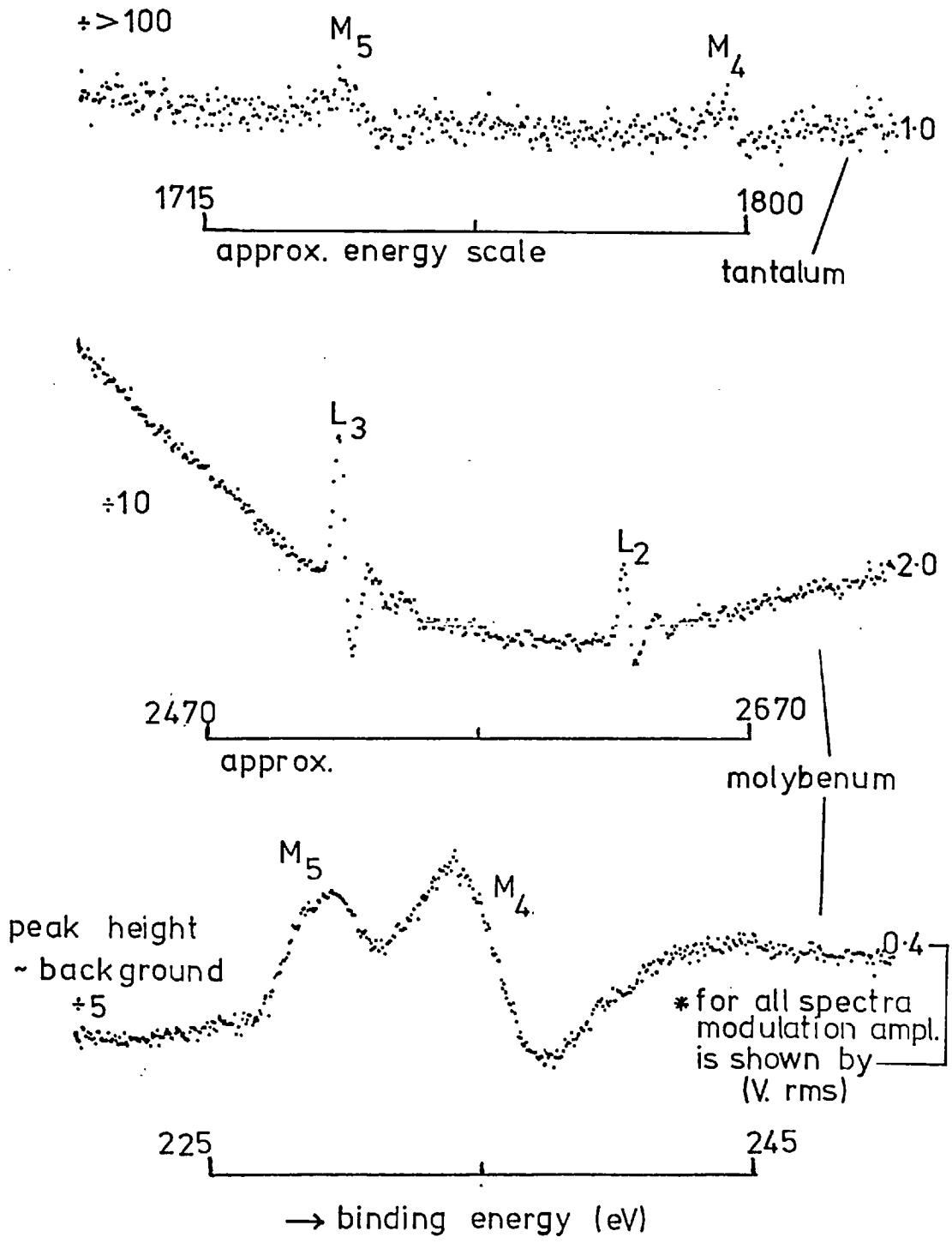

4b

However, because we are concerned with threshold excitation there is a strong dependence on the density of unfilled states at the Fermi level. (To a first approximation $p_x \alpha N^2(E_f)$ since two electrons are scattered to states above the Fermi level.) This N^2 factor strongly modulates the underlying trend and this explains why the observed trend is resticted to columns of the periodic table, as well as the sensitivity to transition elements.

4.3.3 Applications

As is clear from the above discussion APS has considerable disadvantages for routine analysis of surfaces; in general it compares unfavorably with AES[58,59]. Such uses are really restricted to cases where only certain elements are of interest to which APS is sensitive. Where this is true, however, APS has a clear advantage in terms of simplicity since it can be added to a vacuum system with relative ease[6] and has been so used[60]. In addition, as noted by Park[61], APS gives a direct measure of core state energy rather than combinations of three levels as in AES and thus more clearly separates elements which are adjacent in the periodic table, as illustrated in figure 4c for stainless steel. Park et al.[62] have used APS to demonstrate the chromium depletion of vacuum annealed stainless steel surfaces and its consequent lower resistance to corrosion.

4.4 Binding energy determinations

It is often desirable to obtain accurate values of binding energies which may give chemical information. In XPS the observed spectrum may, to a first approximation, be taken to represent the (instrumentally broadened) core level function and the binding energy can be taken to correspond to peak maximum. The use of APS for binding energy determinations is, however, complicated by final state

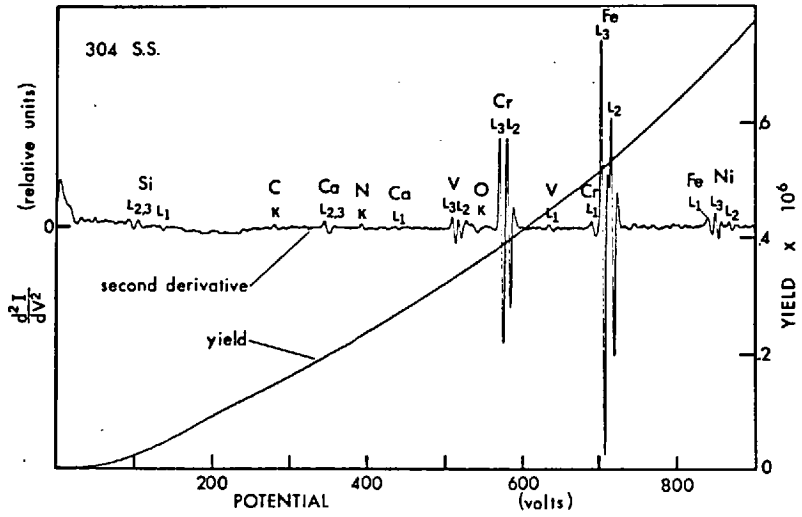

The extraction of core-level excitation edges of 304 stainless steel from the bremsstrahlung background by differentiation. The total yield was measured photoelectrically. Only the Fe $L_{2,3}$ and Cr $L_{2,3}$ edges can be detected in the total yield. The second derivative of the photoelectron current was obtained by the potential modulation method using 1.25 V rms oscillation. Vanadium has been found as an impurity on every stainless steel sample examined. It has not been reported in AES studies because of the difficualty of separating it from Cr and O.

stainless steel revealing
both Cr & V

4C (Park)

effects. PH suggested[63] using the low energy edge in the manner illustrated in figure 4d making a small correction for instrumental

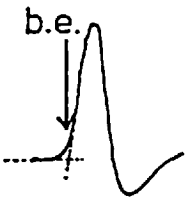

4d

broadening effects, but assuming negligible core level width. They found values for the 3d L-shells which were systematically low compared with tabulated values[64]. As was evidently noted by PH, the latter were mainly determined from X-ray data and put on an absolute scale using XPS data but where 'hard' radiation was used. This implies that the tabulated values correspond to determinations for 'bulk' material whereas APS is surface sensitive as discussed. This led PH to suggest that the difference was due to a surface shift resulting from the reduced co-ordination of surface atoms. They utilised[65] PAPS to provide some support for the existence of such an effect.

However, we showed in a Physical Review Letter[66] that the neglect of the core level width leads to a binding energy which is inconsistent with the XPS peak, and accounted in part for the PH low values. Writing the excitation probability to take account of a core level function of finite width gives

$$P(E_1) \alpha \int_{E_c=-E_1}^{0} \int_{E'=0}^{E_1+E_C} N_i(E_C)\, N(E')\, N(E_1 + E_C - E')\, dE'\, dE_C$$

where N_i is the function representing the core level density of states. The difficulty involved in finding a point on the APS threshold to correspond to the XPS peak can be illustrated by two extreme approximations. Either (A) it is assumed that $N_i(E_C)$ can be taken as a δ function in which case the PH interpretation follows or (B) because of the large density of unfilled d states at the Fermi level

in transition elements N(E') can be approximated to a δ function. In the latter case, however, the APS threshold though appearing qualitatively similar would represent the derivative of N_i and a quite different binding energy interpretation is necessitated as shown in figure 4e. As would be expected the XPS peak is intermediate between the two, but a comparison is facilitated by noting that the Fermi level is expected to be rather sharper than the core level. Figure 4f shows the superimposed APS and derivative XPS spectra for iron and nickel L_3 levels, and there is indeed close agreement within experimental error along the low energy edge where, because of the sharp Fermi level, core level effects are expected to dominate in APS as well as XPS. At higher energies deviations occur when final state effects become the more important in APS.

Despite the agreement of the low energy edges seen in figure 4f, binding energies determined from the XPS peak and APS threshold and listed in figure 4g differ significantly. This implies that the neglect of the core level width is not justified in determining binding energies from APS thresholds and there is no straightforward method of obtaining a value consistent with the XPS peak.

Since soft (AlKα) X-radiation was used for the XPS measurements, a similar degree of surface sensitivity should be seen in both cases. The influence of such an effect as a 'surface shift' on the XPS data, however, will depend upon the proportion of surface atoms which contribute. If, for example,it is assumed that the inelastic mean free path is 10 Å then this would imply about 20% contribution from surface atoms. The effect on XPS spectra would be a broadening of the observed core level rather than a significant displacement of the peak. In APS the threshold would be expected to shift to lower binding energy.

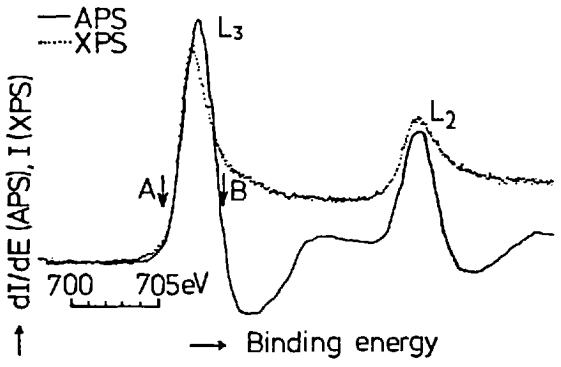

4e

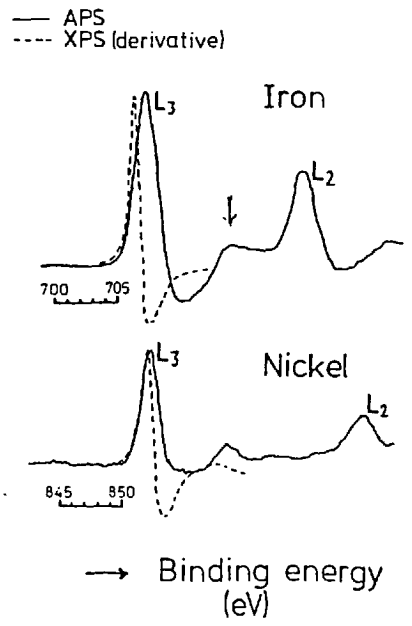

4f

	PH (APS)	WW (APS using PH method)	WW (XPS)	BB (tables)
Fe	706.3±0.5	705.8±0.5	707.1±0.5	708.1±0.9
Ni	850.9±0.5	850.8±0.5	852.8±0.5	854.7±0.4

4g

(Webb & Williams)

4.4.1 Chemical Shifts

Recently Ertl and Wandelt[67] have applied and amplified these ideas in a study of the oxidation of iron using APS and XPS. They observed that in XPS the observed core level is broader for the oxide than the metal so that while the peak position shifts by 3.5 eV the core level threshold changes by only 1.7 eV. This still differs from the observed threshold shift in APS of only 0.5 eV. They pointed out, however, that, in figure 4f, the agreement along the edge is slightly less precise for iron than nickel. This 'slow onset' in Fe realtive to Ni they correlated with a minimum in the calculated density of states for iron close to the Fermi level and were then able to completely reconcile the different shifts seen in APS and XPS. Assuming the self-convolution model they calculated the expected threshold shapes for Fe and Ni, obtaining good qualitative agreement with those observed, using theoretical densities of states.

Ertl and Wandelt also drew attention to the satellite arrowed in figure 4f, suggesting that this is sensitive to surface cleanliness. They noted, correctly, that this is weaker in the spectrum of Park and Houston[63], but also suggested that it is weaker in the data of figure 4f. In fact, this and their figure 4 are, somewhat fortuitously, plotted over almost identical energy and intensity scales facilitating comparison, and they do in fact superimpose with a high degree of precision including the satellite.

In addition Ertl and Wandelt obtained spectra for the $M_{2,3}$ level. Although they apparently did not notice, this spectrum is unique in that it commences with a negative rather than a positive step. It is intriguing to recall that the sign of this step was found in 3.1.2 to depend upon $\{\omega E_\nu - kZE_1^2\}$ suggesting that this $M_{2,3}$ spectrum is the first observation of a negative sign for this term. This is in accord with a much smaller fluorescence yield[57]

($\sim 10^{-5}$) for this level.

4.5 Further Oxidation Studies of Transition Metals

The APS of clean 3d transition elements were studied by Park and Houston[63] in a paper which provides a comprehensive collection of spectra for the L shells of these elements. They found that the expected trend of peak width - i.e. a narrowing for Sc → Ni as the width of the unfilled part of the d band narrows - was obeyed. They also demonstrated in a further paper[68] the sensitivity of APS threshold shapes to chemical environment, by oxidising Ti, Cr and Ni. Chemical shifts occur and for Cr there is a noticeable broadening which they associate[8] with the removal of d electrons by O. In the case of Ti a doublet structure develops for both L_3 and L_2 thresholds which may be due to the presence of atoms in two chemical states.

Recently Andersson and Nyberg[69] have undertaken better controlled studies of the oxidation of Ti, Cr, Ni and Fe and their spectra for O 1s and metal 2p levels at light exposures of O_2 are shown in figure 4h together with the O 1s spectra at much heavier exposures. In the former case they point out that the metal 2p spectra are very similar to those of PH[63] for clean metals though the Ti one shows better resolution. For this light exposure the oxygen spectra are characterised by a single peak which shifts and broadens in systematic fashion. These spectra they identify with the state in which O is chemisorbed on the metal surface and the width of the oxygen peak is seen to be correlated with, though not equal to, the width of the metal 2p peak. This they assign not to cross transitions to metal d states but to a mixing of 3d and 2p states. At longer oxygen exposures the O 1s spectra become extremely complex differing markedly for the different

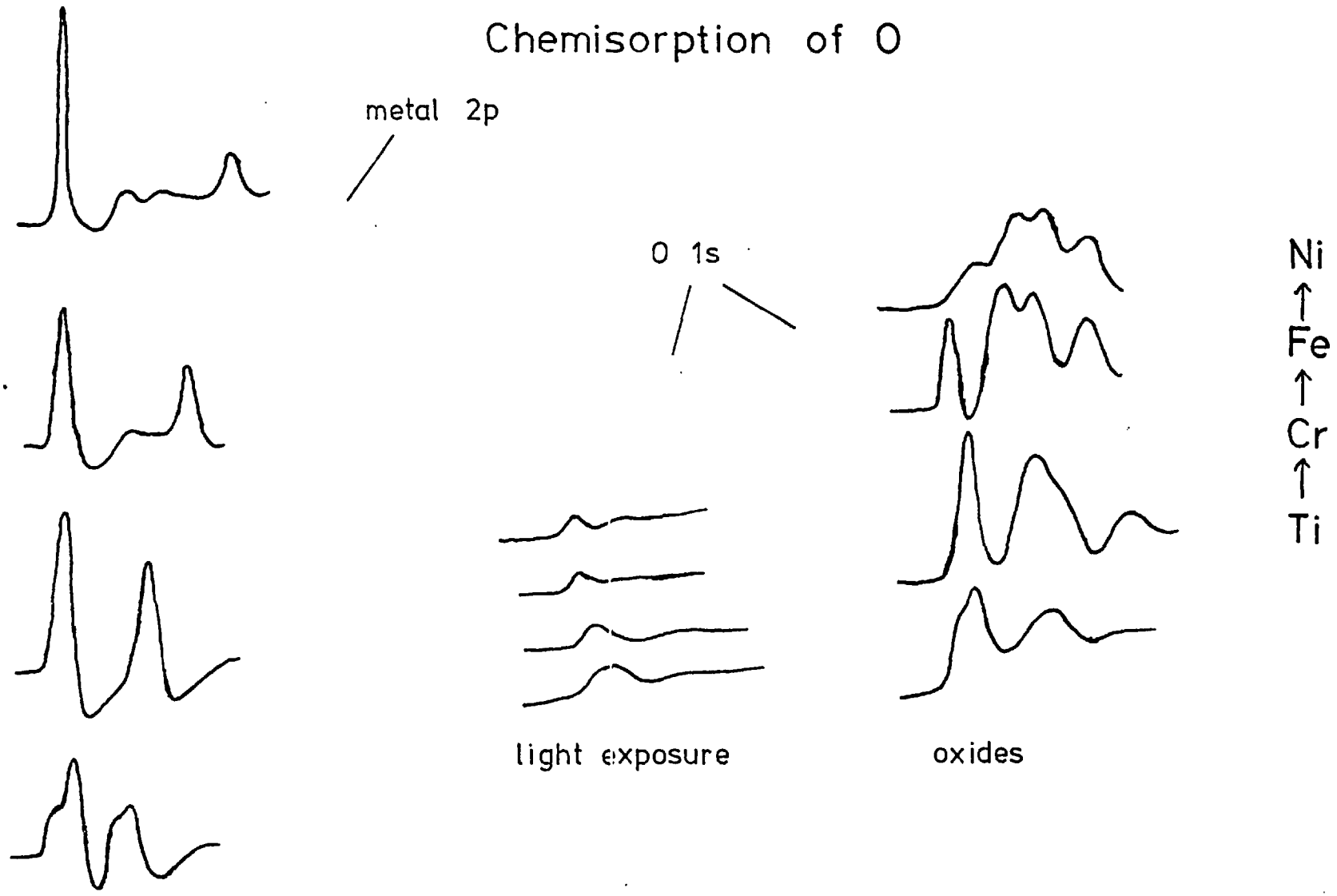

4h (Anderson & Nyberg)

metals and are associated with the formation of oxides. They do not attempt to account for these spectra, but dismiss a plasmon loss argument because the peaks are irregularly spaced. A spectrum obtained from cleaved V_2O_5 is shown in figure 4i. The $V(L_{2,3})$ and O thresholds are very close but the complex role of O is elucidated by comparison with the V L_1.

Ertl and Wandelt[70] have obtained a sequence of nickel 2p spectra during the formation of the surface oxide and these results are shown in figure 4j together with a model for the electronic structures of Ni and NiO due to Adler and Feinleib[71]. In metallic nickel the Fermi level lies near the top of the narrow d band; in the oxide the 3d states are apparently strongly localised and correlation effects play an important role making a one-electron picture inappropriate. Thus while the O 2p and Ni 4s levels form bands as shown to the left, the 3d levels are represented by Adler and Feinleib as 'quasi-particle' states. The $3d^7$+$3d^9$ states represent the energy of excitation of an electron from a $3d^8$ state to a neighbouring nickel atom.

Ertl and Wandelt's spectra show that the L_3 threshold shapes differ in two main respects between Ni and NiO. In the latter there is a pronounced negative dip following the L_3 peak and the series also shows the growth of the peak 'C'. They associate the peak C with the $3d^7d^9$ states suggesting it may either be due to a direct core electron transition to such states or due to multiple excitation including the transition d^8+d^8 → d^7+d^9, analogous to loss peaks originating from interband excitations. The presence of the negative dip in the oxide case is associated with the separation of the 4s band from the 3d states. As can be seen in figure 4k for a simple model the effect of overlapping d and s bands is to reduce the negative dip.

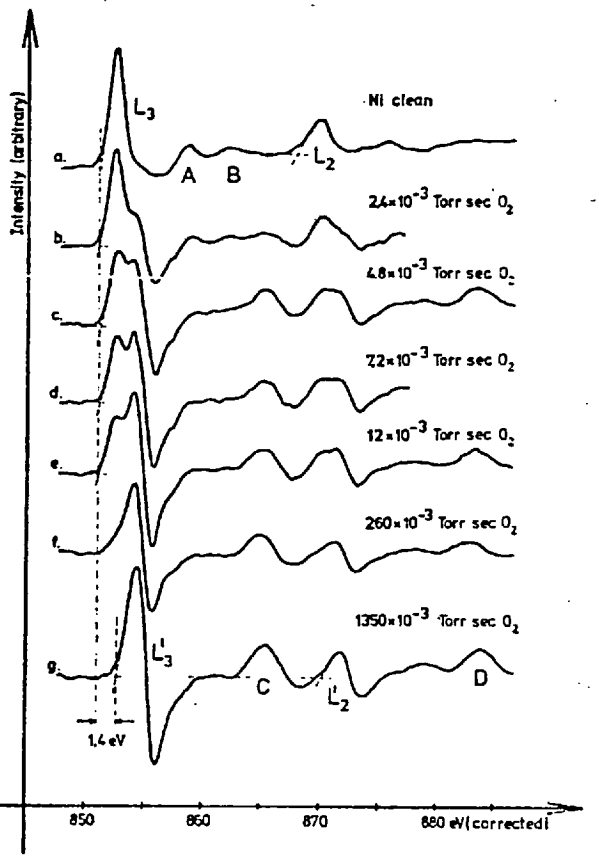

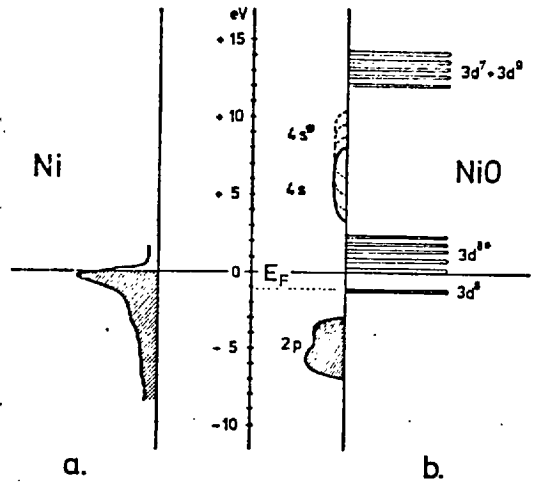

4j

(Ertl & Wandelt)

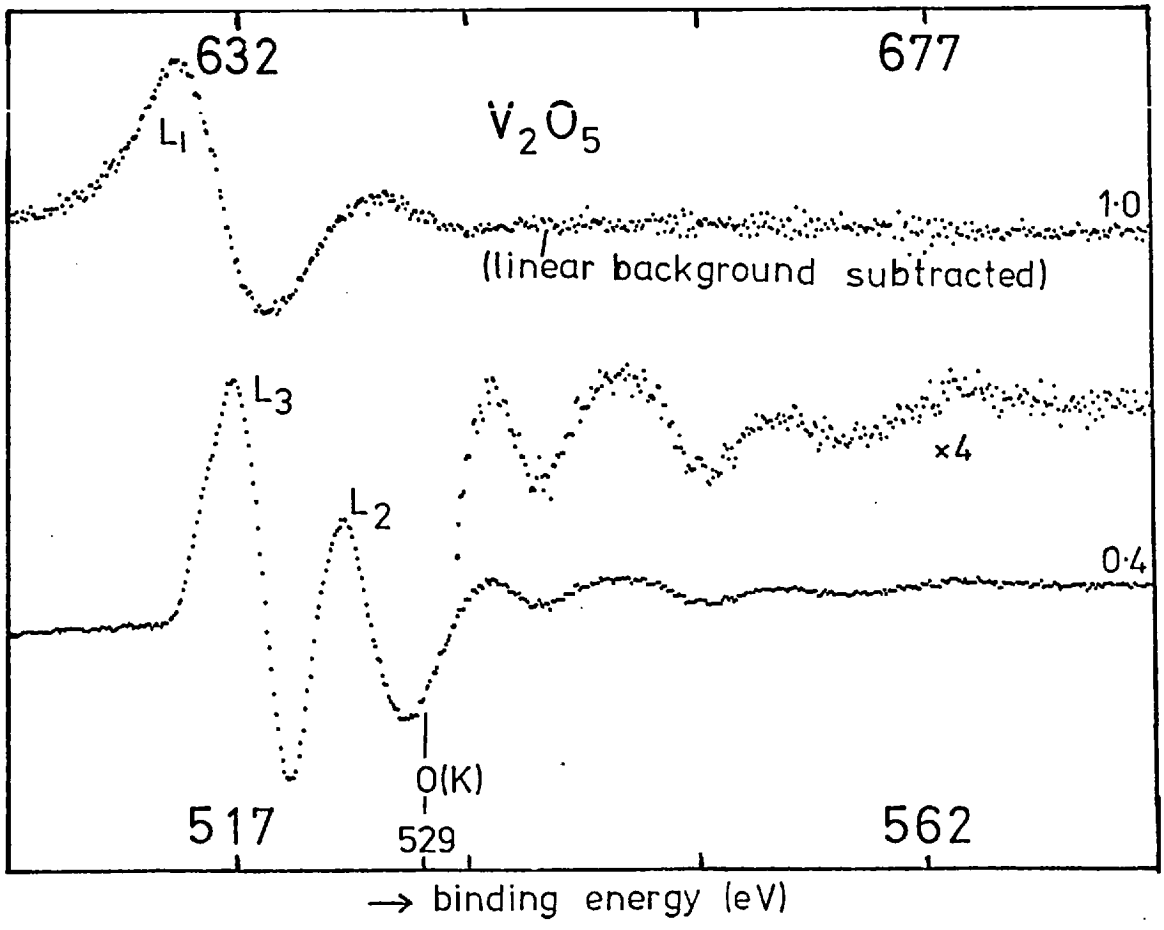

4i

Overlapping d and s bands

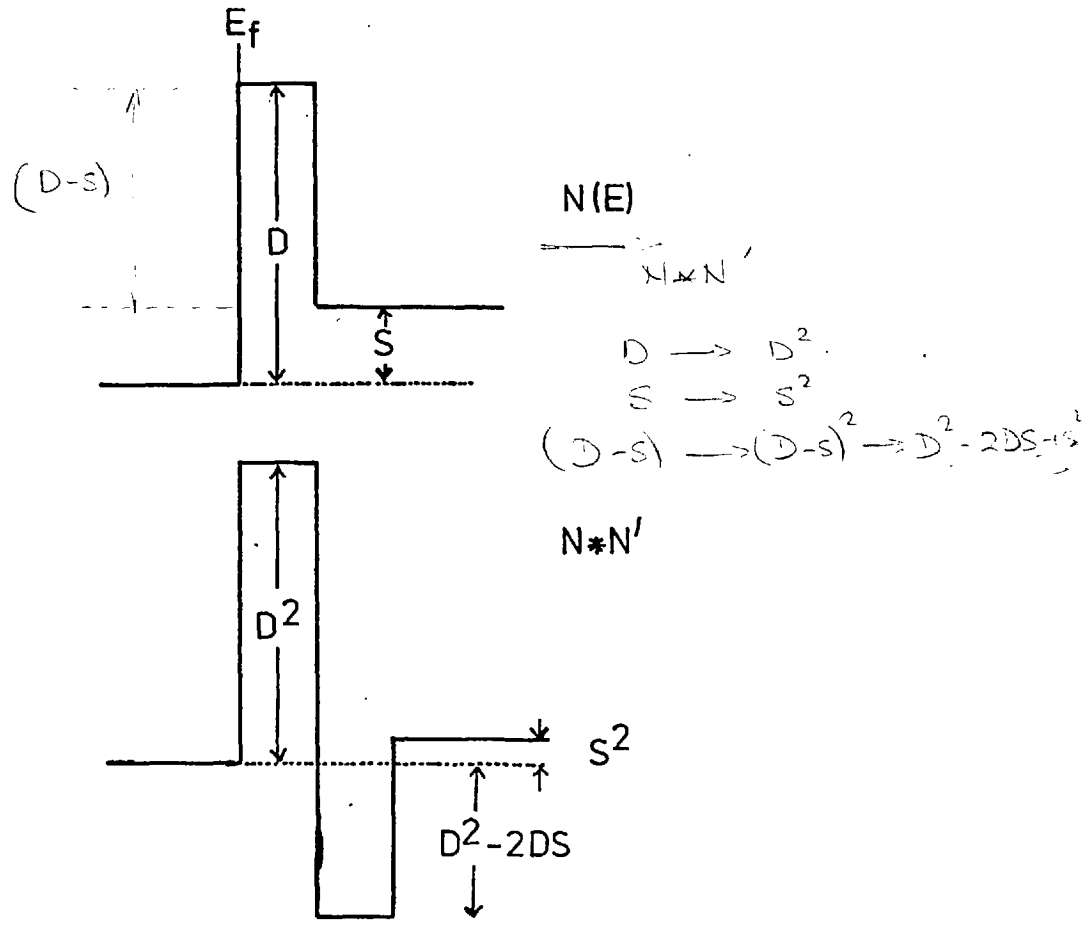

4k

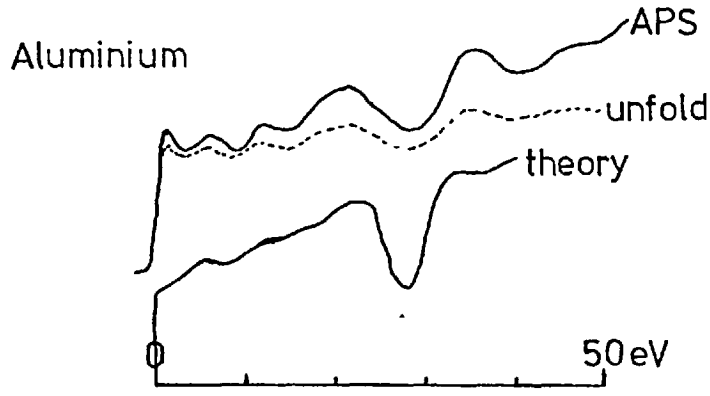

4l (Nilsson & Kanski)

4.6 APS of simple metals

While there has been a tendency to concentrate on transition elements, Nilsson and Kanski[72] have obtained good AP spectra of the light simple metals Al, Mg and Be. We have seen that the APS threshold can be approximated by

$$A(E) \quad \alpha \quad \frac{d}{dE} \int_0^E N(E') \, N(E - E') \, dE' \qquad \ldots.(1)$$

where N(E') is the unfilled desnity of states function. If N(E') is a step function then differentiating its self-convolute restores the step function. Thus for simple metals where the main sharp structure in N(E') is the Fermi edge the APS threshold is directly comparable with N(E') to a first approximation. Explicitly (1) can be rewritten[73]:

$$A(E) \quad \alpha \quad N(E) \, N(0) \quad + \quad \int_0^E N(E') \, \frac{d}{dE} N(E-E') \, dE'$$

The first term actually only arises because the upper limit is E but could equally well be $E + \varepsilon$ in which case the first term becomes $N(E+\varepsilon) \, N(-\varepsilon) = 0$. Thus it is the second term not the first[72] which is to be retained.

The net effect is that the order of integration and differentiation in (1) can be interchanged and to the extent that $\frac{d}{dE} N(E-E')$ can be replaced by a δ function (a good approximation for a simple metal) we have $A(E) \sim N(E)$.

Nilsson and Kanski's results for Al are shown in figure 41 where the APS, its unfold, and the calculated d.o.s. are seen to be in good agreement. They also found excellent correlation with soft X-ray absorption spectra for all three elements, and associated a 'slow onset' for Be with a minimum in the density of states in the Fermi level as in the case of iron[67]. They further identified

features in the Mg and Be spectra as due to plasmon losses but could not identify a plasmon loss for Al. As can be seen in figure 41 there is a peak at threshold not predicted by calculation, and this, they speculate, may be a threshold singularity of the type predicted by Laramore[10].

4.7 APS of Rare Earth Elements

As described in section 3.3.4, in rare earth elements the characteristic X-ray emission is overshadowed by what effectively constitutes a resonance of the bremsstralhlung background[41] and the self-convolution model would not be expected to apply for these f-shell elements.

Chamberlain and Baun[74] (CB) have obtained SXAP spectra for samarium and their $M_{4,5}$ spectrum is reproduced in figure 4m. The M_5 threshold has a doublet structure while only a single peak is observed for the M_4 level.

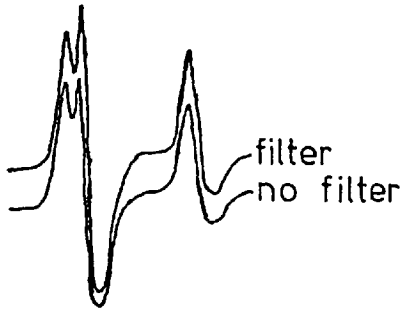

4m (Chamberlain & Baun)

The different weightings of the two M_5 components when using an X-ray filter indicates that different photon energies are responsible for the two contributions. The overall M_5 width is clearly greater than the M_4 so that Coster-Kronig broadening could not be invoked to explain the lack of structure in the latter. CB argue that the higher energy of the two M_5 peaks is due to a resonance of the type observed in X-ray emission for La[41] and Ce[42]. They further point out that

the doublet is found only for $N_5(4d_{5/2})$ and $M_5(3d_{5/2})$ levels of the eight observed, and suggest that this implies the resonance is associated with transitions to $4f_{7/2}$ states which obey dipole selection rules. Implicit in CB's argument is the assumption that transitions to $4f_{5/2}$ states are not possible these presumably being occupied in Sm which has just 6 f electrons. Thus while the resonance is associated with both the M_5 and M_4 levels in La(f^0) and Ce(f^1) it would not be expected for the M_4 in Sm which is in accord with CB's interpretation. However, CB do not actually show their $N_{4,5}$ spectrum and in view of (a) these being unresolved levels according to tables[64] and (b) the complex structure seen over a wide energy range in Gd[75] and La[76], it is difficult to see how it was possible to unambiguously identify the N_5 as a doublet and the N_4 as a singlet.

Murthy and Redlead[75] (MR) have obtained SXAP spectra for La, Gd and Th (the last being an actinide). Their spectra for the $M_{4,5}$ and $N_{4,5}$ in La and $M_{4,5}$ in Gd are shown in figure 4n where the broken curves show the effect of oxidation; in fact, the changes brought about by O_2 are small relative to observations on the 3d transition elements. This may reflect the non-participation of f electrons in chemical bonding as demonstrated by the very similar chemical properties of the lanthanides. MR observe small satellite peaks associated with the M_5 and M_4 levels in La which were not observed in a previous study[54]; these are denoted M_5' and M_4'. It is possible that these could be assigned to separate characteristic and resonance contributions in the manner of CB; though the sub-threshold nature of the resonance in La[41] would imply that the order would have to be reversed and the main first peak associated with the resonant emission. In fact, MR's data for Gd (heavier than Sm) bears a much closer resemblance to the La spectrum that Sm and it seems likely that CB's arguments represent an oversimplification.

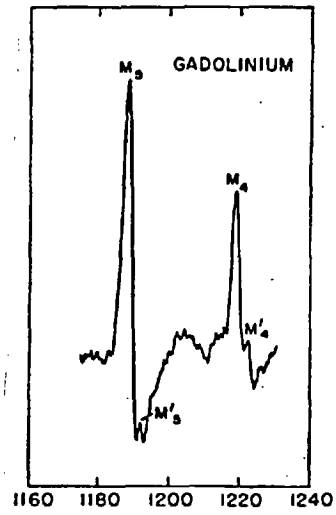

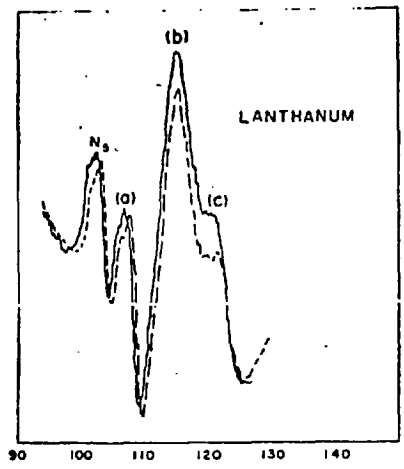

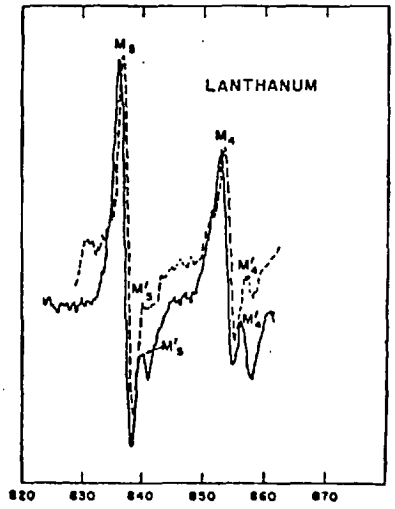

4n (Murthy & Redhead)

Szczpanek and Harte[77] (SH) have obtained the $N_{4,5}$ spectrum for La which is in good agreement with MR's apart from a different background. They note that the extended structure ($\sim$ 30 eV) seen is similar to that found in photoabsorption experiments. The latter has been accounted for by Sugar[78] whose calculations agreed well with experiment. He explains the structure as due to strong overlap between 4d and 4f orbitals resulting in a strong exchange interaction and marked configurational energy dependence of the final $4d^9f^{n+1}$ state. SH note that while a similar argument probably applies in SXAPS an additional electron has to be accounted for.

Nilsson, Kanski and Wendin[79] have discussed the possibility of many electron effects in the $N_{4,5}$ spectrum of barium (adjacent to La but not strictly a lanthanide); Wendin[80] has previously suggested the existence of a 'giant dipole resonance' to explain the photo-absorption spectra of barium.

Less attention has been paid to the actinide series though MR show the $O_{5,4}$ spectrum for thorium and PH[81] the $N_{7,6}$ threshold for uranium. These are reproduced in figure 4o. PH's spectrum for U closely resembles CB's for Sm. However dipole transitions between 4f and 5f states are not allowed so CB's explanation could not be invoked. PH suggested that the N_7 structure is due to a doubly peaked density of states function washed out in the N_6 by Coster-Kronig processes. That the N_6 is also split at higher resolution as indicated by studies being undertaken currently[82] would tend to support this possibility. In general, however, APS of rare earth elements do not seem to be very well understood at present.

4.8 Summary

Some improvements in APS designs have evolved, in particular the use of X-ray filters are advantageous for deeper core levels

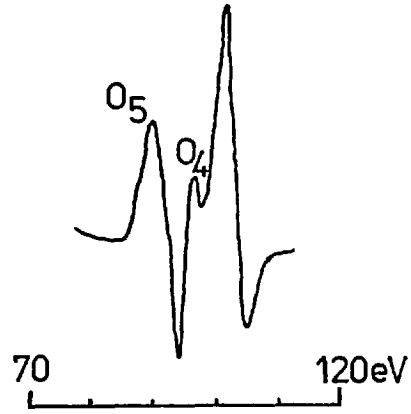

Thorium (Murthy & Redhead)

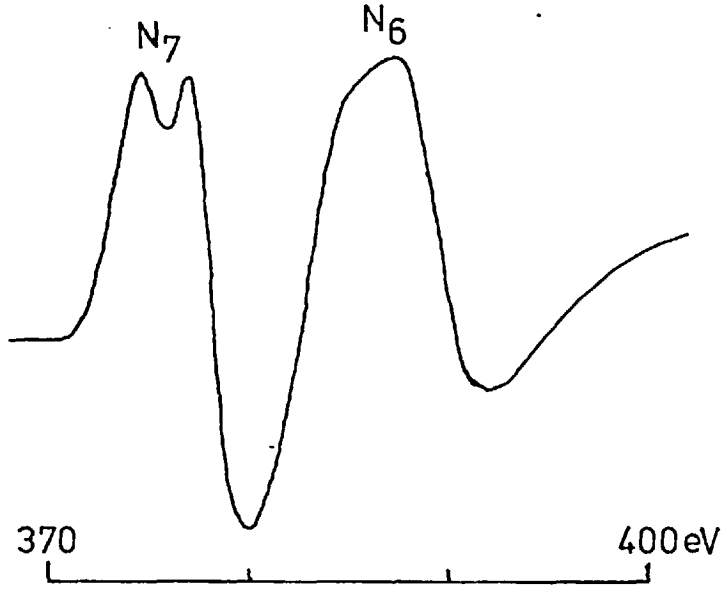

Uranium (Park & Houston)

where in normal APS set-ups noise becomes a problem. The variations in sensitivity to different elements of APS mean that it cannot be universally applied to surface analysis though it can be advantageous for some applications. Absolute binding energies cannot be straightforwardly determined though comparisons are possible with care. It has been demonstrated that APS can be usefully employed in studying light and transition elements and has also been used to study the oxidation of the latter. The interpretation of the APS of rare earth elements is complicated by the occurrence of resonance emission.

CHAPTER 5

DECONVOLUTION

5.1 The Problem

As shown in 3.1 it is desirable when interpreting APS spectra to be able to solve the equation:

$$A(E) = \frac{d}{dE} \int_0^E N(E')\, N(E-E')\, dE' \qquad \ldots.(1)$$

This represents a self-convolution of the unfilled desnity of states function N(E'), which it is hoped can be derived from a knowledge of A(E). This type of problem is frequently found in other situations in experimental physics. The most usual form of the problem is that an instrument is to be used to attempt a measurement of some function f(x), but the obtained function is g(x) where

$$g(x) = \int f(x')\, s(x-x')\, dx' \qquad \ldots.(2)$$

which can be abbreviated $g = f*s$.

Here s is the 'instrumental response function' i.e. if f(x) is actually a δ function $\delta(x-x_0)$, the observed function is just $g(x) = s(x-x_0)$. The width of s is a measure of the resolution of the instrument.

It is convenient to discuss deconvolution in form (2) initially where f and s are distinguished but the basic points apply to (1) equally well. In principle, it is possible to solve (2) by taking the Fourier transform so that using the standard result for the transform of a convolution product.

$$\bar{g} = \bar{f} \times \bar{s} \qquad \ldots.(3)$$

where $\bar{g}(\nu) = \int g(x) \exp(-i\nu x)\, dx$ ....(4)

If (3) is divided by $\bar{s}$ and the inverse transform taken then f is found precisely. Unfortunately the precise solution to a deconvolution problem is rarely of any use. The difficulty is that the instrument is unable even to measure g exactly; the data always contains noise or small distortions. Now referring to (2) we see that g is the convolution product of f with s, and the effect of 'folding' f with s is to smooth f. So if, after smoothing, g contains noise then f must have contained a lot more noise. Alternatively we can say that s has finite width and thus the extent of $\bar{s}$ in frequency space is also finite and $\bar{s}(\nu) \to 0$ as $\nu \to \infty$. If the noise in g is random however it extends to high frequencies and when we divide $\bar{g}$ by $\bar{s}$ the effect is to divide the unwanted high frequency components by zero and greatly amplify them. The exact solution to a deconvolution problem consists usually of meaningless noise.

5.2 Methods of Solution

Any deconvolution routine must involve approximation since the 'mathematical' solution is physically unreal. Further all methods incorporate subjective decisions in one form or another. As noted by Paatero et al.[83] deconvolution methods which may work well in one field often contain subjective decisions in an implicit form so that when the method is tried elsewhere it fails. It is perhaps for this reason that there are so many different methods described in the literature, most of which claim to be the panacea while themselves being criticised by all the others. It is probably more reasonable to suppose that any one group has given the required degree of attention to only one method, but that alternative approaches would have been viable with sufficient care. That is undoubtedly true in the present case and below is given only a brief resume of some

alternative methods with a view to extracting one or two points of value before discussing the iterative routine used in greater detail.

5.2.1 Fourier Transform

The basis of this approach was described in 5.1, but its use in that 'raw' state leads to catastrophe. It is necessary to incorporate a high frequency cut-off above some frequency ν_0 where ν_0 is determined at a point such that $\bar{g}$ is of the same order as the noise level[84]. Ultimately any deconvolution routine must provide these two functions - invert and chop the high frequencies. Undesirable effects can result from a sharp (hard) cut-off and the method can be further refined by softening this[84]. Paatero et al.[83] discuss a method of 'generalised least squares' which they say is equivalent to the transform method with a soft cut-off.

5.2.2 Sequential Calculation

Self-convolutions occur when a transition simultaneously involves two electrons; apart from APS the results of Auger Electron Spectroscopy[85] (AES) and Ion Neutralisation Spectroscopy[86] (INS) can also be interpreted as a density of states self-convolution. Hagstrum and Becker[87] in a paper grandly entitled 'The Interrelation of Physics and Mathematics in INS' describe a sequential calculation method whose basis is as follows: Writing the integral of (1) in digital form (omitting the differentiation)

$$g_i = \sum_j^{i-1} f_{i-j} f_j \qquad \ldots.(5)$$

where we suppose $f_i = 0$ for $i \leq 0$.

Then $g_0 = g_1 = 0$

$$g_2 = f_1^2 \qquad \ldots.(6)$$

$$g_3 = 2\, f_1\, f_2 \qquad \ldots.(7)$$

$$g_4 = 2\, f_1\, f_3 + f_2^2 \qquad \ldots.(8)$$

etc.

In general we can rewrite (5) more usefully

$$g_i = 2\, f_1\, f_{i-1} + \sum_{j=2}^{i-2} f_{i-j}\, f_j \qquad \text{for } i \geq 4 \qquad \ldots.(9)$$

Now f_1 can be found from the first non-zero datum point using (6) i.e. $f_1 = \sqrt{g_2}$ (g_2 is the first non-zero datum point in this notation). f_2 is then found using (7) since f_1 is now known and each point calculated sequentially from (9) in gneral since the summation is always in terms of already known f's.

$$\text{i.e.} \quad f_{i-1} = \frac{1}{2f_1} \{ g_{i+1} - \sum \} \qquad \ldots.(10)$$

This method was briefly tried but gave only 'wild' noise. This might have been anticipated since the solution is the same 'mathematical' one that we have said is 'physically unreal'. The method does, however, provide some insight into what is meant by this statement. In (10) the term {....} is the small difference of two large numbers. Any samll errors in the already calculated f's, perhaps even computer rounding erros, may induce drastic errors in subsequent ones. So the derived 'mathematical' solution with its high noise level actually must consist of accurately known numbers. Hagstrum and Becker[87] describe procedures which, no doubt, correct these undesirable effects but also must introduce approximations.

A further point the method illustrates is that, in principle,

we can calculate as many f's as we know g's. Physically, with reference to APS process, this is closely related to the fact that, if the incident electron has excess energy E over that required to excite a core electron, then neither final state can lie above E since energy conservation would then demand that the other final state be below the Fermi level. Thus over a threshold of width ΔE the information pertains to the density of states up ΔE above E_f but it is not influenced by whatever the density of states may be above.

5.3 The Iterative Solution

This was the method adopted for solving (1) and is now considered in greater detail again in connection with (2) initially. The idea is to form the (n+1)th approximation to f from the nth by the equation

$$f_{n+1} = f_n + (g - f_n * s) \qquad \ldots.(11)$$

The difference between g and $f_n * s$ is added to f_n; clearly it converges in the sense that if $f_n = f$ then $g = f_n * s$ and the bracketed term is zero. Figure 5a also demonstrates that this is

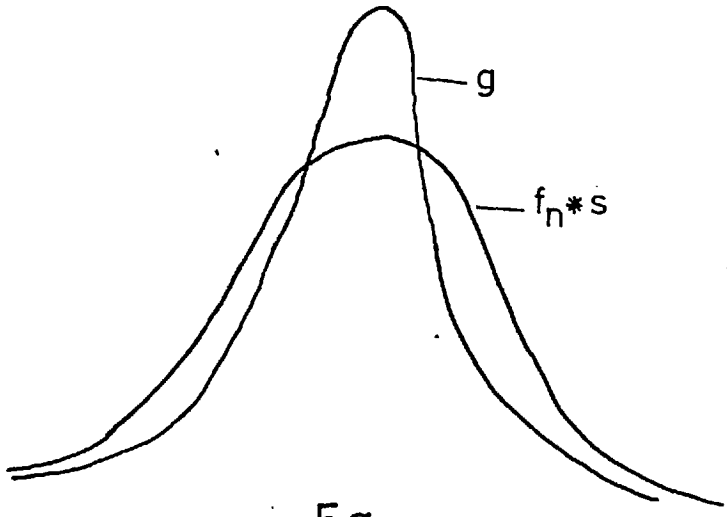

5a

a physically reasonable correction since if $f_n * s$ is too broad $(g - f_n * s)$ is +ve close to the peak centre and -ve in the 'wings' and f_{n+1} is sharpened.

5.3.1 Analysis

The method has been analysed harmonically by Jones and Misell[84]. f_n can be written

$$f_n = g + g \sum_{r=1}^{n-1} (1 - *s)^r \qquad \ldots.(12)$$

(Proof is by induction)

Taking the transform of (12) and incorporating g in the sum gives

$$\bar{f}_n = \bar{g} \sum_{r=0}^{n-1} (1 - \bar{s})^r$$

This is just a geometrical progression which summed gives

$$\bar{s}\,\bar{f}_n = \bar{g} - \bar{g}\,(1 - \bar{s})^n \qquad \ldots.(13)$$

Thus $\bar{f}_n \to \bar{f}$ as $n \to \infty$ provided $(1 - \bar{s})^n \to 0$ as $n \to \infty$

i.e. $|1 - \bar{s}| < 1$

In practice, however, we do not want f to contain the erroneous high frequency components and effective convergence is achieved for some n such that

$$(1 - \bar{s}(\nu))^n \simeq \begin{cases} 0 & \text{for small } \nu \\ 1 & \text{for large } \nu \end{cases}$$

Jones and Misell note that if s is normalised i.e.

$$\int_{-\infty}^{\infty} s(x)\,dx = 1$$

then $\bar{s}(0) = 1$ and $\bar{s}(\nu)$ should be close to 1 for small ν so satisfying $(1 - \bar{s})^n \simeq 0$.

For the high frequencies at sufficiently small n and $\bar{s}$

$$(1 - \bar{s})^n \simeq 1 - n\bar{s}$$

and putting this in (13) gives for large ν

$$\bar{f}_n(\nu) \simeq n\,\bar{g}(\nu)$$

This shows that the high frequency components are amplified proportionately to the number of iterations. Initially, when using this method, there is convergence, but eventually noise becomes visibly large and divergence occurs. This behaviour has been noted by a number of workers[88] as well as in the present studies. In practice some form of smoothing has to be incorporated.

5.3.2 The Central Point

It is relevant to the practical application of the iterative method to consider how the correction made during each iteration produces a 'better' estimate of the required function. Again for a digital convolution we write:

$$g_{ni} = \sum_j s_{i-j} f_{nj} \qquad \ldots\ldots(14)$$

where g_n is the nth attempt at g calculated from the nth trial function f_n. The (n+1)th trial function is

$$f_{(n+1)i} = f_{ni} + g_i - g_{ni} \qquad \ldots\ldots(15)$$

The basic question is why should $f_{(n+1)i}$ defined in (15) be better than f_{ni}? Reference to (14) shows that in calculating a particular g_{ni} there are contributions from many of the f's (depending on the width of s), but when the correction is made according to (15)

only f_{ni} is modified by the error in g_{ni}.

The other f's are also adjusted and will affect the value of $g_{(n+1)i}$ but generally in essentially random fashion. Some iterative methods[89] form the difference function $(g - g_n)$ and then smooth it so correlating the points of the difference function. In practice there will be some correlation anyway unless $(g - g_n)$ is comparable with the noise level, but in that case convergence has effectively been achieved. It is convenient to ignore this correlation here since it does not alter the conclusion.

The main 'coherent' contribution to the correction to f_{ni} comes from the contribution to g_{ni} from f_{ni} in (14),

$$\text{i.e.} \qquad \delta g_{ni} = s_0 f_{ni}$$

If, for example, g_{ni} is too small $f_{(n+1)i} > f_{ni}$ and hence $g_{(n+1)i}$ is increased over g_{ni} by an amount

$$\delta g_{(n+1)i} - \delta g_{ni} = s_0 (f_{(n+1)i} - f_{ni})$$

+ other 'random' terms.

Hence for the maximum 'coherent feedback' we need to choose s_0 at the maximum of s. This was probably done automatically by other users of the interative method, but these considerations become relevant when the data represents a derivative spectrum and the choice of s_0 is less obvious. In this case before comparing g_n with g we differentiate

$$\text{i.e.} \quad g'_{ni} = g_{n(i+1)} - g_{ni}$$

and the contribution to g'_{ni} from f_{ni} is

$$\delta g'_{ni} = f_{ni} \{s_1 - s_0\}$$

The 'centre' is now chosen so that s_0 occurs at the maximum slope of s to maximise {....}.

5.4 Application of the Iterative Solution to the Self-Convolution Case

The self-convolution case is not amenable to the harmonic analysis of Jones and Misell. The following, however, serves to demonstrate that the basic points are as above.

We write

$$g = g_T + \varepsilon \qquad \ldots.(16)$$

and

$$f_n = f_T + E_n \qquad \ldots.(17)$$

Here g_T is the 'true' function that would be measured by an ideal instrument and ε represents noise, distortions etc. E_n is the error in the nth try and we have

$$g_T = f_T * f_T' \qquad \ldots.(18)$$

f_T being the 'true' deconvolute. It is assumed that g is in derivative form and the order of differentiation and integration has been reversed as in 4.6.

The (n+1)th trial function is calculated according to:

$$f_{n+1} = f_n + k\{g - f_n * f_n'\} \qquad \ldots.(19)$$

When the derivative is taken, g_n is more sensitive to small changes in f_n; thus it is found experimentally necessary to incorporate a scaling constant k (< 1 and in fact normally $k = \frac{1}{8}$) to prevent erratic adjustments to f_n if the first guess is not close to f_T.

Now substituting (16) and (17) in (19) and using (18)

$$f_{n+1} = f_T + E_n + k\{\varepsilon - E_n * f_T' - E_n' * f_n\} \qquad \ldots.(20)$$

The first term in {....} shows again that at each iteration the noise in g is added to f_n, and the last term probably has only a small randomising effect since E'_n will typically be a rapidly oscillating function which is smoothed by f_n. Then the effective adjustment originates from $E_n * f'_T$. If f'_T is close to a δ function (with k = 1) (20) reduces to:

$$f_{n+1} \simeq f_T + (\text{noise})$$

For rapid convergence we need f'_n to look as close as possible to a δ function and thus must choose the centre at the maximum slope of the leading edge of f_T, but provided $E_n * f'_T$ has the same sign as E_n then convergence is achieved. Since f_T is not known initially the first choice of 'centre' may have to be adjusted for rapid convergence.

5.5 The Scheme Used

As noted above the (n+1)th trial function is calculated according to:

$$f_{n+1} = f_n + k \{g - f_n * f'_n\} \qquad \ldots.(21)$$

where g is the original data (in derivative form) and f is interpreted as the unfilled density of states function. The correction is scaled by the parameter k whose value is not critical.

As alternative method of proceeding, which would have kept a closer parallel with the approach of 5.3, would be to integrate the data and match g to $f_n * f_n$. The above method was chosen since matching derivatives provides a keener test of accuracy and probably gives faster convergence.

As already mentioned, a problem originates from the feedback of noise to the trial function and ultimately results in divergence.

This is troublesome but can be overcome in straightforward fashion by smoothing f_n when divergence begins. In order to quantify the 'accuracy of the match' the function

$$M_n = \sum_i \{g - f_n * f'_n\}_i^2$$

is calculated at each iteration and compared with M_{n-1}. If M_n increases m times (m = 3 usually) in succession the smooth is triggered. A 3-point smoothing routine was arranged

$$\text{i.e. } f_{n+1} = \tfrac{1}{2} f_n + \tfrac{1}{4} (f_{n-1} + f_{n+1})$$

This is actually operated several (usually 4) times, though again this is fairly arbitrary. The result is that M_n is usually increased but the divergence summarily halted and M_n then proceeds to a new 'low' before divergence occurs again.

Effective convergence is obtained when the deviations between g and $f_n * f'_n$ are comparable to the noise in g. This is usually obtained in something $\sim$ 100 iterations. The form of f_n is then insensitive to the point at which iteration is stopped and this is not usually done until f_n has remained essentially unchanged for a fairly large number of iterations.

5.5.1 Computation

Details of the actual programme are given in the Appendix; it is housed in the same PDP8 mini-computer as is used for the data accumulation described in 2.3. The main disadvantage is that it is time consuming, several hours being required for the necessary iterations. The actual convolution takes up most of the cycle time; for an N point spectrum the convolution involves $\sim N^2$ multiplications each of which is done by repeated addition. The time for a single iteration varies with N and the magnitude of the numbers.

This is amply offset, however, by the convenience of having the deconvolution facility 'on site' and immediate access to the cassette storage and oscilloscope/chart recorder display facilities. The programme is controlled from the teletype and switch register with the ability to stop after any iteration and display data on the oscilloscope.

5.5.2 Setting-up Procedure

For most materials $L_{3,2}$ spectra were obtained which meant that only the L_3 threshold shape was known unambiguously and that only for a limited energy range i.e. the L_2/L_3 spacing. It is generally convenient to assume that the positive part of the L_3 threshold is all that is known unambiguously (which is approximately so) since it simplifies computation not to have negative numbers. In fact, since the positive peak is approximately the same width as the d band this is sufficient to obtain the d band density of states. As noted in 4.6 the derivative of the self-convolute approximates the original function and so the first trial function is taken to be the same positive peak as is to be matched to.

5.6 Programme Test

When the programme had been developed into its final format a test was made to determine how faithfully it could retrieve a known function. The starting function used is shown in figure 5b (trace A). The derivative of the self-convolute of A was taken and the positive peak taken in the usual way to give trace B, which was also used as the first trial function exactly as usual. It is interesting to note that the doublet feature 'X' in A is apparently lost in B. Thus this choice of starting function

Programme test

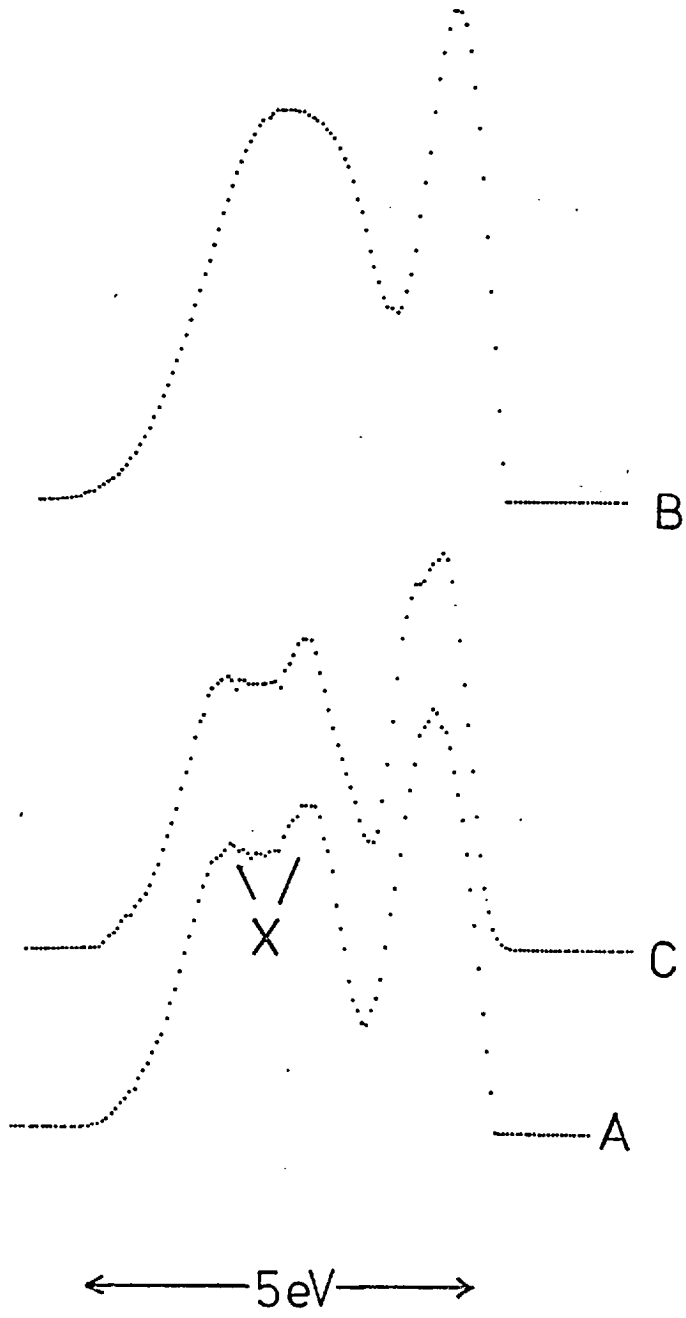

5b

represents a particularly demanding test though it was fortuitous that it was chosen.

Iteration was terminated after around 150 iterations at which time the form of the deduced original function (trace C) had remained constant over about 50 iterations. The accuracy with which the original function was retrieved is extremely satisfactory. It may be noted that there was no 'juggling' with parameters involved and the initial value of 'centre' chosen (without reference to A) proved satisfactory.

Trace B is less noisy than typical data; noise would presumably limit the accuracy with which a function can be retrieved but this test serves to illustrate the capability of the programme.

5.7 Twin Solutions

For the TiS_2 and $TiSe_2$ spectra obtained at UHV, subsidiary structure was resolved whose interpretation in terms of a density of states function has proved ambiguous. The problem is illustrated with reference to the $TiSe_2$ spectrum shown in figure 5c, where the two possible solutions for N(E) are also shown 'A' and 'B'.

From the view point of deconvolution it is interesting to note how these two solutions are arrived at. Which solution is obtained in fact depends upon the choice of 'centre' and the role of this parameter was investigated by performing the deconvolution for a range of values a, b, c, d, e, f as marked in figure 5c. In cases a and b solution A was obtained but convergence was very slow. For c, solution A was again obtained but convergence was very fast. In the case of d, although after a long time solution B was 'locked-in to' the trial function at different times resembled sometimes A and sometimes B. For e, rapid convergence to B was

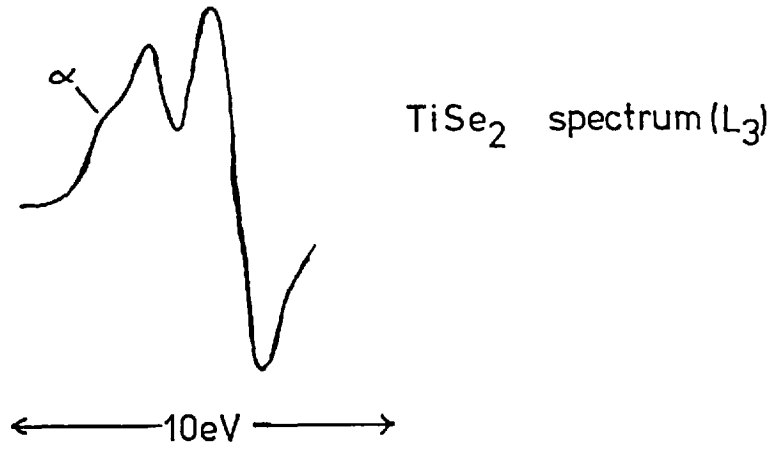
α
TiSe2 spectrum (L3)
10eV

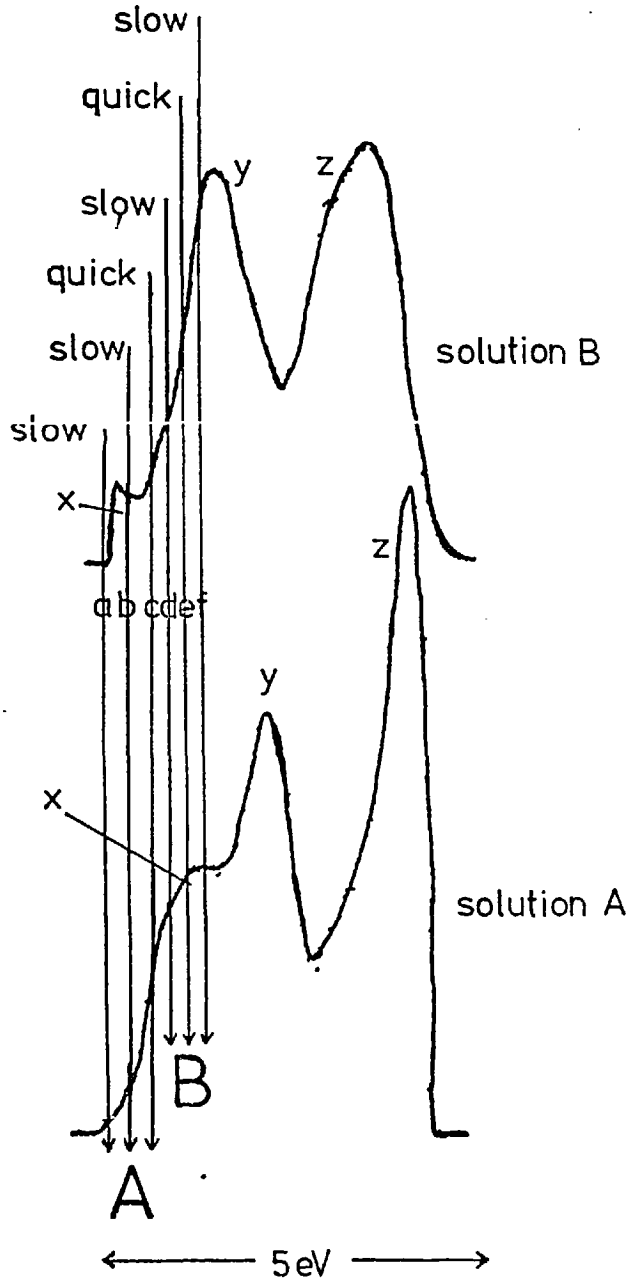
slow
quick
slow
quick
slow
slow
x
y
z
solution B
z
a b c d e f
y
x
solution A
B
A
5eV

5c

obtained while for f convergence to B was slow. These observations are summarised in figure 5c; their relationship to previous discussions is quite clear. An inflexion occurs on the leading edge and depending on whether centre occurs above or below this inflexion solution B or A is obtained. With centre close to the maximum slope in either case convergence is rapid, while with centre close to the actual inflexion point some confusion is caused.

Physically the derivation of these two solutions can be illustrated with reference to figure 5d, where the differentiated self-convolutions of A and B are shown. They arise essentially because the observed spectrum does not correspond to an exact self-convolution and neither A nor B can be regarded as completely satisfactory, since they both predict features not found in the actual spectrum.

The origin of the shoulder α in case A is the self-convolution of a similar feature, but as a consequence the convolution of z with x and y predicts structure on the second peak of the spectrum (arrowed) which is not observed. While extending the density of states to higher energies could modify the spectrum in this region, it would actually require a negative density of states to remove this feature. Mathematically reasonable though this may be it is not physically admissable.

In case B, α derives from a convolution of x with y and, because x is now much smaller and z less sharp, there is no apparent structure on the second peak of the spectrum. But the self-convolution of x now gives a tiny spurious feature (arrowed).

It is clear that there is some deviation from a quantitative self-convolution though in view of the approximations this is not very surprising. The question as to which solution we should regard as more nearly correct is fortunately not very critical

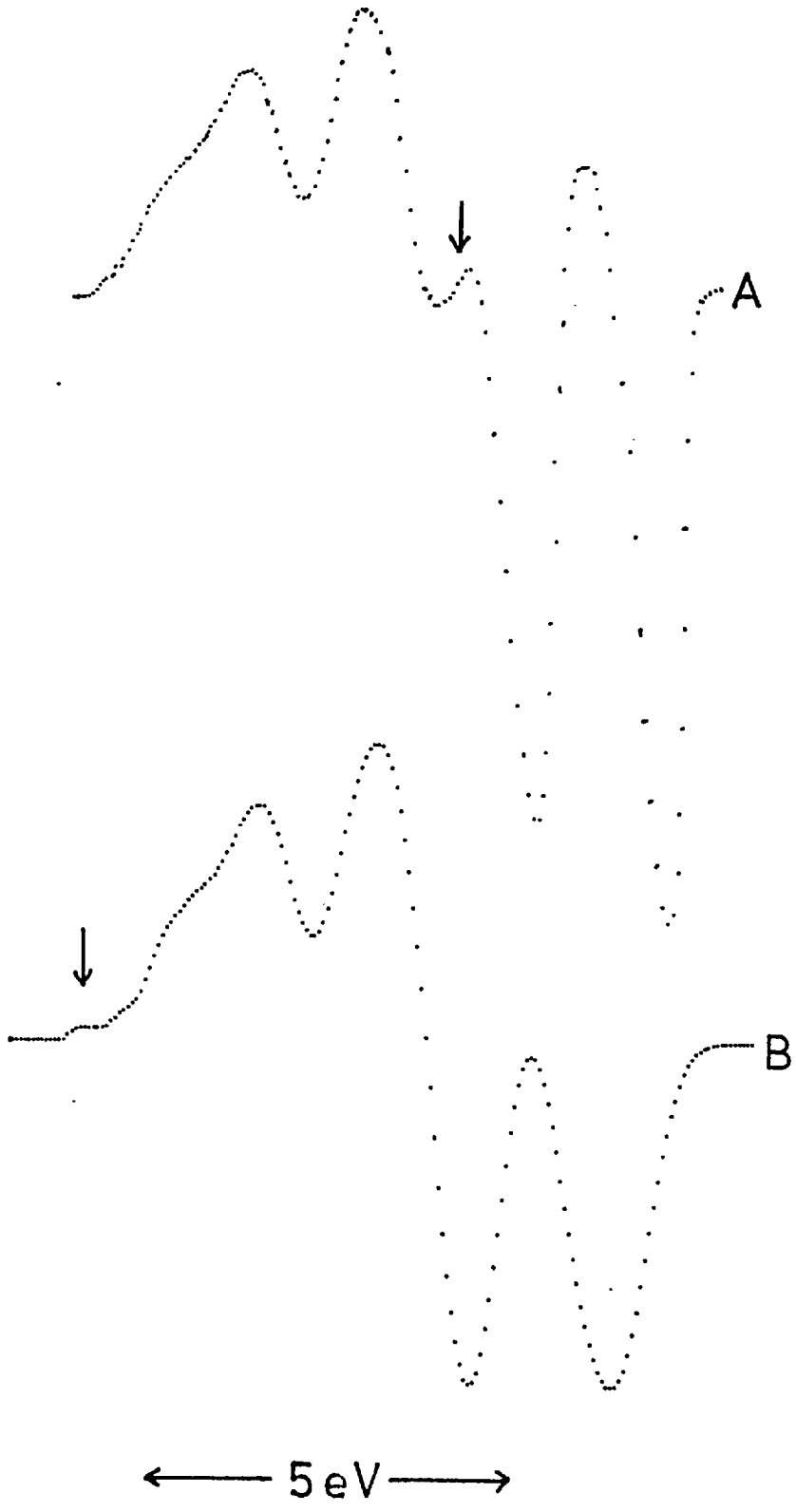

5d

since the predicted splittings are very close in either case and possible matrix elements effects suggest little emphasis could be placed on relative intensities in any event. In fact, we shall take B as the more representative since α then induces only a small feature (x) in the density of states function and gives overall the best fit to the observed spectrum. This choice is consistent with the previously less well resolved spectrum[90] where α was not apparent. (In that case choice of lower values of 'centre' did not lead to a convergent solution over a long period of time).

5.8 Summary

The problem of deconvolution has been discussed, pointing out the requirement for approximation to obtain a physically reasonable result. An iterative routine was devised which has been demonstrated to work well. A criterion for rapid convergence was found which has been correlated with an ambiguity in the interpretation of complex spectra.

CHAPTER 6

APS OF LAYER MATERIALS: I. TRANSITION METAL DICHALCOGENIDES

The transition metal dichalcogenides exhibit, as a group, a wide range of properties including a number of the more fascinating effects to be found in solid state physics. Considerable effort has been exerted during recent years toward gaining an understanding of their behaviour in terms of energy band schemes. Probably of greatest interest have been those compounds formed between the metals of groups IVA, VA and VIA (excluding chromium whose compounds are not layered) with the chalcogens sulphur, selenium and tellurium.

Electrically such compounds as ZrS_2 and HfS_2 are semiconducting with relatively wide band gaps ($\sim$ 2 eV); in MoS_2 the band gap is narrower. TiS_2 and $TiSe_2$ are metallic as are the group V compounds such as $NbSe_2$ and TaS_2 which become superconducting at low temperatures. The structural anisotropy is reflected in the physical properties; thus electrical conductivity is generally much greater parallel to the layers than perpendicular.

The layered structure is also of great practical importance since the crystals can be readily cleaved to thicknesses of a few hundred Angstroms for electron microscopy or optical transmission studies. Thicknesses down to 12 Å (or a single unit cell) have apparently been achieved enabling changes in the superconducting transition temperature to be followed as a function of crystal thickness[92]. Of relevance to the present work is the fact that such cleavage properties enable clean optically flat surfaces

to be prepared in vacuum for surface studies.

These compounds can also be intercalated i.e. molecules or atoms of other species introduced between the layers. Organic molecules such a pyridine, cyclopropylamine or octadecylamine have been intercalated into these compounds resulting in interlayer separations of over 50 Å; the superconducting transition temperature for TaS_2 has been shown to increase markedly when intercalated[93]. Transition temperatures as high as 13°K have been observed for non-stoichiometric titanium disulphide intercalated with lithium[94].

Alkali metals such as sodium and potassium can also be introduced between the layers when complex superstructures have been found in electron diffraction studies by Clark and Williams[95]. Such effects are also observed in the non-intercalated TaS_2 and have recently been interpreted by Scruby, Williams and Parry[96] as arising from a charge density wave coupled to a periodic lattice distortion.

The above gives only an indication of some of the areas of interest in these materials; a comprehensive review has been given by Wilson and Yoffe[12] and more recently by Yoffe[97]. Below ideas on their band structures particularly those aspects relevant to APS are developed. Good AP spectrum have been obtained for TiS_2, $TiSe_2$, VSe_2, ZrS_2, $ZrSe_2$ and MoS_2. In all cases, except ZrS_2 as mentioned in the text, these crystals cleaved to give mirror like surfaces. No tellurides have been studied owing to the non-availability of suitable crystals. The 5d transition metal compounds were not studied due to the insensitivity of APS to the 5d series. However, with the advent of X-ray filters, it may be possible for such materials as TaS_2 to be investigated in future since the M_5 levels, which are the most useful, are deep enough to make an X-ray filter valuable.

The crystals used where small platelets of paper thickness

and several millimetres across grown by vapour transport in the establishments listed in the acknowledgements. Exceptionally for these materials MoS_2 occurs naturally and such crystals were used in this work.

6.1 Crystal Structure

The general formula may be written MX_2 where M is the transition metal and X the chalcogen. Each layer consists of a hexagonal two dimensional array of M atoms sandwiched between two similar networks of X atoms. The co-ordination of each M atom by the X's may be either octahedral or trigonal prismatic and these two alternative structures are illustrated in figure 6a. In addition to this basic division the trigonal prismatic compounds adopt structures in which more than one layer is contained within the repeat unit, this not involving chalcogen atoms stacking immediately above one another. The notation 1T, 2H etc. is often used to refer to the structure; here the number gives the number of layers within a single repeat unit and the letter indicates the crystal symmetry: T - Trigonal, H - Hexagonal. Most of the crystals studied are 1T (octahedral co-ordination). MoS_2 like $NbSe_2$ is 2H (trigonal prismatic). The structure of MoS_2, which is identical to $MoSe_2$, differs from $NbSe_2$, however, in that the M atoms of one layer are located vertically above X atoms of an adjacent layer. In $NbSe_2$ M atoms stack above M atoms; figure 6b illustrates the types of stackings among the compounds studied. Figure 6c shows electron diffraction patterns for several materials studied (including graphite and boron nitride). These were obtained from crystals cleaved from samples after running AP spectra and in all cases show clear hexagonal diffraction patterns with some characteristic[98] 'streaking' for TiS_2. Structural

MX_2 structures

plan of single layer:

co-ordination unit:

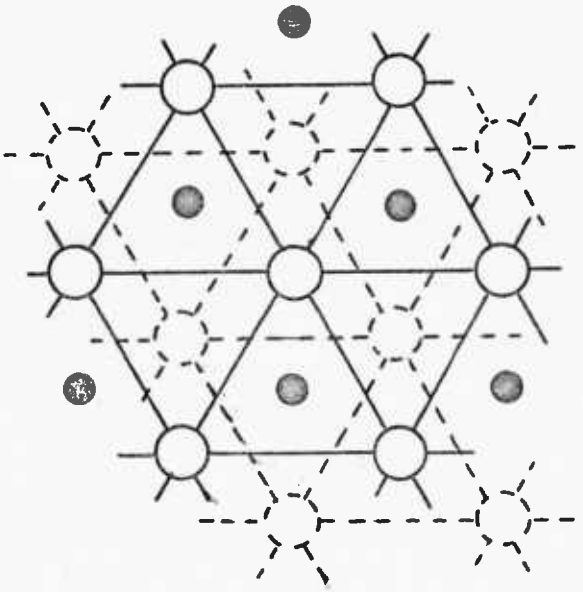

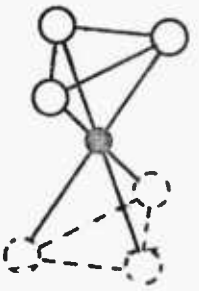

1T

● metal atom

○,◌ chalcogen atom

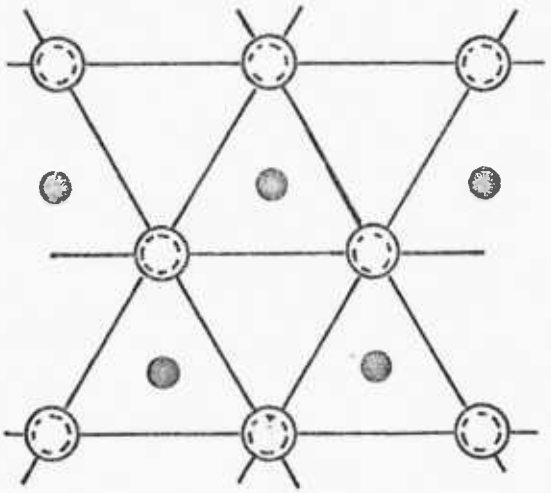

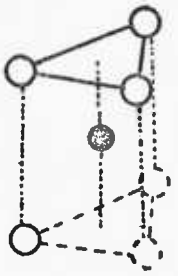

2H

6a

Stacking of layers in:

TiS_2 NbS_2 MoS_2

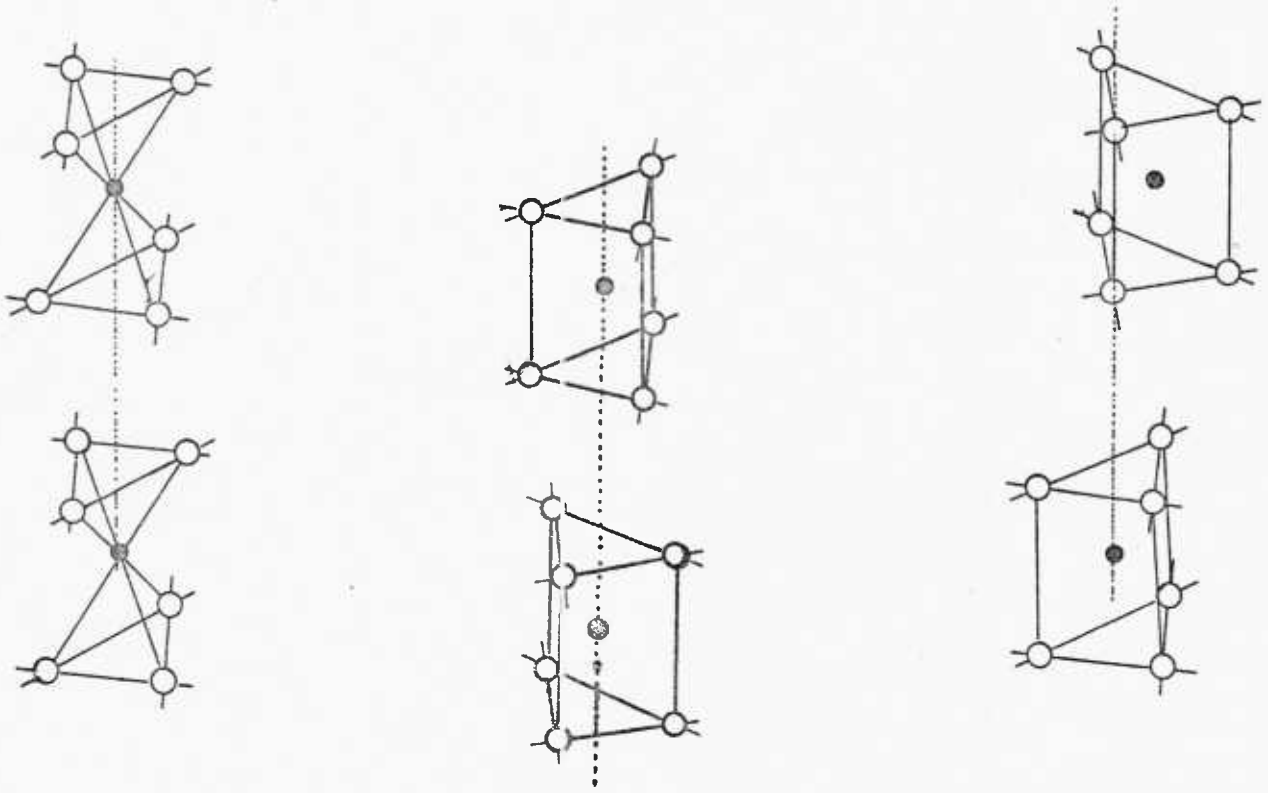

6b

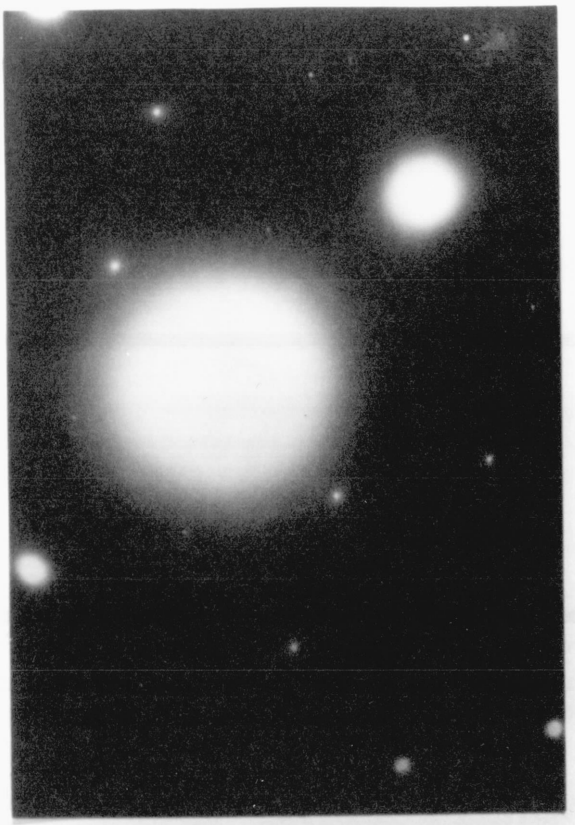

a TiS_2

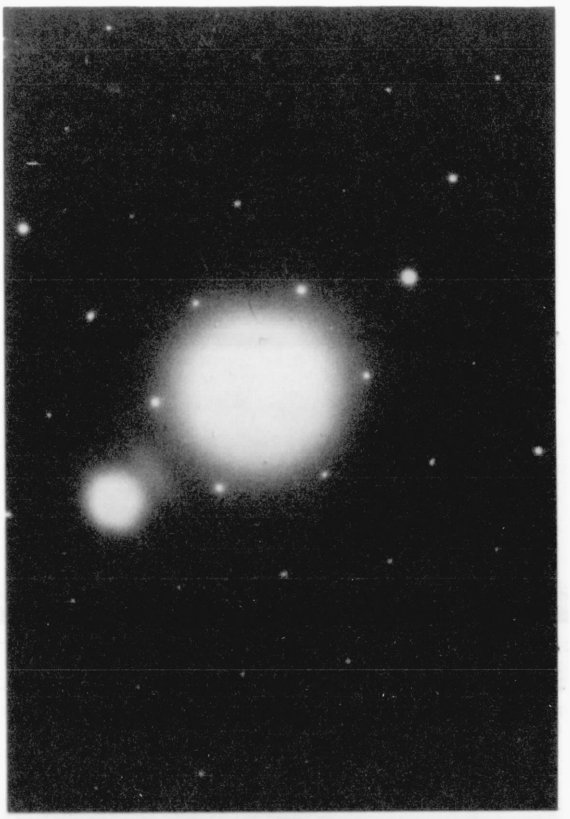

b Graphite

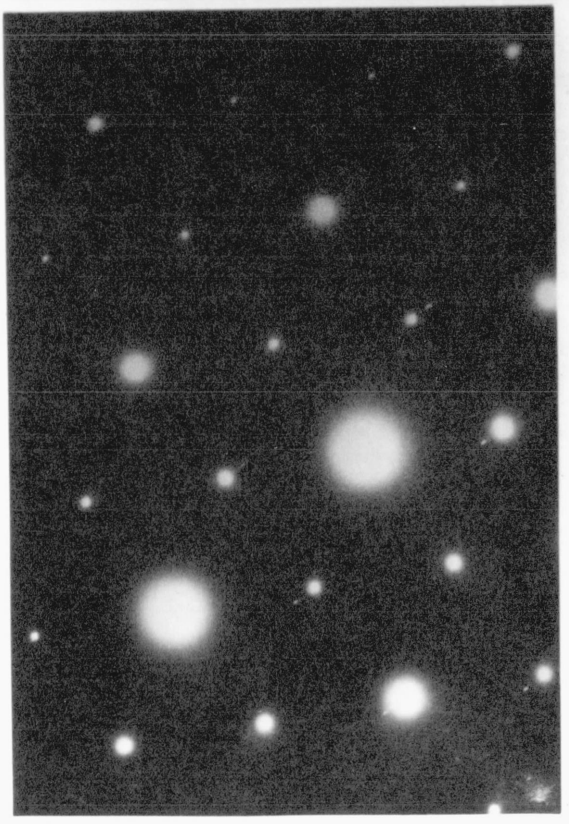

c $ZrSe_2$

d BN

parameters for compounds studied are tabulated in figure 6d.

6.2 Crystal Field Splitting of 'd' Orbitals

As seen above each metal atom is co-ordinated by six chalcogen atoms forming either an octahedron or trigonal prism. In this environment the energy of the metal d orbitals is lower for those which tend to concentrate electrons away from the negatively charged chalcogens, and this leads to an energetic splitting of d orbitals characteristic of the octahedral or trigonal prismatic co-ordination.

It is possible to deduce the subsets into which the d orbitals divide by appealing to symmetry. A proper consideration would involve us in the rather sophisticated language of group theory which is not attempted. We can, however, apply a simple symmetry argument to the case of a regular octahedron.

First we write down the angular dependence of the five d functions in cartesian co-ordinates:

$$d_{z^2} \sim 2z^2 - x^2 - y^2$$

$$d_{x^2-y^2} \sim x^2 - y^2$$

$$d_{xy},\ d_{yz},\ d_{zx} \sim xy,\ yz,\ zx$$

(These are the 'real' functions obtained by taking suitable combinations of the spherical harmonic functions).

Pictorially these can be represented in the familiar way shown in figure 6e. We now imagine these to be at the centre of a regular octahedron as illustrated for xy in figure 6f where the co-ordinate axes are chosen to pass through the ligand ions at the corners. It is readily seen that the environment of d_{xy}, d_{yz}, d_{zx} orbitals is identical and the octahedral environment cannot

Structural Parameters

	a (Å)	c/a	Co-ordination
TiS_2	3.405	1.670	Oct.
$TiSe_2$	3.535	1.698	Oct.
$V Se_2$	3.35	1.82	Oct.
MoS_2	3.160	1.945	Trig.
ZrS_2	3.662	1.590	Oct.
$ZrSe_2$	3.770	1.628	Oct.

Figure 6d

angular variation of d functions

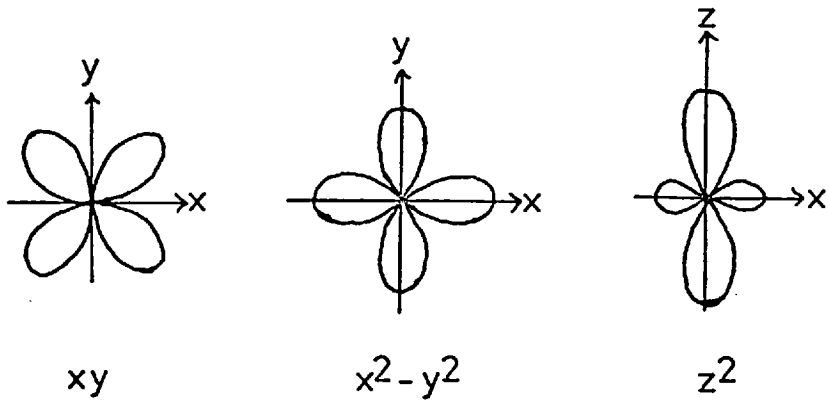

6e

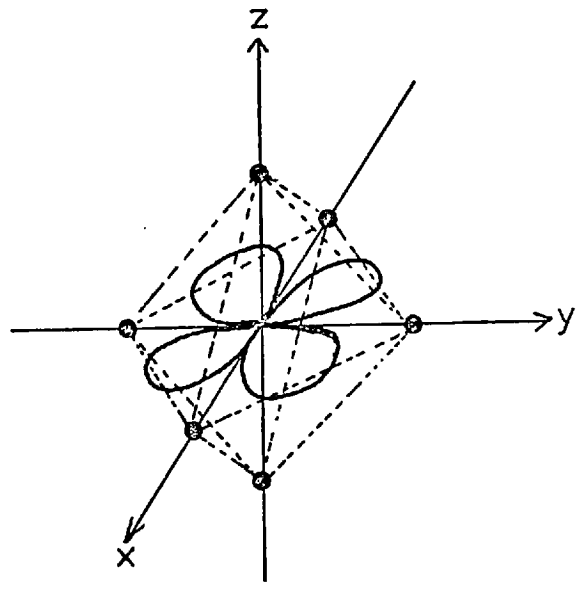

6f

alter the degeneracy of these three. That the other two are also degenerate is not so obvious from reference to figure 6e. However, while these are the conventionally chosen d orbitals other choices analogous to x^2-y^2 are possible i.e. z^2-x^2 or z^2-y^2. These three clearly are degenerate but they are not linearly independent and the normally quoted d_{z^2} is a linear combination of the last two and hence is indeed degenerate with $d_{x^2-y^2}$.

Symmetry then shows that in this case the d orbitals are split into two subsets of 3 and 2 which are referred to in group theory nomenclature as t_{2g} and e_g respectively. Unfortunately the choice of axes found convenient above is not appropriate for the layer materials where the z axis is normally best taken perpendicular to the layer. For this choice of co-ordinates the t_{2g} subset comprises the d_{z^2}, $d_{x^2-y^2}$ and d_{xy} orbitals.

These symmetry-based considerations do not, of course, determine the sign or magnitude of the relative splitting. One approach to this consists basically of obtaining an expression for the octahedral field, V_{oct}, assuming the ligand ions behave as point charges, and calculating the effect of this field on the energy of the wave functions. Such a calculation, described by Figgis[99], is extremely tedious, and similarly predicts the 3 and 2 splitting. However, we can easily see that the t_{2g} subset has the lower energy for the octahedral case since the lobes of d_{xy} in figure 6f point between the ligand ions while the $d_{x^2-y^2}$ point directly at the ligands.

Trigonal prismatic co-ordination does not lend itself to the same straightforward analysis as does the octahedral case and we simply quote the results here. It differs from the octahedral case in that the d_{z^2} orbital is no longer degenerate with the

$d_{x^2-y^2}$ and d_{xy} orbitals[100]. The ordering is generally believed to be that the d_{z^2} orbital has the lower energy. The same behaviour occurs for a non-ideal octahedron i.e. the subsets are 2, 2, 1, the last being d_{z^2}. Mattheiss's[100] calculations for 1T and 2H TaS_2 are reproduced in figure 6g since these neatly summarise the conclusions.

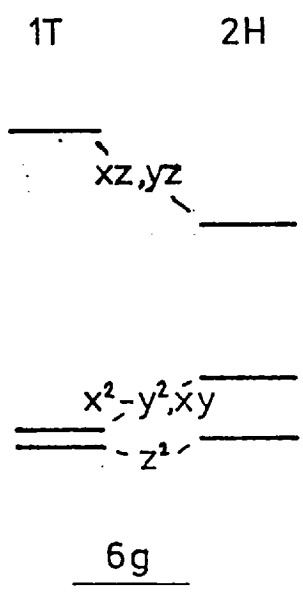

6g

The splitting between the d_{z^2} and d_{xy}, $d_{x^2-y^2}$ is much smaller for the octahedral case where it is only induced by the slightly lower symmetry cf. the regular octahedron case (edges are 3.37 and 3.51 Å).

6.3 Band Models

In, for example, the group IV dichalcogenides the neutral atom outer electron configurations are for M, d^2s^2 and for X, p^4. Accordingly in the formation of an ionic compound all of the M's outer electrons go to complete the X p levels leaving the metal atoms in a M^{4+} charge state with completely empty d and s levels.

The basic picture of the band structure of their solid compounds is therefore that the upper most valence bands are based on the chalcogen p states and the lowest conduction bands are based

on the metal d states, while the chalcogen s levels and metal s + p levels are respectively well below and above the Fermi level. If, as in general, the bonding is partially covalent the valence and conduction bands will be of 'mixed' p/d character, though this is not an important consideration for present purposes and it is convenient to refer to them as 'p' and 'd' bands.

Most calculations predict that the p and d bands do not overlap so that the group IV compounds are expected to be semiconductors. This is the case for e.g. ZrS_2 and HfS_2 but photoemission results[27] for TiS_2 and $TiSe_2$ reveal a small but finite density of states at the Fermi level, and in TiS_2 a tiny d band is clearly resolved immediately below the Fermi level. It was suggested that this may result from non-stoichiometric crystals where excess metal atoms donate electrons to the otherwise unoccupied d band or alternatively may be taken to indicate some degree of overlap between p and d bands. The reproduceability of this peak which was again observed during the present studies (see figure 6q) would tend to favour the latter explanation.

The d bands, in accord with the crystal field effect discussed above, are split into two subsets, the lower of which comprises three bands and the upper two (the group IV compounds are octahedrally co-ordinated). This division within the d bands is seen for example in the energy band calculations of Myron and Freeman[101] for TiS_2 and $TiSe_2$ shown in figure 6h. The density of states calculated from these energy bands is shown in figure 6i and shows the expected doubly peaked density of states.

In moving to groups V and VI the previously unpopulated d states now have to accommodate 1 and 2 electrons per M atom respectively, and the grouping of the d bands becomes important

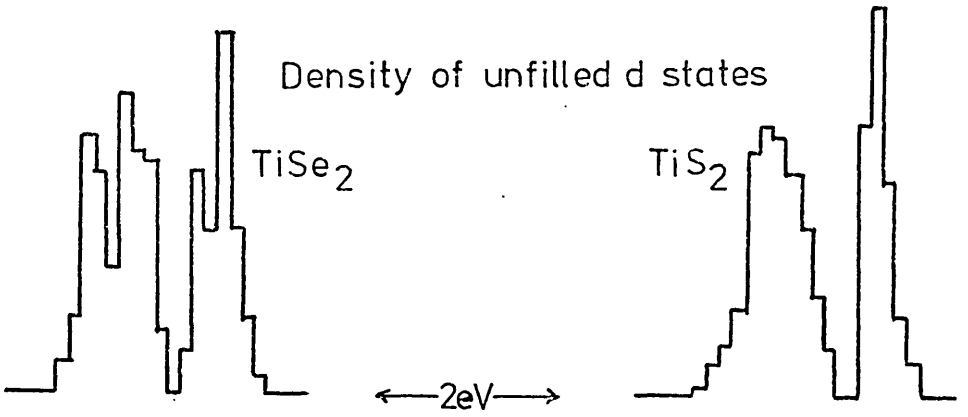

6i

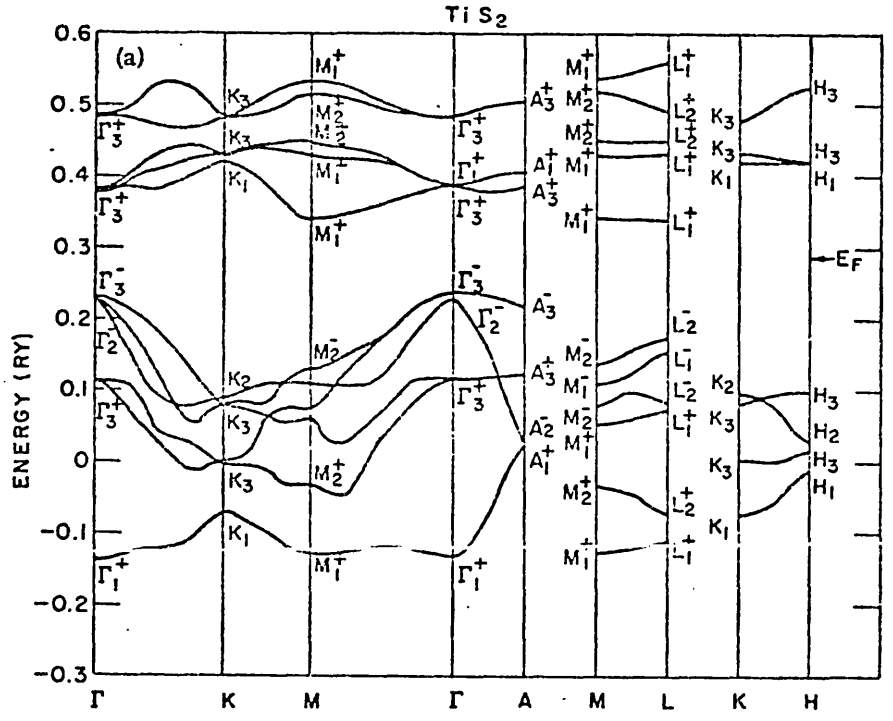

Brillouin zone

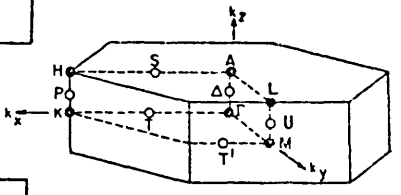

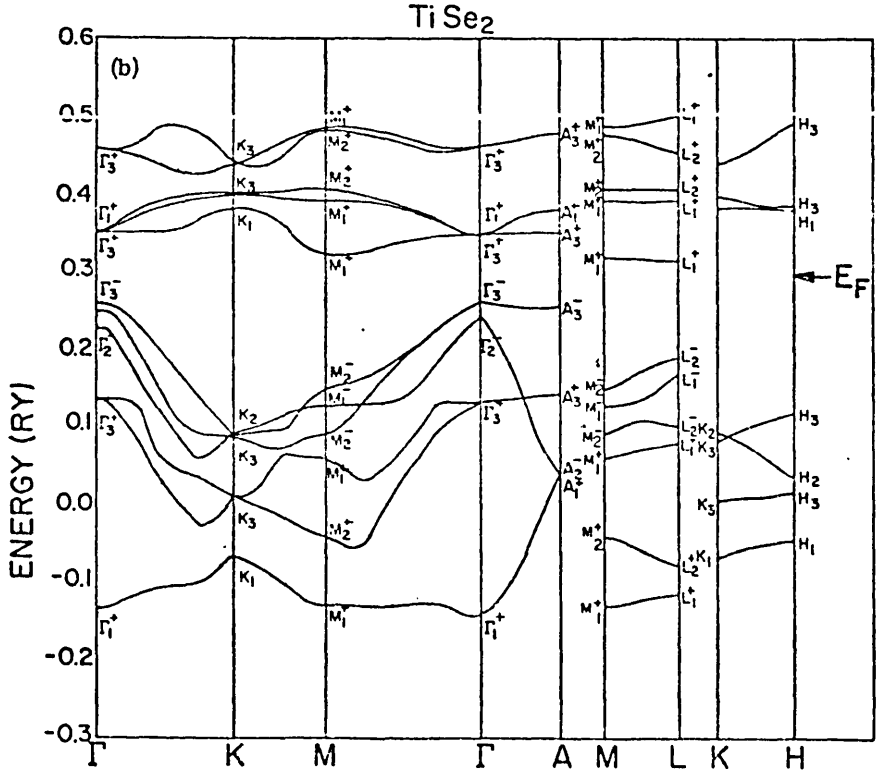

6h

(Myron & Freeman)

in determining the electrical behaviour. The group V compounds are generally metallic as expected, but in the group VI compounds, where trigonal prismatic co-ordination is adopted, the d_{z^2} band which is lower than the others is just filled leading to semi-conducting behaviour in e.g. MoS_2.

While the basic ideas outlined above are generally agreed upon the details remain in doubt. Thus for MoS_2 several models have been suggested to describe the ways in which the d and p bands overlap in order to fit to various experimental data. Three such models are shown in figure 6j (after Williams and Shepherd[102]). The splitting within the d_{xy}, $d_{x^2-y^2}$ level is due

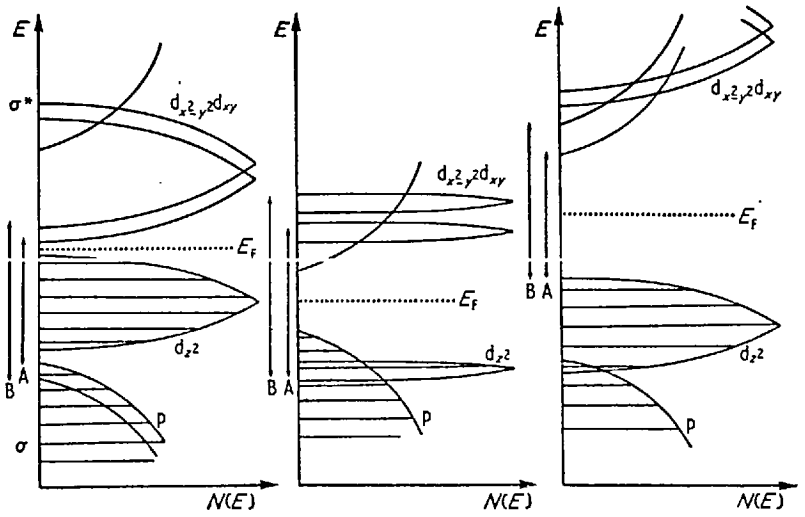

6j

(Williams & Shepherd)

to the spin-orbit interaction. (In fact further refinements to the third model are likely to be necessary[103]).

6.4 APS of TiS_2 and $TiSe_2$

The Appearance Potential Spectra of the Ti $L_{3,2}$ levels in TiS_2 and $TiSe_2$ are shown in figure 6k. Additional data accumulated over just the L_3 peak in each case are also shown and the top trace is for metallic titanium obtained by Park and Houston[63]. (The

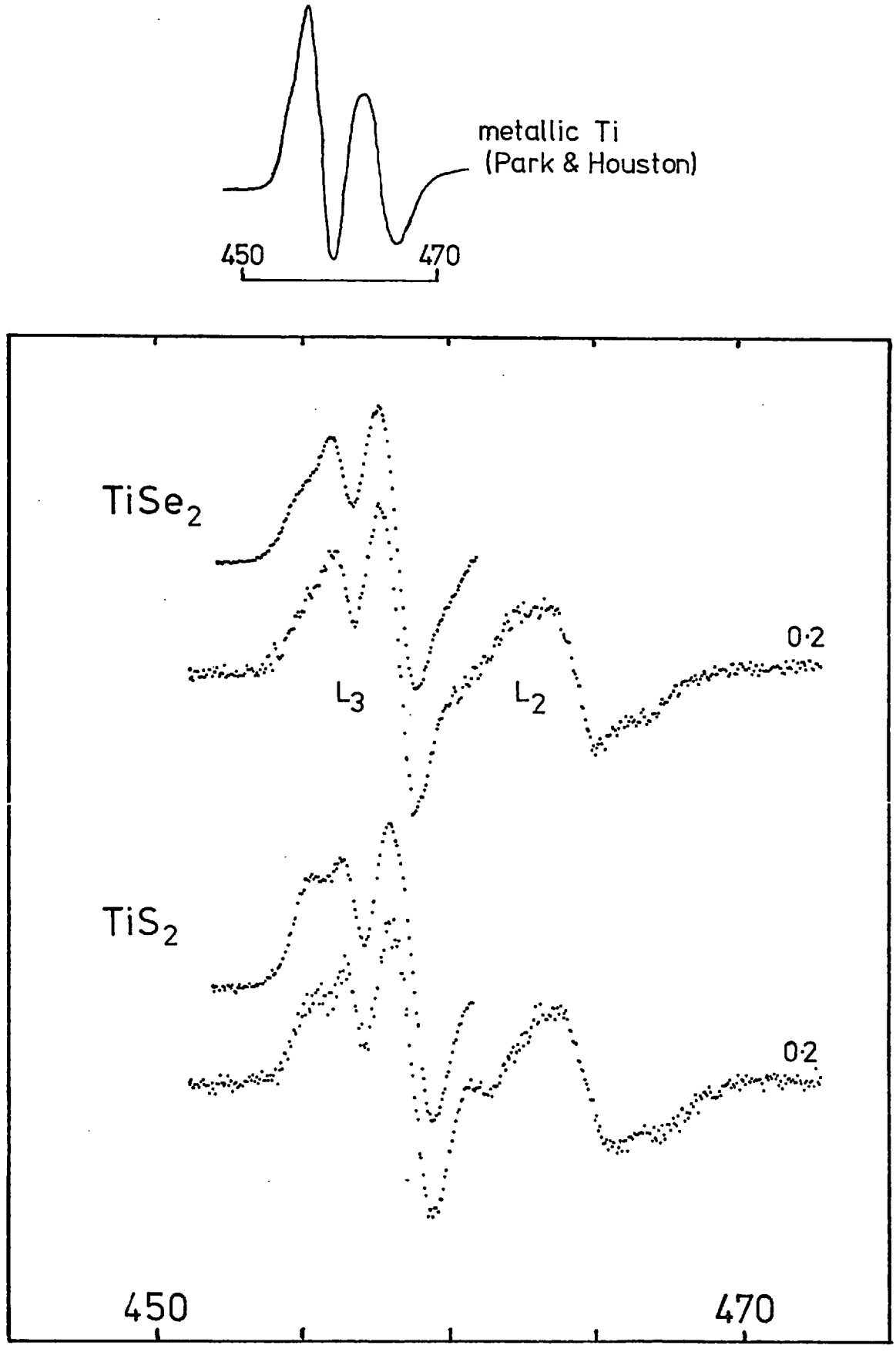
metallic Ti
(Park & Houston)
450
470
TiSe2
0·2
L3
L2
TiS2
0·2
450
470
→ binding energy (eV)

6k

shoulder is actually better resolved in the more recent data of Andersson and Nyberg[69]). For the compounds there is a pronounced splitting of the L_3 peak not seen for the metal and it seems almost certain that the origin of this is in the crystal field split d band discussed above. The TiS_2 and $TiSe_2$ spectra are very similar differing only in relatively minor detail, but such differences were highly reporduceable upon separate UHV cleaves.

In order to eliminate from consideration any possible initial state effects XPS spectra were also obtained for TiS_2 and $TiSe_2$ and the derivatives of these are compared with APS spectra in figure 61. (For convenience these AP spectra are the previously obtained less well resolved ones[90]). The XPS spectra show no sign of such splitting, and indicate within the limits of the experiment that in each compound all the Ti atoms are in an identical environment. A relative shift to lower binding energy (~ 0.4 eV) is seen in both APS and XPS in $TiSe_2$ and may reflect a smaller degree of ionicity in the selenide as might be expected.

Returning to the AP spectra of figure 6k we note that the L_3 and L_2 threshold shapes are quite different. In fact, this is by no means unexpected since the close spacing of these levels implies a significant overlap in their APS; and it is really only the positive region of the L_3 threshold and to a lesser extent the negative dip of the L_2 which can be regarded as known unambiguously. However, in view of the marked splitting observed for the L_3 peak it would be surprising if such considerations alone were responsible for there being only a faint splitting observable in the L_2. The failure to resolve such a feature in the latter is probably a consequence of a relative broadening of the L_2 level due to Coster-Kronig transitions. It was found by experiment that the splitting

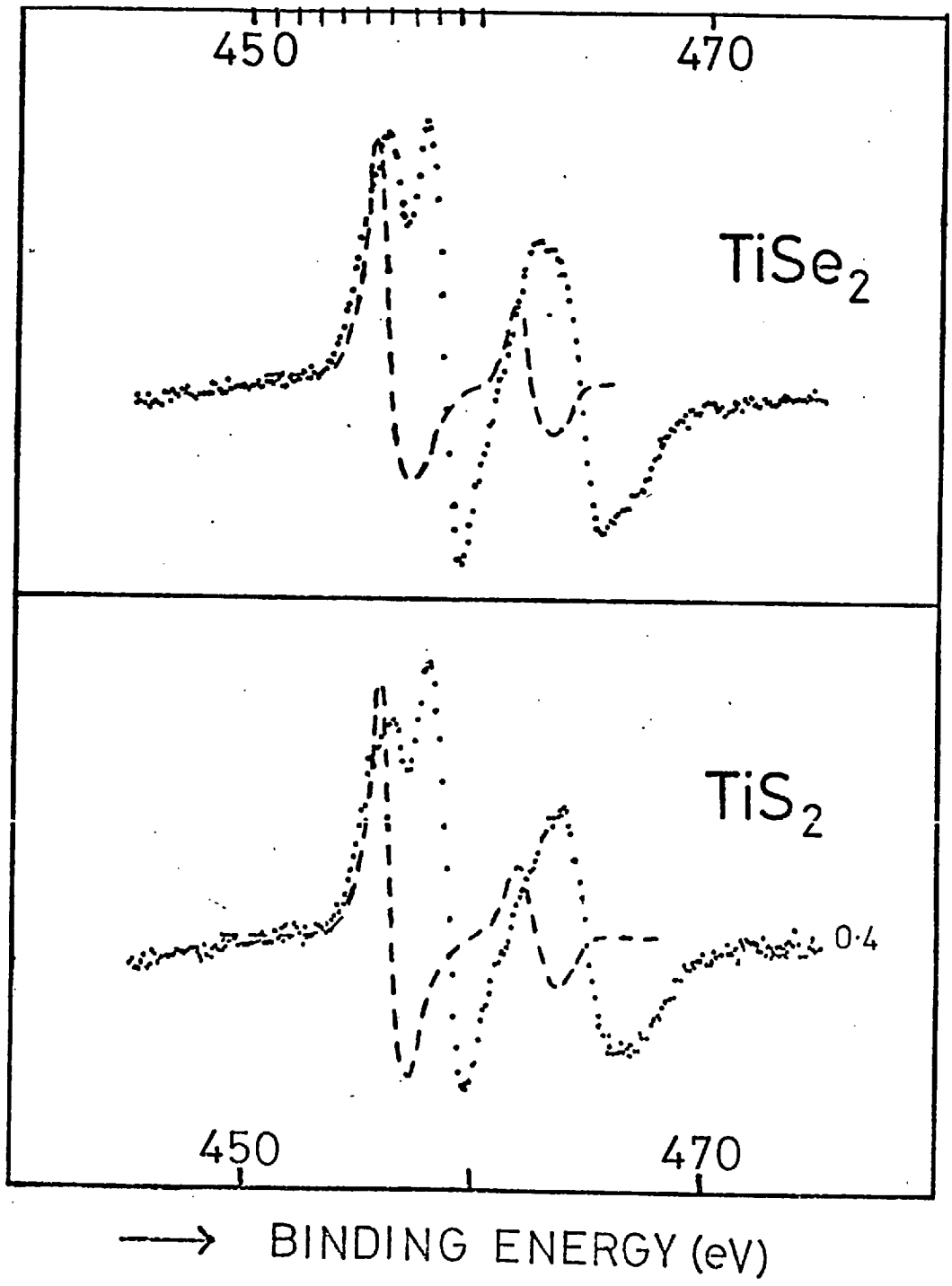
450
470
TiSe2
TiS2
0·4
450
470
BINDING ENERGY (eV)

is very sensitive to such broadening effects and this can be seen by referring to figure 6r where a modulation amplitude of 1 volt r.m.s. is sufficient to all but completely eliminate any sign of the splitting. At the same time the total broadening of the L_3 peak is almost too small to be measured ($\lesssim$ 5%). (The data of figure 6k used a modulation amplitude of 0.2 volts r.m.s. though 0.4 volts gives close to the same resolution). The XP spectra did show a small broadening of the L_2 relative to the L_3.

6.4.1 Implications of a Self-Convolution Model

In the presence of a predominantly doubly peaked density of states function the self-convolution model predicts that three peaks should be seen in the AP spectrum and this is illustrated in figure 6m. In the present case the entanglement of the L_3 and L_2 thresholds prevents an absolute identification of the third peak. However in both cases the negative dip of the L_2 threshold exhibits a distinct inflexion which is in accord with the near washed-out structure for this level. In addition a marked shoulder is seen on the low energy side of the 'L_2 peak' in TiS_2 and less clearly in $TiSe_2$ which seems most likely to have its origin as the third peak of the L_3 threshold. Thus it is seen that the main features of these spectra fit rather well with the qualitative predictions of the crystal field and self-convolution models.

In addition to the points mentioned above a subsidiary splitting is found for the first peak of the sulphide while a marked shoulder is visible for the selenide. It is tempting to associate these effects with the splitting between the d_{z^2} and d_{xy}, $d_{x^2-y^2}$ levels in a non-ideal octahedral environment, but this is probably not directly applicable. As shown by Mattheiss[100]

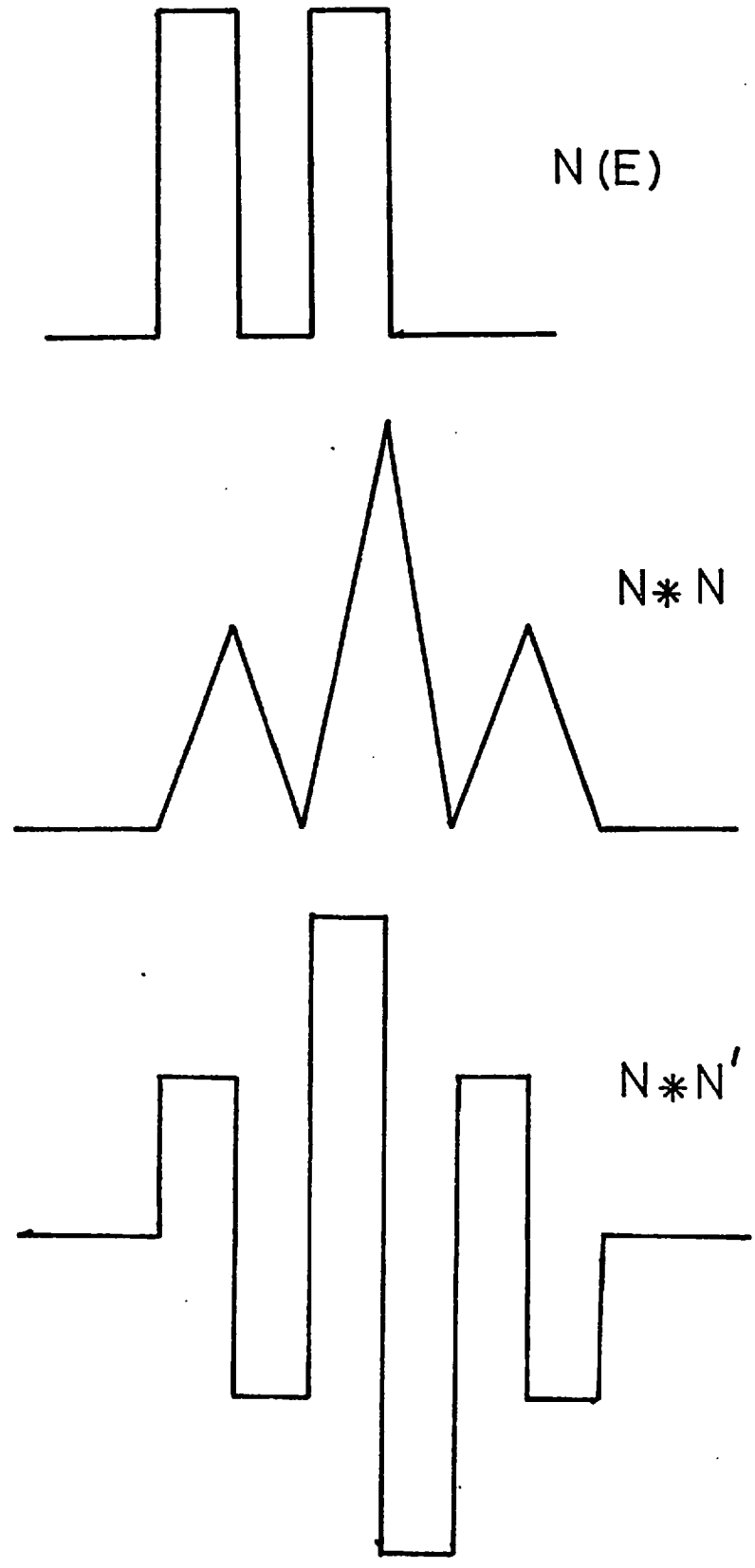

6m

for 1T TaS_2 the splitting between the centres of gravity of these sub-bands is rather small (0.1 - 0.2 eV) and not reflected in the total density of states in general. Myron and Freeman's[101] density of states histograms suggest such a splitting for $TiSe_2$ but not TiS_2. However, it may in any case be recalled that APS sees a localised density of states and the details may well differ from the details of the total density of states.

6.4.2 Deconvolution Results

The results of deconvoluting the positive parts of these L_3 spectra by the methods described in chapter 5 are shown in figure 6n (Solution B is assumed though for completeness figure 6o shows A for TiS_2. The spurious shoulder was less marked here and this solution would probably be reasonable, but B is taken for consistency. For both compounds either solution gives the same c.o.g. sub-band separation to within 0.1 eV). Core level and instrumental broadening effects are inherent and allowing for these the Fermi level is inserted about 1 eV from the onset (± 0.5 eV). The c.o.g. sub-band separations are 2.2 eV for TiS_2 and 1.9 eV for $TiSe_2$ (± 0.2 eV). These figures are very close to the previous values[90], but the present high resolution results indicate a larger crystal field effect in the sulphide which is consistent with both the slightly less marked splitting in the $TiSe_2$ spectrum and greater ionicity in the sulphide. For TiS_2 other experimental data are available; Fischer's[104] X-ray absorption also gives a value of 2.2 eV and Sountag and Brown's[105] synchrotron absorption gives 2.3 eV. All are in very close agreement. Figure 6n also shows Fischer's X-ray absorption band and Myron and Freeman's theoretical histograms. The latter give somewhat lower values of

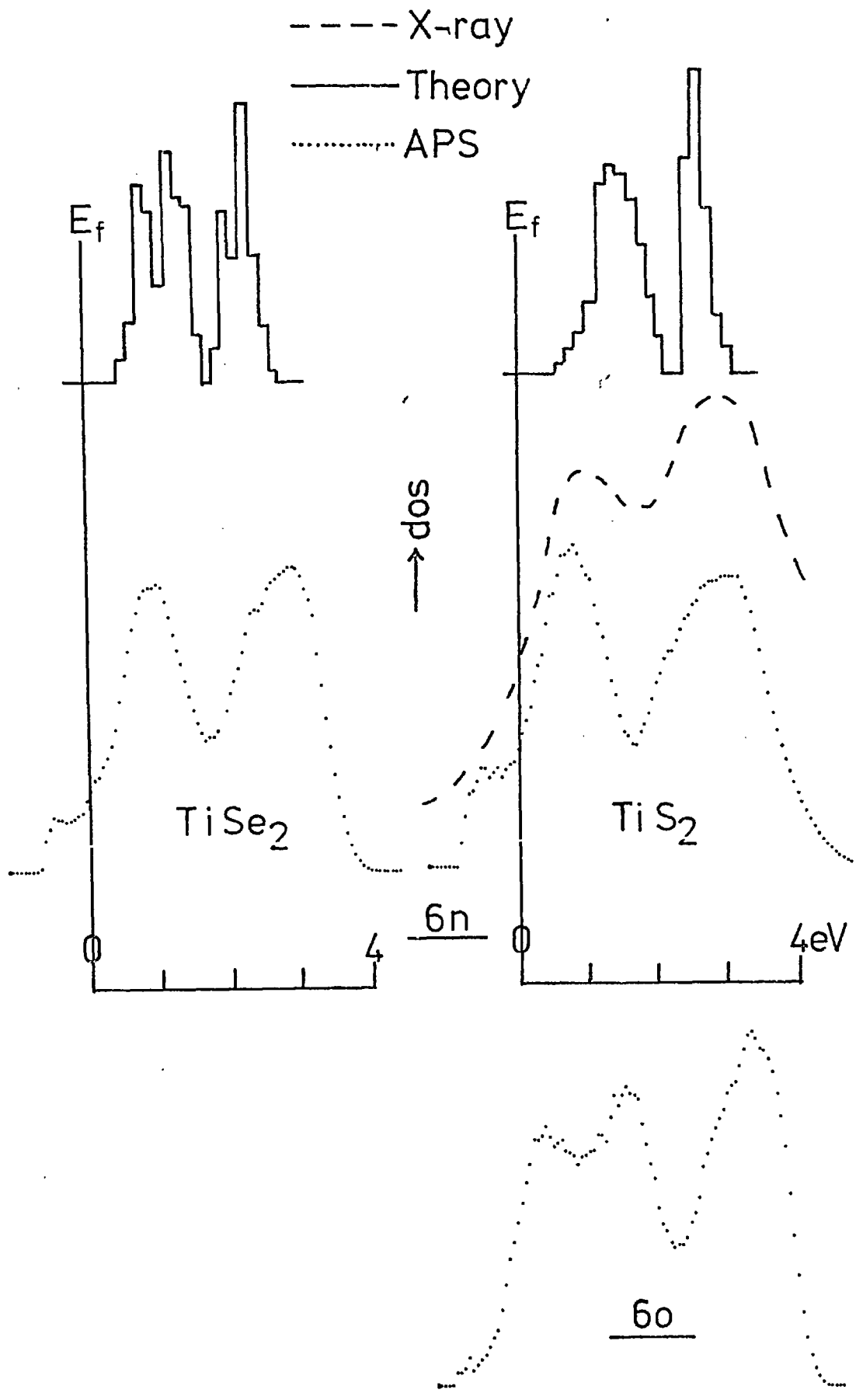
X-ray
Theory
APS
E_f
E_f
dos
$TiSe_2$
TiS_2
6n
6o
0
4
0
4eV

1.3 eV. It is interesting to note that the magnitude of this discrepancy is about the same as the predicted band gap which photoemission suggests does not exist; thus closer agreement between experiment and theory would ensue if the lower (t_{2g}) subset were moved down in energy by $\sim$ 1 eV.

A small step (x) is suggested at threshold. In a sense this is consistent with the observation that the density of states at the Fermi level is small in photoemission but not with the implication that p and d bands overlap. However, we cannot place emphasis on the details since as discussed in chapter 5 an accurate self-convolution is not obeyed. An alternative explanation which would fit this last observation is that the feature α is not a density of states effect and the role of x is to account for it in an 'unobtrusive' manner. Thus if x is manually deleted the differentiated self-convolute closely resembles the actual spectrum but without any trace of α as would be anticipated. It is conceivable though somewhat speculative that the origin of α could be a threshold singularity of type predicted by Laramore[10].

The calculated 'APS thresholds' from the density of states functions in figure 6n are shown in figure 6p and compared with the actual spectra. Apart from the initial spurious feature they are seen to be in close agreement over the positive part of the L_3 threshold (between the arrows) over which region matching was carried out. In general deviations may occur at higher energies since no account is taken of the possibility of scattering electrons to states above ε. Thus the sharp third peak, while not in precise agreement with the shoulders on the L_2 peaks, is close enough to make this interpretation very credible.

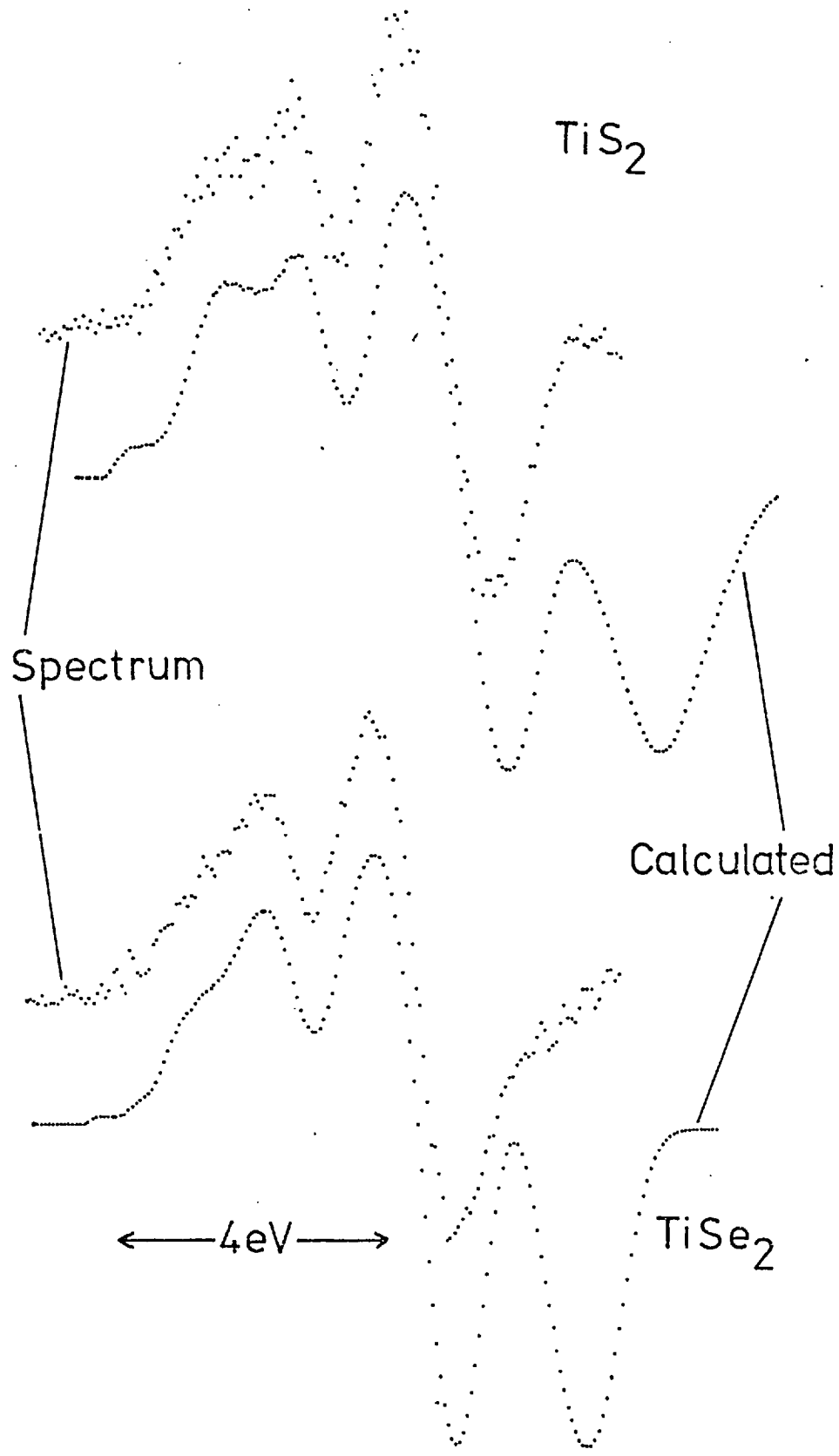

6p

6.4.3 UPS

UPS data were obtained from a TiS_2 crystal subsequent to running its APS. The He I (21.2 eV photon energy) and He II (40.8) spectra are reproduced in figure 6q. They are in good agreement with those of Shepherd and Williams[27], the tiny 'd' band at the Fermi edge is seen in the He II. Its absence in He I suggests the 'd' character[91].

6.4.4 Plasmon Losses

Weak structure is frequently seen in AP spectra of transition elements over a range of $\sim$ 50 eV and the $L_{3,2}$ spectra for TiS_2 and $TiSe_2$ extended to higher energies are shown in figure 6r; also shown is the L_1 level for TiS_2 as well as XPS $L_{3,2}$ data for TiS_2. Such structure in APS may originate from either features in the conduction band or represent loss replicas of the main peaks due to plasmon creation or interband transitions. It was previously shown[14] that there is some correlation between such structure and electron energy loss data for metallic Ti and Fe.

In the present cases a barely resolved doublet of the same spacing as the L_2/L_3 levels is seen displaced from the main peaks by some 22.0 eV in TiS_2 and 19.6 eV in $TiSe_2$. The XPS of TiS_2 is also shown revealing a similar doublet, and this latter observation would seem to establish these structures as loss peaks. Liang and Cundy[46] have made electron energy loss measurements on a number of transition metal dichalcogenides though not including TiS_2 and $TiSe_2$. They observe the main feature of the loss spectrum in each case to be the σ loss at energies $\sim$ 20 eV followed by a weaker peak at about twice the energy associated with 2 x σ losses and other weak features including the π loss. In figure 6r subsequent structures are observed at about 42.5 eV for both the

UPS of TiS_2

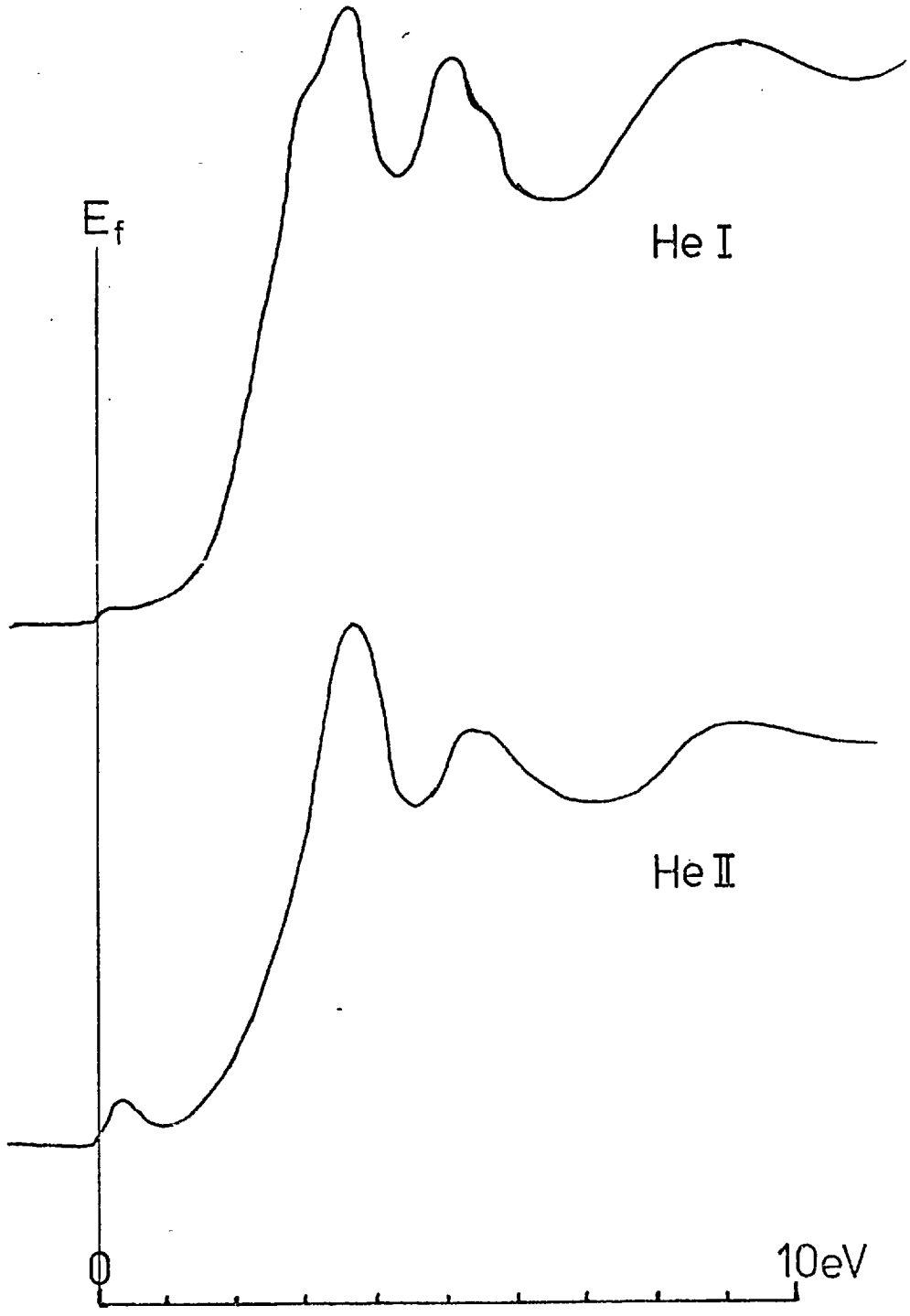

6q

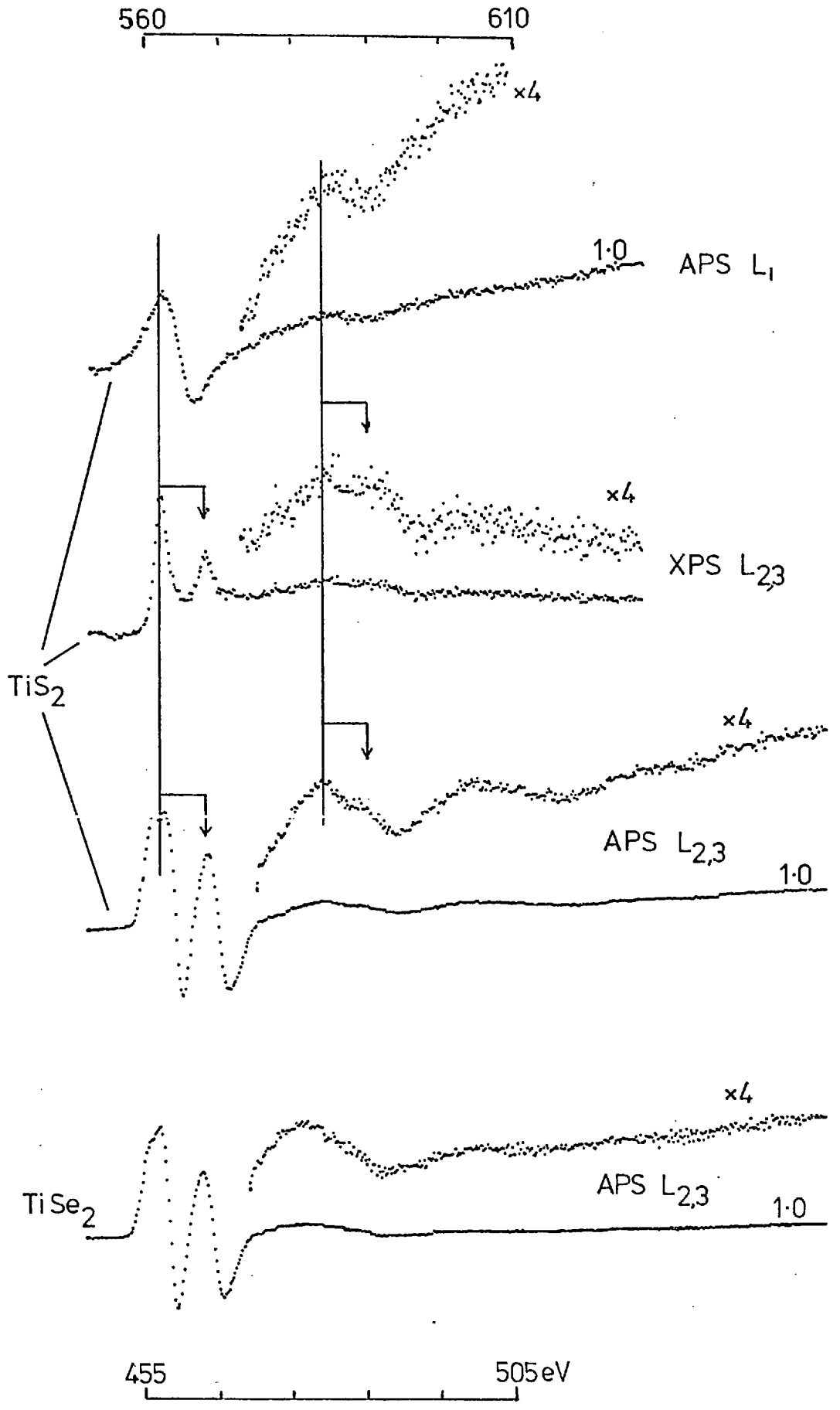
560
610
×4
1·0
APS L_1
×4
XPS $L_{2,3}$
TiS_2
×4
APS $L_{2,3}$
1·0
×4
$TiSe_2$
APS $L_{2,3}$
1·0
455
505 eV

6r

sulphide and selenide though so weakly in the latter case that its precise position is slightly uncertain. There is a hint of such structures in the XPS and also the APS L_1.

Several points are worth noting concerning these observations. Firstly the satellites observed in APS are much weaker than the main peaks (by perhaps an order of magnitude) and of comparable relative intensity to those seen in XPS. Plasmon lifetime broadening effects are in evidence since the doublet $L_{2,3}$ structure is only just apparent. There are no obvious features which can be assigned as π losses though this is not surprising if they are much weaker as in the energy loss measurements, particularly since they would in any case be overlapped by the main part of the threshold.

A further point concerns the intensities of the second satellites since that in the sulphide does not decrease in intensity to the extent that would have been expected in contrast to the $TiSe_2$ spectrum. There is no obvious explanation for this; it may be that other processes (interband transitions or high energy conduction band structure) are influencing the spectrum. That they seem to occur at the same energy in both cases (as opposed to 2 x the first peak energy) would support this, but the present data are inadequate to clarify this.

Finally we note that the values observed here for the σ losses (19.6 eV for $TiSe_2$ and 22.0 eV for TiS_2) show a similar trend between sulphide and selenide as was found by Liang and Cundy and indeed predicted in the free electron approximation. It thus originates from selenium's larger atomic size and accordingly larger lattice parameters in the selenides.

6.5 APS of VSe_2

Most of the above ideas apply in this case also and we need only consider the points of difference. VSe_2 is again octahedrally co-ordinated but with an additional d electron cf. the titanium compounds so that the t_{2g} sub-band is partially populated and VSe_2 accordingly metallic. The unfilled density of states, however, would be expected to be very similar to TiS_2 and $TiSe_2$ though no band structure calculations have been found in this case. The V $L_{2,3}$ AP spectrum for VSe_2 is shown in figure 6s (top trace); the poorer signal to noise ratio is a consequence of the apparently greater reactivity exhibited by this material and rapid deterioration of the spectrum. Thus useful data was obtained only for about ten minutes in this case cf. about an hour for TiS_2 and $TiSe_2$. Again the L_3 peak is split though not the L_2; it is noticeable that the high energy edge of the L_3 peak does not fall as rapidly as for the Ti compounds and a faint shoulder-like structure is evident. This can be consistently attributed to the third peak here since the observed splitting is smaller.

The deconvolution results are also shown in figure 6s where the lower trace represents the implied density of states function and above the 'APS threshold' calculated from this is compared with the actual spectrum. As suggested, the narrow splitting leads to the third peak not being resolved in good agreement with observation. The shoulder-like structure here cannot be confused with that found in deconvolving the Ti spectra since there is no sharp third peak in this case. The separation of the sub-bands is about 1.6 eV in accord with the estimate made on the basis of the previous APS data[90].

APS of VSe_2

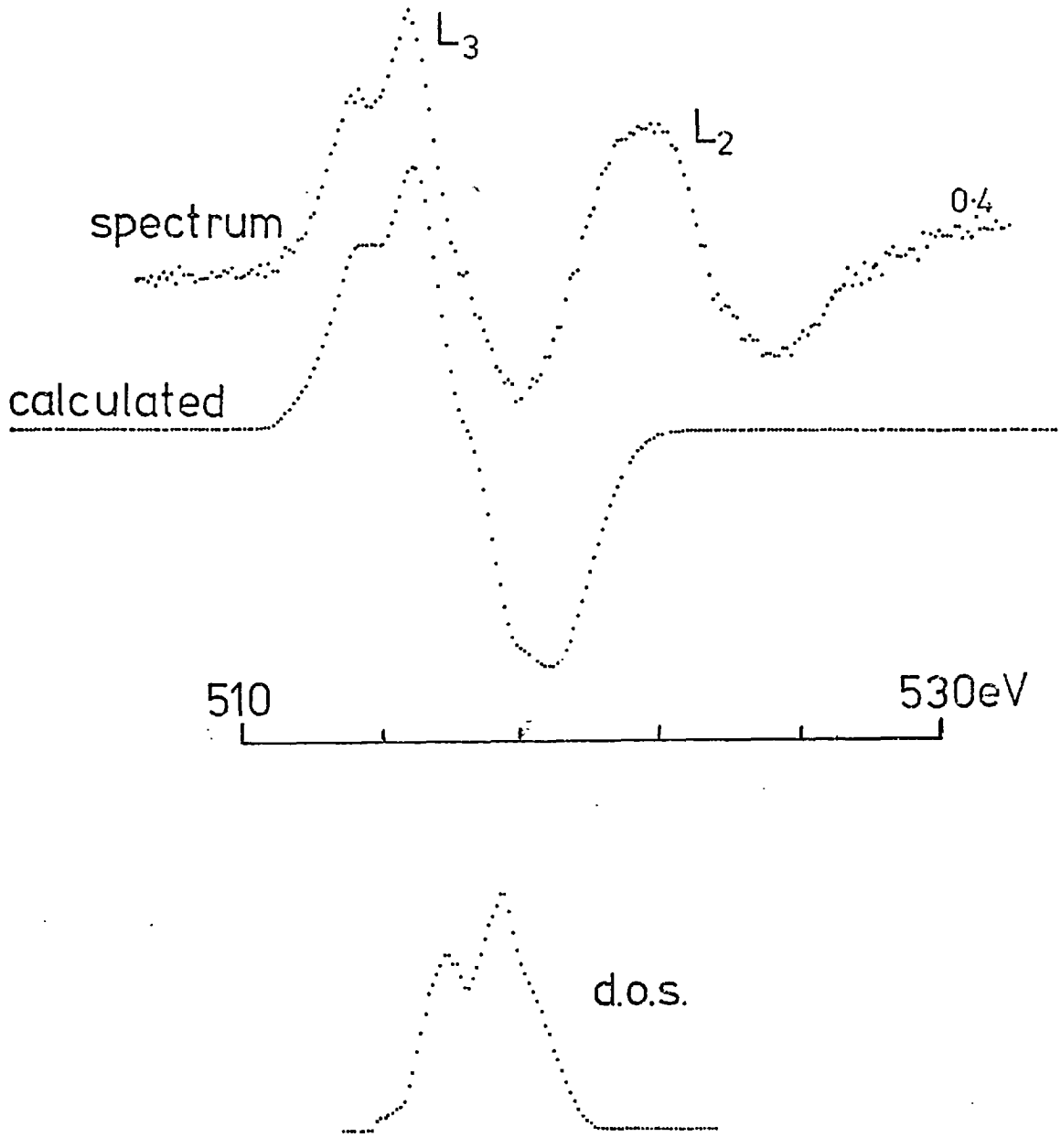

6.6 APS of MoS_2

MoS_2 is trigonal prismatically co-ordinated and the crystal field model suggests we may expect the d bands to form three subsets based on

(i) d_{z^2} (ii) d_{xy}, $d_{x^2-y^2}$ (iii) $d_{xz}d_{yz}$ orbitals. The Wilson and Yoffe[12] band model suggests that the d_{z^2} band is split off lower than the others leading, because it is completely filled in the group VI compounds, to semiconducting behaviour. Mattheiss's[100] (APW) band structure is shown in figure 6t and (referring to the right hand portion of the diagram) we see that one d band is split off significantly lower than the others producing an indirect gap of about 1.1 eV within the d manifold. Mattheiss describes this as a 'hybridisation gap' not directly related to the ligand field splitting; however, we continue to refer to the lower band as the 'd_{z^2} band' for convenience.

The upper four bands do not fall into two separate groups but the calculated unfilled density of states is doubly peaked with a separation of about 1 eV as also shown in figure 6t. The AP spectrum for the $M_{4,5}$ Mo levels in MoS_2 is shown in figure 6u, where it can be seen that the M_5 peak is faintly split, the magnitude being

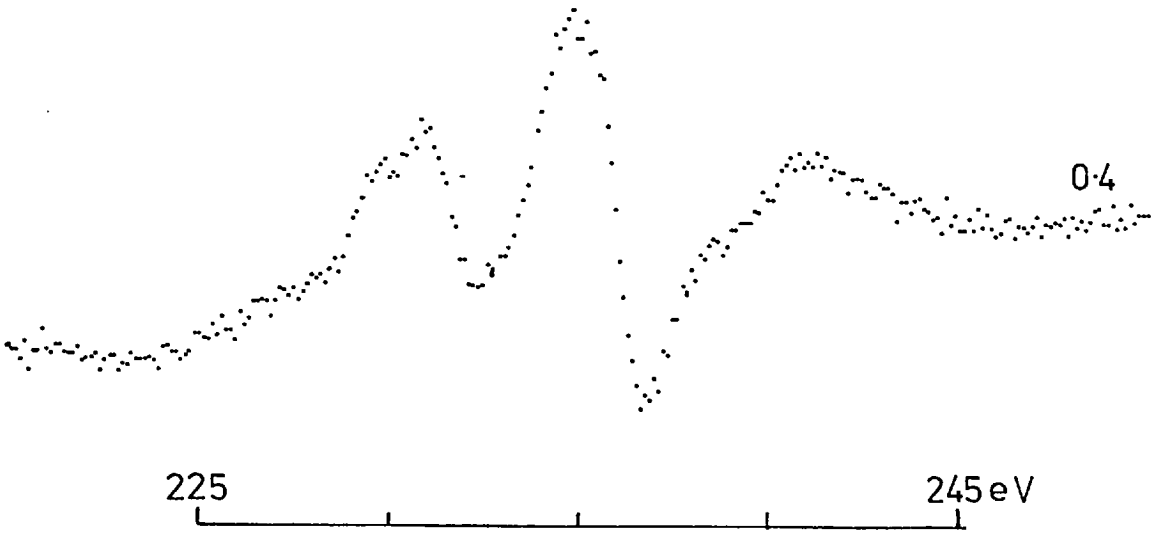

6u

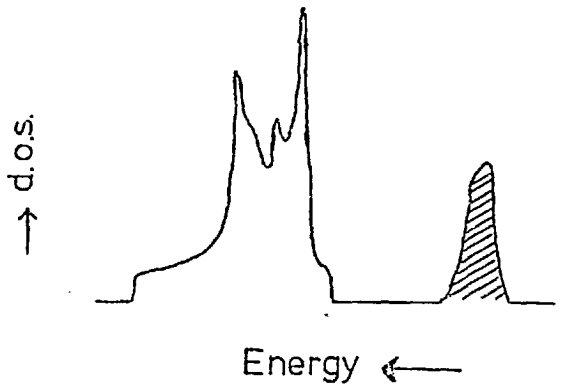

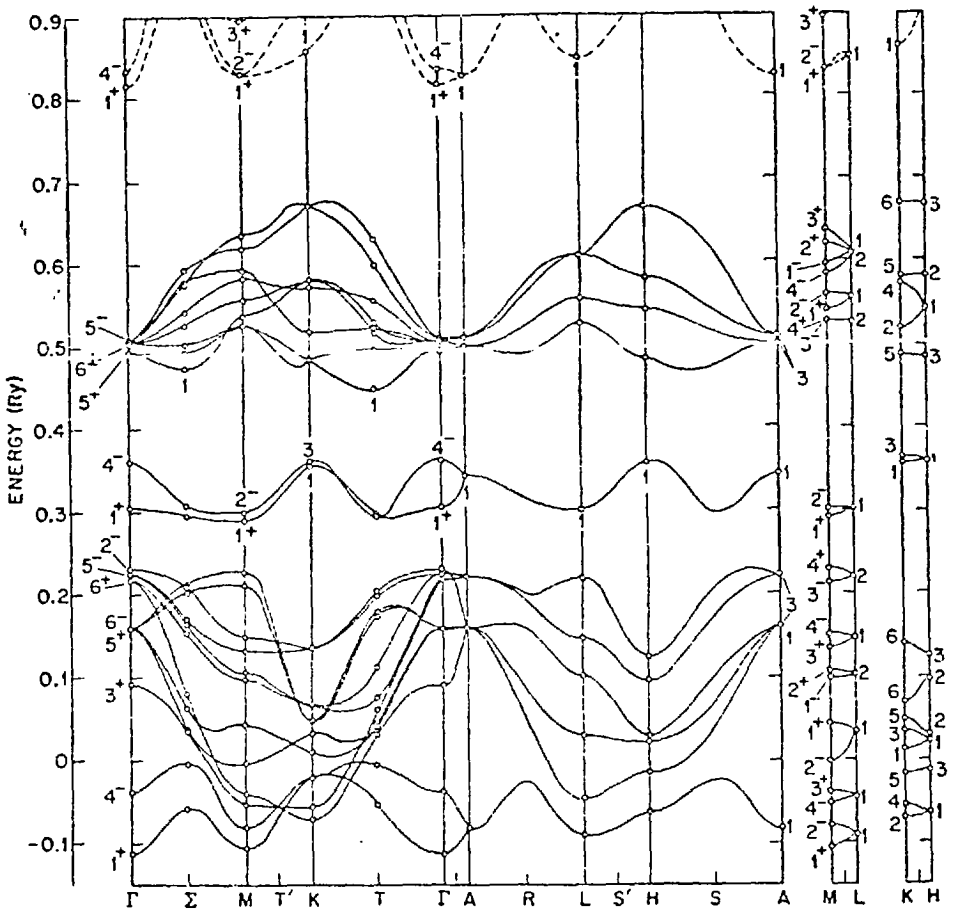

Energy bands in 2H MoS_2

6t (Mattheiss)

about 1.2 eV. We previously[90] observed that deconvolution tends to widen the separation in the density of states function which leads to a value of about 1.5 (± 0.3) eV. Sountag and Brown's[105] synchrotron absorption data suggests a figure more like 2 eV and contrasts sharply with the TiS_2 case where APS and synchrotron absorption were in agreement. However, their experiment used excitation of the sulphur $L_{2,3}$ levels and the spectrum was subsequently separated into two components assuming a 1:2 weighting and known spin orbit splitting. In fact this separation was relatively unambiguous for TiS_2 but not for MoS_2 so that their value may be less reliable in the latter case. It is also possible that the disagreement may reflect differing local densities of states around Mo and S atoms.

6.6.1 Higher Energy Structure

In accord with previous data for TiS_2 etc. the M_4 peak is not split. There is, however, a loss-like feature some 6 eV from the M_4 peak (10.7 eV from the M_5) but neither of these values agrees with π loss observed at 8.9 eV by Liang and Cundy[46]. (The σ loss lies beyond the range of these measurements, it being more difficult to get good spectra from 4d transition elements). In fact, it is relatively safe to associate this 'loss' with the M_4 level since if it were associated with the M_5 a second stronger feature should also be found contrary to observation. It is noted that the intensity ratio of the M_4/M_5 peaks is anomalous here as in the case of Mo metal. Such an occurrence is not uncommon in APS and has been discussed by Park and Houston[50,63] in connection with the 3d series. They explained it as due to a 'j-dependent selection rule' for the radiative decay rate.

The 'loss' feature of the MoS_2 spectrum then would seem

likely to originate from structure in the conduction band at an energy some 7-8 eV above the Fermi level. This would accord with the band model for MoS_2 proposed by Leveque et al.[106] on the basis of optical and photoemission data. The low energy edge is also in rough agreement with the lowest lying metal s bands in Mattheiss's calculation.

If the above interpretation is correct, it is relevant to enquire why similar observations were not made for other materials such as TiS_2. In fact such structure at similar energy in TiS_2 would tend to be masked, because the peaks and subsequent negative dips are appreciably broader in TiS_2 than MoS_2. There are of course, inflexions in the negative L_2 dips in the Ti spectra which were associated with the 'third peak'. This interpretation remains the most consistent, since the relative intensities of the supposed third peaks for L_3/L_2 levels is in accord with the degree of splitting observed.

The narrower peak found in MoS_2 is in accord with the partially filled d band in this material and the wider splitting in octahedral materials; the overall width of the M_4 peak in MoS_2 ($\sim$ 3 eV) is in excellent agreement with the extent of the upper four d bands in Mattheiss's calculation. The latter also shows a much greater separation between d and s bands in MoS_2 than in his other results, there being overlap in the only 1T calculation (TaS_2), and this separation would tend to favour the observation of s states.

6.6.2 Low Energy Structure

A low energy tail is observed associated with the M_5 peak and a possible source of this is an experimental effect in that MoS_2 being semiconducting may charge under the electron

beam. It is interesting to speculate, however, on the possible source due to impurities[103]. The photoemission threshold behaviour[91] in MoS_2 was parallel to that in niobium doped $MoSe_2$ and Shepherd[91] suggests that Ef may be 'pinned' within Nb d-states which though not observed in UPS could possibly be responsible for this effect in APS.

The above assignments are, however, at best tentative and a more systematic study of the compounds of groups V and VI would be interesting. Unfortunately, during the present studies an $MoSe_2$ spectrum was only obtained after a 'poor' cleave and simply resembled the MoS_2 one but less well resolved, while no useful signal was obtained for $NbSe_2$.

6.7 APS of ZrS_2 and $ZrSe_2$

These gave particularly complex spectra for the Zr $M_{4,5}$ levels as shown in figure 6v; in contrast with all of the other results presented so far a basic doublet structure is not obvious. Instead essentially four peaks are resolved mutually spaced at intervals of approximately 3 eV.

6.7.1 Experimental Notes

The ZrS_2 spectrum was obtained first and, being semiconducting, it was thought likely that charging effects may have been responsible for the complexity of the observed spectrum, a possibility supported by the presence of a step on the surface. In order to eliminate any such occurrence the $ZrSe_2$ crystal used was actually conducting presumably due to a slight excess of Zr. Although the extent of such an excess is not known, provided it were less than say 10% it would be unlikely to appreciable modify the

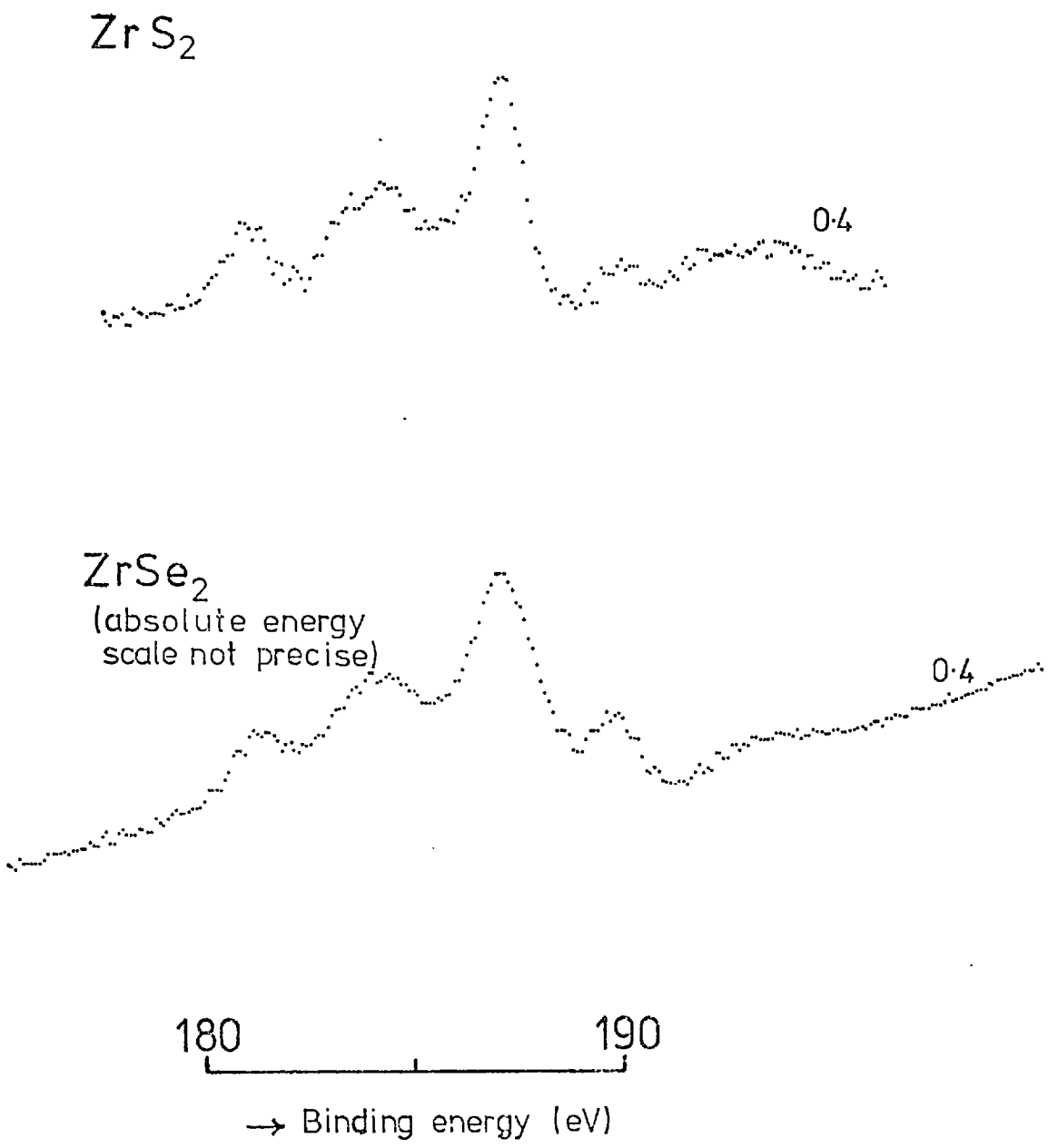
ZrS_2
0·4
$ZrSe_2$
(absolute energy
scale not precise)
0·4
180
190
→ Binding energy (eV)

6v

APS. The similarity between ZrS_2 and $ZrSe_2$ spectra strongly suggests, as assumed below, that both are truly representative. An attempt to obtain XPS data for the $ZrSe_2$ crystal was unsuccessful since it was apparently too thin after the APS run to cleave well again.

6.7.2 The Proposed Model

These compounds are closely related to the Ti ones, Zr also being a group IV metal and ZrS_2 and $ZrSe_2$ are likewise octahedrally co-ordinated. Estimates of the sub-band separations made from the band structure calculations of Murray, Bromley and Yoffe[107] give values of 2.5 eV for ZrS_2 and 2.0 eV for $ZrSe_2$. However recalling that calculations seem to underestimate such splittings in general, we refer to the analogous calculations for TiS_2 and $TiSe_2$ by Murray and Yoffe[109]. In both cases the t_{2g}/e_g splitting is around 1.7 eV, so that, upon scaling the zirconium figures using the mean for TiS_2 and $TiSe_2$ found here, we find values in the region of 3.0 for ZrS_2 and 2.4 for $ZrSe_2$. The M_4/M_5 separation in Zr found from XPS using a $ZrSe_2$ crystal is 2.5 eV.

The above implies that, unlike the Ti compounds, the M_4/M_5 separation is very close to the t_{2g}/e_g separation. In APS then we should in such circumstances see two sets of three peaks overlapping in such a manner as to produce four peaks altogether in good qualitative agreement with observation. The mutual peak spacings in APS are 2.9 - 3.0 eV which is probably a fairly close measure of the crystal field splitting in ZrS_2 and $ZrSe_2$. That the peaks are better resolved in the sulphide is consistent with a larger crystal field effect than in the selenide, and indeed the separation of first to fourth peaks is smaller in the latter by some

0.2 - 0.3 eV, leading to a narrower t_{2g}/e_g spacing by about half this amount.

If it was difficult to disentangle the L_2 and L_3 contributions to the Ti spectra, the situation here is near-impossible, and clearly it is not possible to quantify matters much further. The effect of the slightly smaller M_4/M_5 relative to the t_{2g}/e_g separation will be to overlap slightly negative dips with peaks and generally complicate peak shapes which may be responsible e.g. for the faintly doublet structure of the second peak in ZrS_2.

We can, however, make some attempt to see how the intensities accord with the above model. If we assume that, as for Mo, the M_4 threshold is more intense that the M_5, and for well-separated similarly-weighted sub-bands the ideal peak intensity ratios go as 1:2:1, it is found that the two central peaks are the most intense with the third largest of all, as observed.

6.8 Summary

The main features of the AP spectra for the octahedral compounds have been explained by the crystal field split d band in conjunction with the self-convolution model. Deconvolution has enabled the t_{2g}/e_g splitting to be determined for TiS_2, $TiSe_2$, VSe_2. In addition the calculated doubly peaked density of unfilled states in MoS_2 was detected and a σ loss peaks identified for TiS_2 and $TiSe_2$.

CHAPTER 7

APS OF LAYER MATERIALS: II GRAPHITE AND BORON NITRIDE

These two materials are closely related structurally and are also isoelectronic. Of primary interest is graphite whose complex SXAPS has been observed previously[16,17]. The multi-peaked structure was thought to originate from multiple plasmon loss events. The results obtained here, however, show much better resolution than was previously achieved, and, as is to be shown below, are better described by the same sort of conduction band argument that was used for the transition metal dichalcogenides. XPS and SXAPS studies of boron nitride provide further support for this interpretation.

7.1 Crystal Structure

The structure of graphite and boron nitride is illustrated in figure 7a. A single layer comprises a hexagonal network with B and N atoms alternating in boron nitride; all atomic sites are, of course, equivalent (in the single layer) in graphite. The common forms of the(hexagonal)materials have alternate layers identical (ABAB...), but there is a slight difference between graphite and BN in the way the layers stack. Referring to figure 7a, the illustrated graphite structure (in plan) shows the two layer repeat, different symbols being used to denote C atoms in different layers. Only one BN layer is shown and here the two symbols differentiate between the two types of atom. The BN structure differs from graphite in that adjacent layers have all atomic sites vertically above one another differing only through the interchange of B and N atoms.

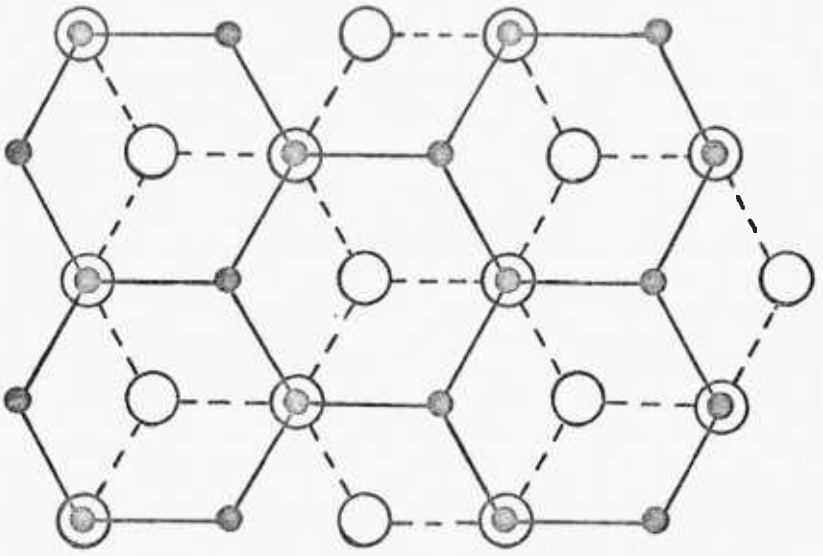

graphite

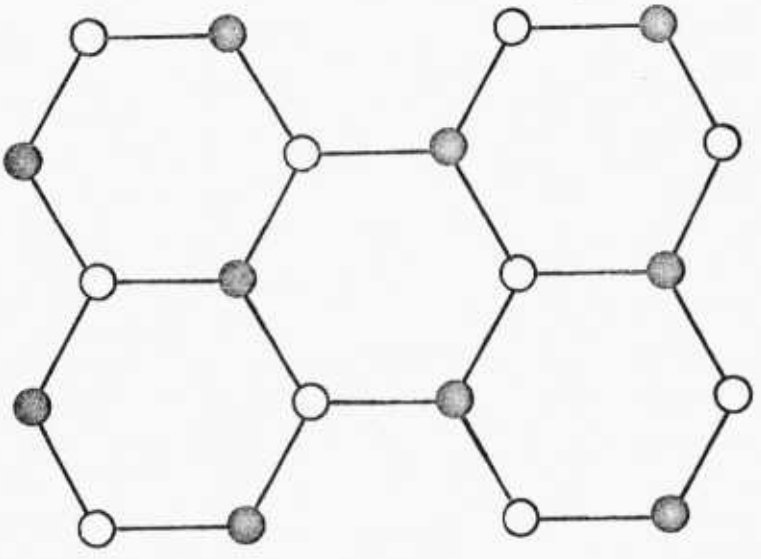

boron nitride

Graphite is extremely anisotropic; but one example of this is strikingly illustrated by the fact that, while its easy cleavage properties lead to its use in lubricants, the great strength of the intralayer bonds has led to the development of carbon fibres. The nearest neighbour separation within the layers is 1.42 Å compared with 3.35 Å for the separation of adjacent layers; for BN the analogous distances are almost identical at 1.45 and 3.30.

7.2 Band Structure - Theoretical Predictions

Because of the relatively wide separation of the layers, which are held together by weak van de Waals forces, a good approximation to the band structure of graphite is obtained by considering a single layer. In this 2-D approximation electron states can be classified according to whether they are even (σ) or odd (π) under reflection in the layer plane. The ground state of a carbon atom has the outer electron configuration $2s^2p^2$, so that the orbitals upon which calculations are based are 2s, $2p_x$, $2p_y$, $2p_z$. Of these only the last mentioned has π symmetry, and the first three can be combined to sp^2 hybrid orbitals which overlap strongly giving bonding and antibonding σ states well separated in energy. The p_z orbitals give much weaker overlap and would be expected to have energies intermediate between the σ bonding and antibonding states. Early attempts[109,110] at a band structure ignored the σ electrons and examined only the nature of the π bands among which the Fermi level lies, since there are two atoms in the unit cell and hence eight bands in all based on the above orbitals, with sufficient electrons to fill four of them. The ordering of the bands is three low lying σ bands, (based on the bonding orbitals) followed by the two π bands and three more σ bands at higher energies. It was found in the early calculations that the two π bands are degenerate at the

corners of the symmetrical 2-D Brillouin zone. Graphite is thus expected to be a semiconductor with zero energy gap i.e. a semi-metal.

For BN rather similar considerations apply, with the obvious distinction that now two atomic species are present. Neutral atom configurations would lead to the p_z orbitals being empty at B sites and doubly occupied at N sites. It is thus more likely that a degree of electron transfer occurs giving some ionic character to the bondings; and a further consequence[111] is that a finite minimum energy gap occurs between the π bands ($\sim$ 4 eV) so that despite its close relationship to graphite, BN is actually an insulator.

The 2-D calculation for graphite, using a variational approach, by Painter and Ellis[112] is reproduced in figure 7b. No band structure calculation has been found for BN though Zunger[113] has obtained various band parameters using a small cluster calculation.

For present purposes the extension to three dimensions has little effect except to replace each band by two closely spaced ones due to the doubling of the number of atoms in the unit cell. It is for this reason that we are probably justified in ignoring the structural differences noted in 7.1 and regarding BN and graphite as essentially isostructural.

7.3 Experimental Studies of the Band Structure of Graphite

We confine attention here mainly to the work of Willis and co-workers[114,115,24], reference being made also to the photo-emission studies of Shepherd and Williams[116] and optical reflectance data of Greenaway et al.[117].

Graphite – 2-D bands

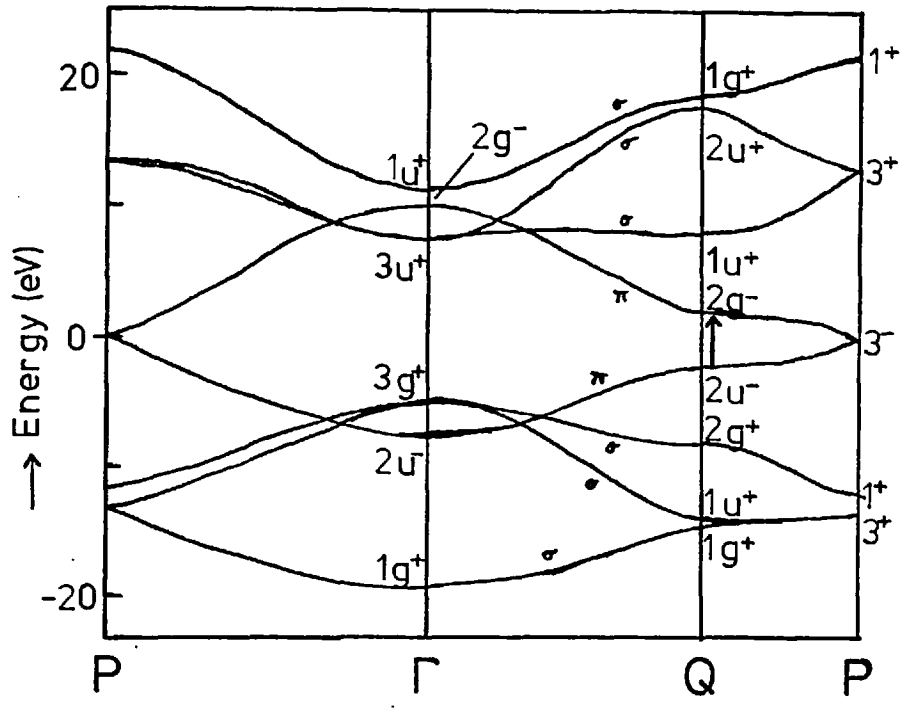

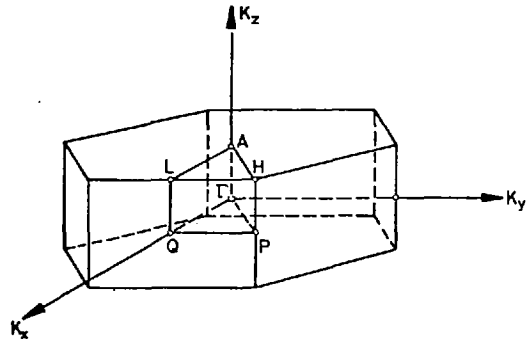

Three-dimensional Brillouin zone of graphite.

7b (Painter & Ellis)

7.3.1 Secondary Electron Emission (SEE)

Willis et al. have observed structure in secondary electron emission induced (mainly) by electron bombardment of graphite surfaces. They show[24] (after Kane[23]) that such structure is expected to reflect the conduction band density of states. Without considering their detailed analysis,however, it is readily seen that where a peak occurs in the density of states function at some energy above the vacuum level, then there is an increased probability that any excitation will result in the population of, and possible emission from, states at that energy. Superimposed on the cascade background we may see structure corresponding to features in the conduction band density of states, and, since the final energy distribution may result from multiple processes, observations should be independent of the initial probe.

In graphite an extremely sharp, intense peak is observed both in the electron and photon induced secondary distribution corresponding to an energy 7.5 - 7.7 eV above the Fermi level. (The photoemission data of Shepherd and Williams (see figure 7c) give the former value obtained by subtracting the observed energy cf. the Fermi level from the photon energy; the error should certainly be no more than ± 0.2 eV). A further weaker feature is observed some 1 eV higher.

These values are in fact extremely close to two minima in the lowest σ conduction band (see figure 7b) at the points Γ and Q of the Brillouin zone (7.5 and 8.0 eV respectively). From the flatness of the band in the ΓQ direction we would expect a large contribution to the density of states at this energy, and these peaks observed in SEE are in very satisfactory agreement with the Painter and Ellis scheme.

In addition Willis et al.[115] observed other weak structure

Graphite - UPS (He I)

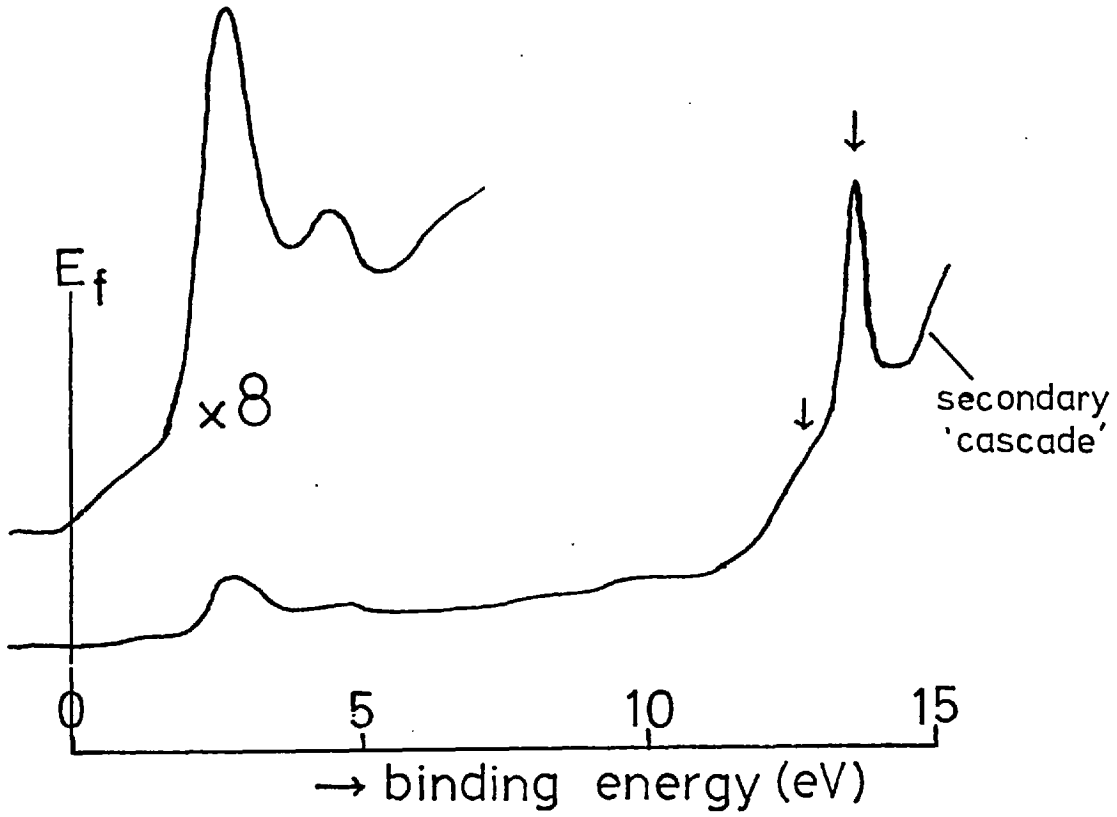

7c (Shepherd & Williams)

7d

(Willis et al)

Comparison between the energies of maxima observed in the SEE spectrum and critical points in the theoretical conduction-band structure at which high densities of final states would be expected.

Conduction-band state	Energy with respect to Fermi level (eV) Theoretical	Observed
Γ_{3u}^{+}	7.5	7.7±0.5
Q_{1u}^{+}	8.0	8.7±0.5
Γ_{2g}^{-}	10.5	12.2±0.5
Γ_{1u}^{+}	11.5	13.2±0.5
P_3^{+}	13.5	14.7±0.5
Q_{2u}^{+}	17.5	16.7±0.5
Q_{1g}^{+}	18.5	19.2±0.5
P_1^{+}	22.0	22.2±0.5

at energies up to about 25 eV which they correlated with the critical points of Painter and Ellis's calculation. Figure 7d reproduces this comparison. Fair agreement is generally observed though it may be noted that deviations between the observed and theoretical values are comparable with the spacings. Attempts were made in the earlier paper[115] to relate the threshold energies (of the incident electrons) at which the various structures appeared to interband transition energies and 'tentative assignments' were made. One difficulty in this attempt to extend the range of information retrievable with SEE is that indirect transitions may also occur. Particularly in view of the weakness of many of the features it would not seem entirely justified to suppose that such processes will have only a 'smearing effect'.

7.3.2 Below the Vacuum Level

SEE, of course, cannot provide information on conduction band states below the vacuum level. However, a narrow peak is observed[117] in the reflectivity spectrum of graphite at a photon energy of 4.6 eV which was assigned to transitions between the π bands at Q (arrowed in figure 7b). The non-empirical band calculation of Painter and Ellis gives precise agreement for the separation of the π bands at this point. However, the symmetrical disposition of the π bands would imply that a peak might be expected in the valence band at -2.3 eV whereas the sharp peak observed by Shepherd and Williams (see figure 7c) occurs at -3.0 eV. Recent angular resolved photoemission data by Williams, Latham and Wood[118] provide clear evidence that the calculated π valence band is too high at Q. It is therefore suggested that the critical point Q_{2g}^{-} may occur at 1.6 eV rather than 2.3. In fact, the density of states histogram (actually for the 3-D calculation, figure 7e) does not suggest any strong

Graphite - SEE & theory

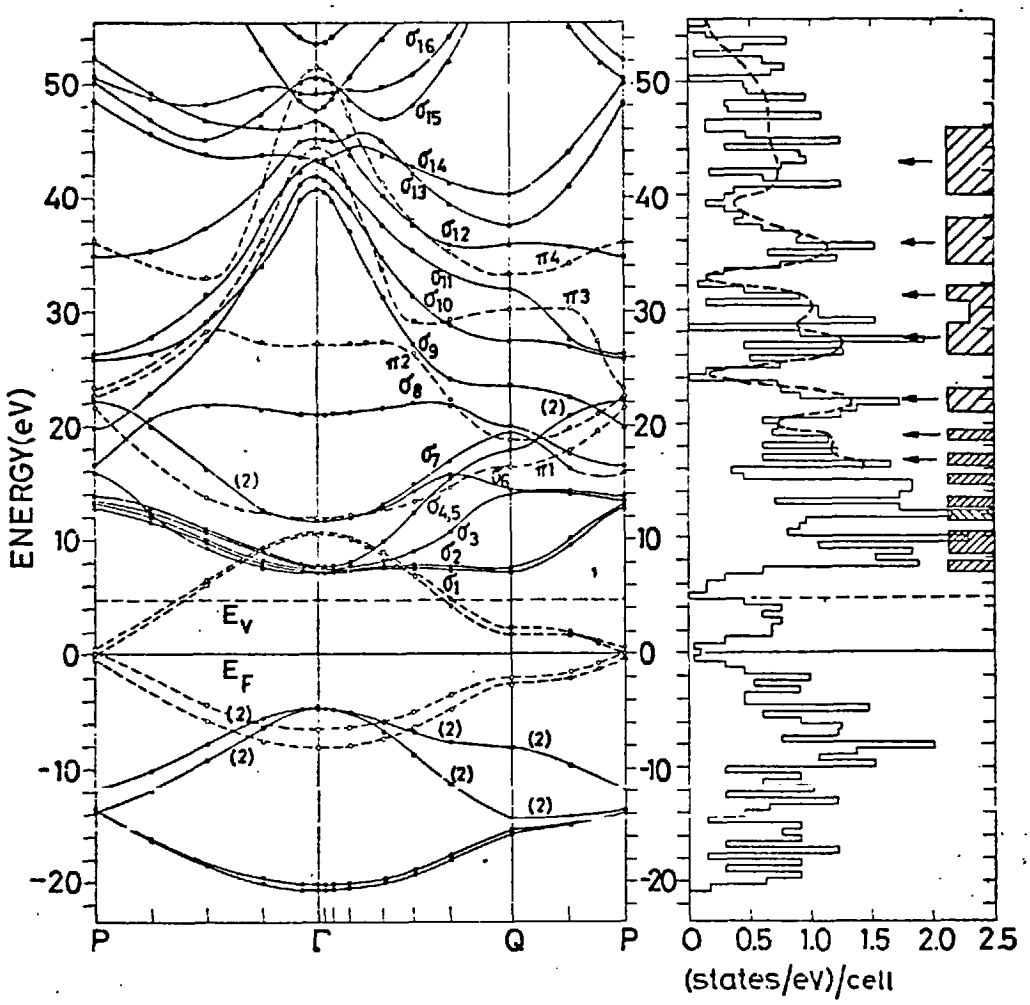

7e (Willis et al)

structure in the range E_f to E_v (the vacuum level at 4.7 eV relative to E_f in graphite). It is possible, however, that the suggested shift of Q_{2g}^- to lower energy would flatten the band along QP leading to an enhancement in the d.o.s. close to this energy.

7.3.3 High Energy SEE Observations

In a more recent paper, Willis, Fitton and Painter[24] extended both SEE observations and the band structure calculations to higher energies ($\sim$ 55 eV relative to E_f). The 3s and 3p atomic orbitals were also used in constructing the Bloch basis set and the calculation was a 3-D one. The very weak high energy features of the SEE spectrum were resolved by obtaining the second derivative of the energy distribution function. Figure 7e shows these results where good agreement is found at high energies between the smoothed calculated d.o.s. and experimental observations (indicated by the shaded blocks).

7.3.4 Summary - Conduction Band d.o.s. in Graphite

Experiments suggest that two principal features occur close above the Fermi level at $\sim$ 1.6 eV and 7.5 eV with a further lesser peak at 8.3 eV. These last two features in particular correlate extremely closely with the minima in the lowest σ conduction band of the Painter and Ellis scheme, though the d.o.s. histogram does not indicate such a significant feature as might have been anticipated. Further structure is predicted and observed up to very high energies.

7.4 Previous APS Work on Graphite and the Role of Plasmons

7.4.1 SXAPS

The SXAPS of graphite has been studied by Park and Houston[16] (PH) and Bradshaw and Menzel[17] (BM). In both cases six peaks were resolved over an energy range of some 30 eV with a broad hump about 45 eV from threshold. (PH actually observed all six peaks only in the case of graphite contamination on nickel). In both cases essentially the same conclusions were reached, BM giving a more detailed analysis. They noted that the separation of the first two peaks is close to the plasmon energy namely 7.0 eV in graphite (Liang and Cundy[46] quote a value 7.2, but 7.0 is the value more usually given e.g. by Zeppenfeld for this the 'π loss'). This plasmon behaviour in graphite is also confirmed by optical measurements[117]. (The σ loss occurs at around 27 - 28 eV).

The separations of subsequent pairs of peaks decreased monotonically except for the 5th/6th. In fact, as BM noted, the sixth peak is separated from the first by some 29.6 eV which is close to the σ loss energy. They suggested that the decrease in peak separations throughout the rest of the series was indicative of anharmonic plasmon behaviour. In the data of BM and PH the peak widths are all essentially the same and PH noted that this implied that the plasmon lifetime is not a determining influence.

Subsequently Bradshaw et al.[45] compared the results of SXAPS, XPS, PAPS (to be described below) and ionisation loss spectroscopy (or characteristic loss spectroscopy (CLS)). This last can be briefly described as being analogous to Auger Electron Spectroscopy differing in that it is the structures whose energies depend upon the incident electrons that are of interest. Information directly related to the conduction band is expected, and in common

with PAPS, the number of slow electrons as defined by Langreth[9] is conserved. Bradshaw et al. were mainly concerned, however, with the SXAPS and XPS data; in both cases the number of slow electrons is not conserved and strong plasmon coupling is possible. But, in fact, the plasmon satellite observed in XPS is smaller by about two orders of magnitude than the second peak of the SXAP spectrum (relative to the first in each case). They proposed a model attempting to explain this discrepancy in terms of different coupling constants.

7.4.2 Angular Measurements

In the usual SXAPS set up electrons thermionically emitted from a filament are attracted to the positively biased sample and although the electric field probably tends to align the electron beam normal to the surface there is likely to be significant range of angles. Any $\underline{k}$ dependence of the initial or final state was ignored in section 3.1, but it is possible that matrix elements variations will lead to changes in the spectrum when the angle of incidence is varied. The results of a very simple attempt to investigate such an angular dependence are to be presented below and, while a more sophisticated theory would be required to interpret them, there are one or two features of interest. A further point is that it was apparently[16] pointed out by Langreth that extrinsic coupling to plasmons should decrease as the angle of incidence is increased. In fact, the net effect on the energy loss spectrum as observed by Zeppenfeld[119] and predicted from optical data by Greenaway et al.[117] is a decrease and shift to lower energy as the interband transition at 4.6 eV becomes increasingly significant. Bradshaw and Menzel obtained SXAPS data by bombarding a graphite edge and, observing no change in the spectrum concluded the plasmon coupling to be intrinsic. Verhoeven and Kistemaker[120] attempted measurements

as a function of angle of incidence using an electron gun but did not really obtain statistically significant data. One trend, however, between four spectra which probably is statistically valid is that the first peak seems to decrease in relative intensity as the angle of incidence is increased.

7.4.3 PAPS

In photon appearance potential spectroscopy (PAPS) it is the photon induced electron yield which is detected. Because the pentration depth of photons is much greater than for electrons and there is no restriction on electrons leaving the solid without inelastic collisions, it can be regarded as essentially a bulk probe. As a simple approximation to a monochromatic X-ray source the bremsstrahlung emission from a transition element has been used[65] since this should reflect the high density of unfilled d states at the high energy cut-off. The observed (derivative) spectrum can be regarded as a convolution product of the one electron density of states of the sample with the derivative of the bremsstrahlung spectrum of the 'target'. To the extent that the (smaller) negative dip of the latter can be ignored this product can be approximated by the former.

Bradshaw et al. obtained the PAPS for aquadag. This was painted on to the photocathode of a normal SXAPS set-up enabling a large surfact area to be otained in view of the extremely weak signal that is observed. They resolved two peaks separated by $\sim$ 7 eV in good agreement with the picture of the conduction band d.o.s. of section 7.3.4.

7.4.4 Plasmons in SXAPS

In contrast with the interpretations which have been suggested for the SXAPS of graphite, it was found in chapter 6 that strong spectral features in the SXAPS of the layered transition metal dichalcogenides were in good agreement with the conduction band self-convolution model. The only plasmon influcences detected were the weak σ losses observed in TiS_2 and $TiSe_2$.

In general we note that SXAP spectra for transition elements are dominated by the narrow d states, but observations on non-transition elements are very frequently[72,69] characterised by strong structure over a wide energy range. Carbon[36] in forms other than graphite gives very different spectra but still complex over a wide energy span, and without 'satellite' character. Even where relatively strong plasmon satellites are found in XPS, e.g. Li[44], the corresponding SXAPS still shows only a relatively weak effect.

We shall show in 7.5 that a conduction band argument fits the detailed observations on the APS of graphite considerably better than the plasmon model and brings this material into line with all other APS observations.

7.4.5 Plasmons in SEE

Before discussing the present APS results in the context of a conduction band model it is relevant to briefly consider the possible influence of plasmons in SEE. Willis et al.[24] noted two mechanisms: (a) 'hot' electrons may excite plasmons or (b) decaying plasmons may excite valence electrons. In either event such effects are dictated by the availability of (a) empty electron states or (b) electrons and observations are most likely to take the form of a discontinuity corresponding to the Fermi level at $E = h\omega - \phi$ (E is energy of escaping electron, ω the plasma frequency and ϕ

the work function). Willis et al. suggest that such effects are likely to be strongest in free electron like metals and indeed weak features have been observed[121] corresponding to the bulk and surface plasmon in aluminium. However, they do not consider the possibility that the sharp peak found in SEE for graphite could have such origins in view of the difference in energy, and it would in any case be difficult to reconcile this structure with the foregoing considerations.

7.5 APS of Graphite

7.5.1 Observations in SXAPS

Figure 7f shows the first six peaks of the graphite spectrum; the upper trace (A) is the usual first derivative of the X-ray yield and the lower trace (B) is the digitally-obtained second derivative. These data were obtained with a modulation amplitude of 0.2 volts r.m.s. which is the smallest amplitude necessary since the spectrum scarcely differs at twice this value. Such an amplitude (0.4) applies in the case of figure 7g which shows the extended spectrum (C) over 125 eV. A linear background was subtracted to give trace D which is shown at increased gain while E shows the (2nd) derivative over the region of the 45 eV 'hump'.

Referring to figure 7f it is immediately apparent the PH's supposition that all the peaks (identified hitherto as α, β, γ ...) have essentially the same width is inaccurate; as can be clearly seen in the lower trace the first three are of similar width but distinctly sharper than subsequent ones. A measure of the peak width defined by the full width at half maximum (fwhm) can be readily obtained for α as 1.6 eV. This quantity is ill-defined for the other peaks, however, on account of the background; an alternative

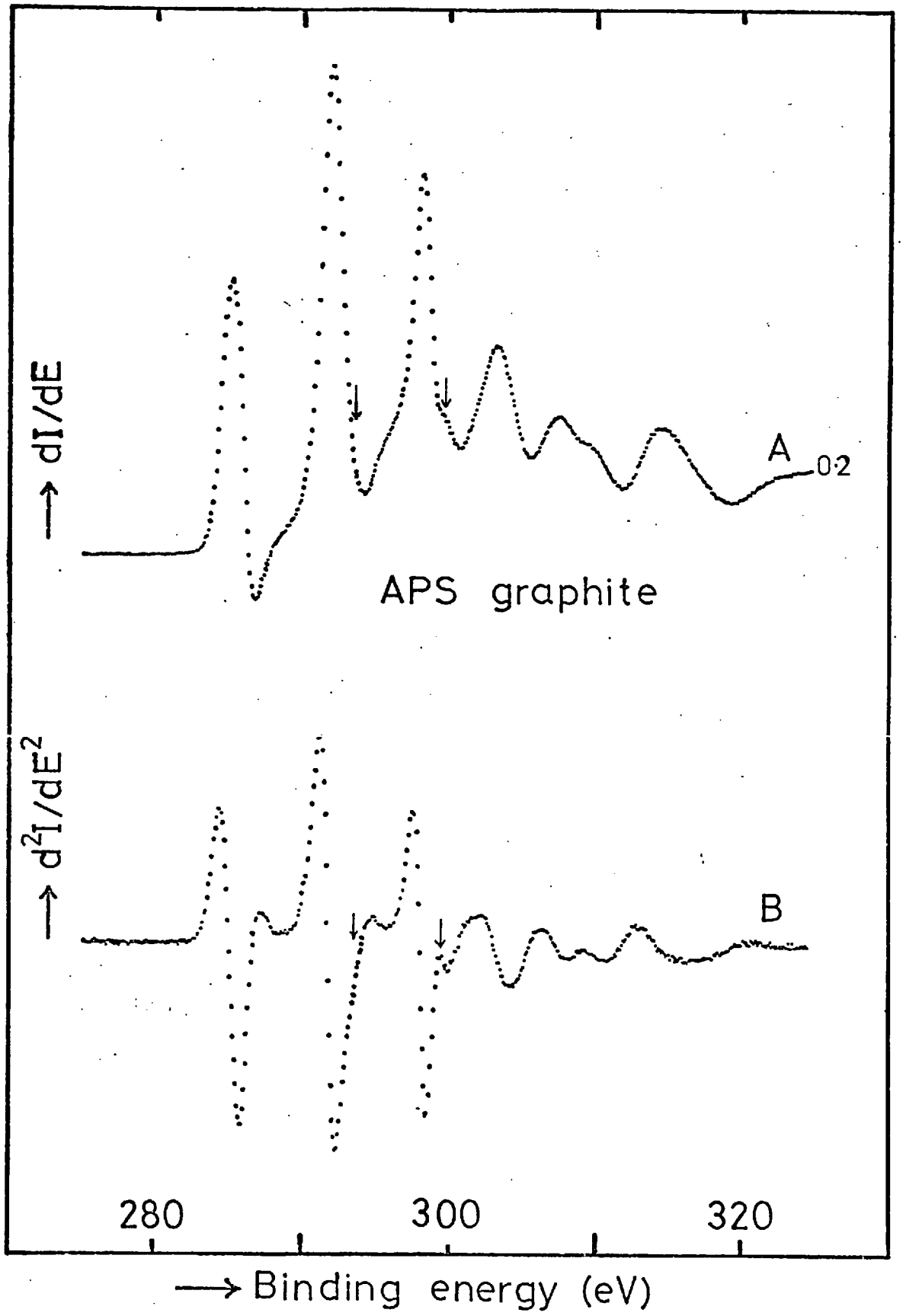

7f

APS graphite – extended scan

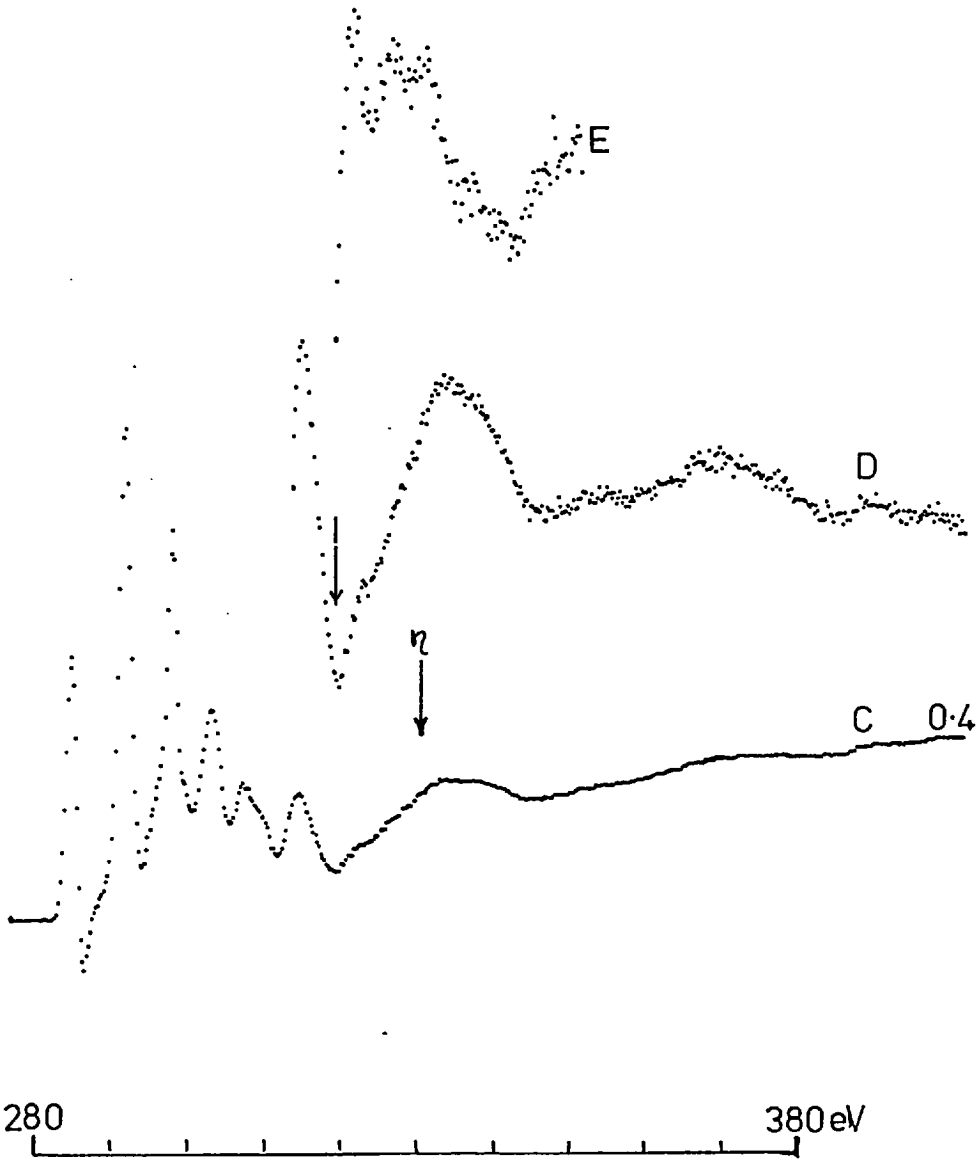

7g

measure which gives a consistent means of determining the relative sharpness of these features is obtained from the separation of maxima and minima in B. This quantity corresponds to the separation of the points of inflexion in A, and gives for α, β, γ respectively 1.5, 1.1, 0.95 eV. Even this is less well defined for subsequent peaks but for δ gives a value of about 2.3 eV.

Again as is best seen in B, β has a distinct asymmetry signified by the arrowed 'tailing' while γ has at its base a step-like structure in A and corresponding feature in B. In fact if γ (which is sharper than β) were less well resolved it would closely resemble β in shape. Observing in A just the portion of γ above the step it is noteworthy that there is in fact a slight asymmetry such that the high energy edge is sharper than the low energy one. It is also noted that ε has a doublet structure and δ in B is slightly flat topped indicative that we may be on the verge of resolving a shoulder on the low energy edge in A. While the details referred to above may be quite subtle, it is well justified to draw attention to them on account of their precise reproducibility upon repeated high vacuum cleaves (including one UHV cleave).

Turning to the extended energy scan in figure 7g it is characteristic of the spectrum as a whole that the sharp structure expanded in figure 7f ends summarily with a marked minimum (arrowed). This is followed by the broad hump referred to previously which the derivative trace E shows has a number of components. A lesser minimum is then followed by weak structure up to high energies.

7.5.2 Deconvolution Results

The first three sharp peaks of the spectrum are strikingly reminiscent of the derivative of the self-convolution of a doubly

peaked conduction band (see figure 6m); while the narrowing observed through the progression α, β, γ is consistent with the higher energy peak in the conduction band being the narrower. (The peak observed in SEE (photon-induced) is about 0.5 eV wide). In contrast the observed progressive narrowing is contrary to the interpretation that β and γ are satellites of α in which case they should be at least as broad.

The implied conduction band d.o.s. was obtained by fitting to the region of the first two peaks α and β. These results are shown in figure 7h in which (a) shows the obtained d.o.s. and (b) indicates the accuracy of the fit by comparing the 'real' and 'calculated' spectra.

Two main peaks occur in (a) with a lesser one some 1 eV from the second. This last feature is required to fit to the slight 'tailing' of β as pointed out above, and thus depends on a rather precise application of the self-convolution model to an extent which would not be expected. This view is supported by the fact that the self-convolution of (a) alone results in a more complex third peak than is observed. The result is that rapid variations of the d.o.s. are required at higher energies to counter these. Unlike the first two peaks whose d.o.s. origin is unambiguous these rapid variations depend crucially on an accurate self-convolution. Effectively, it is the basic deconvolution problem, and it is necessary to accept a less accurate fit to proceed further.

Such a fit is shown in figure 7i, together with its predicted spectrum; it was obtained by smoothing the trial function from the second peak on at each iteration. A strong feature is predicted in the d.o.s. in the region of the third peak and is thus open to doubt without further justification.

Deconvolution of graphite

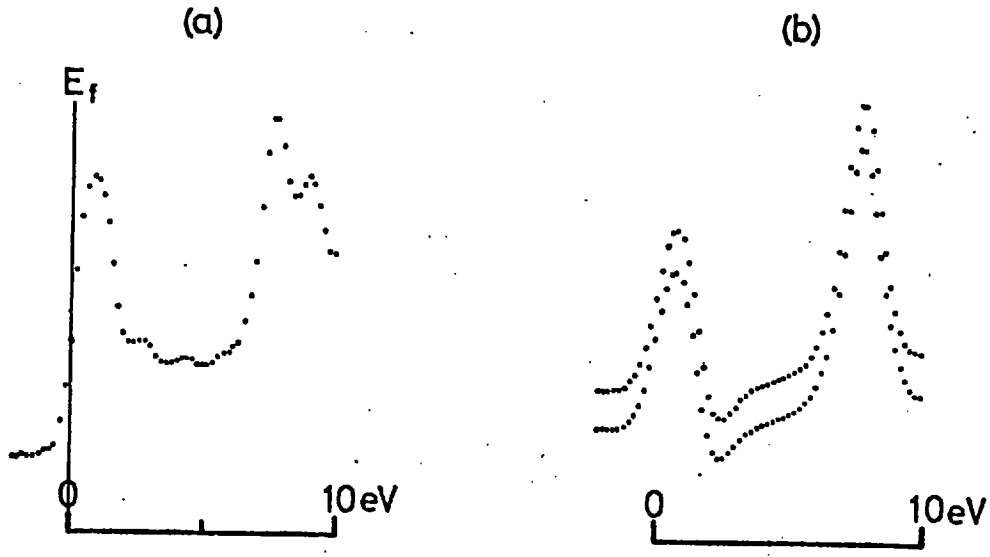

7h

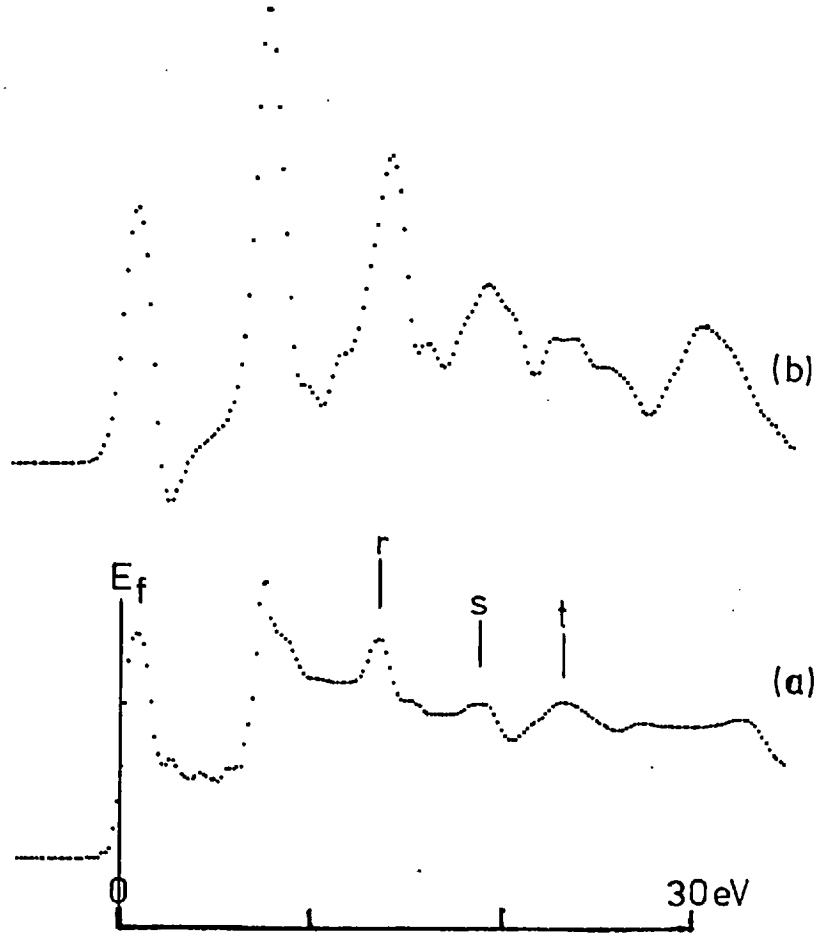

7i

7.5.3 A Semi-Quantitative Model (SQM)

7.5.3.1 α, β, γ

As we have seen two sharp peaks in the conduction band are expected to give rise to three in the SXAPS such as are observed for graphite. That the spacing differs slightly as noted originally by Bradshaw and Menzel may indicate some departure from an accurate self-convolution model though that is not unexpected. The deconvolution fit to the first two peaks predicts the energies of the conduction band states as 0.9 and 7.6 (± 0.5) eV in very sound agreement with the conduction band picture arrived at in section 7.4. In fact the spacing is almost identical to that found in the spectrum as would be anticipated for well resolved peaks. The smaller peak at 8.8 eV is also in good agreement with SEE observations, but as mentioned above the validity of this is open to question. It seems very probable that it is over-emphasized in figure 7h, but that a weak feature is implied by the SXAPS. This is supported by the observation that there is a step at the base of γ which overall looks rather like a better resolved β consistent with the present conclusions regarding the widths of the conduction band peaks. The asymmetric nature of β is not in evidence for γ and is thus not consistent with an interpretation in terms of inelastic scattering.

7.5.3.2 δ, ε, ζ

The origin of the subsequent three peaks is more complicated since as we proceed to higher energies there is more and more preceding structure to influence the spectral shape. However, to a first approximation we may expect such features to result from a convolution product of the derivative of the two dominant peaks with

whatever structure follows; and to simplify matters we can, very reasonably, neglect the relatively small negative dips that result in differentiating the d.o.s. of 7h. The required function can thus be regarded as consisting of two δ functions of separation close to 6.8 eV. The implication is that, initially at least, we attempt to pair features in the spectrum at separations of 6.8 eV. The associations 'y' and 'z' of figure 7j, taking advantage of the doublet structure of ε, follow immediately. However, we would expect the relative intensities of each pair to be similar and this is clearly not so. This can be remedied if δ consists of two closely spaced components (evidence for this will be given in the angular results of section 7.5.6), and 'x' added. There is some evidence of the implied peak between β and γ but strong variations in this region do not allow a positive identification.

Thus δ, ε, ζ imply three peaks in the d.o.s. (r,s,t) at 12.7, 18.7 and 23.5 (± 1) eV (referred to α at 0.9 eV) which are in good agreement with the deconvolution results of figure 7i. The first two features that would be produced by the self-convolution of this structure are indicated by the dashed arrows in figure 7j and may thus contribute to ε and ζ. In fact it is easy to see that a consistent picture can be built up without s, but not r or t.

7.5.4 Comparison with Theory

As noted previously the sharp structure ends with a notable minimum which, relative to α at 0.9 eV occurs at 35.1 eV. This corresponds roughly to a minimum in the d.o.s. at about 28.3 consistent with the above. We accordingly surmise that a downward step occurs in the conduction band d.o.s. at 27.3 ± 1.5 eV. This is close to the conduction band width (∿ 22 eV) calculated by Painter and Ellis[112] based on 2s and 2p atomic orbitals. We might expect

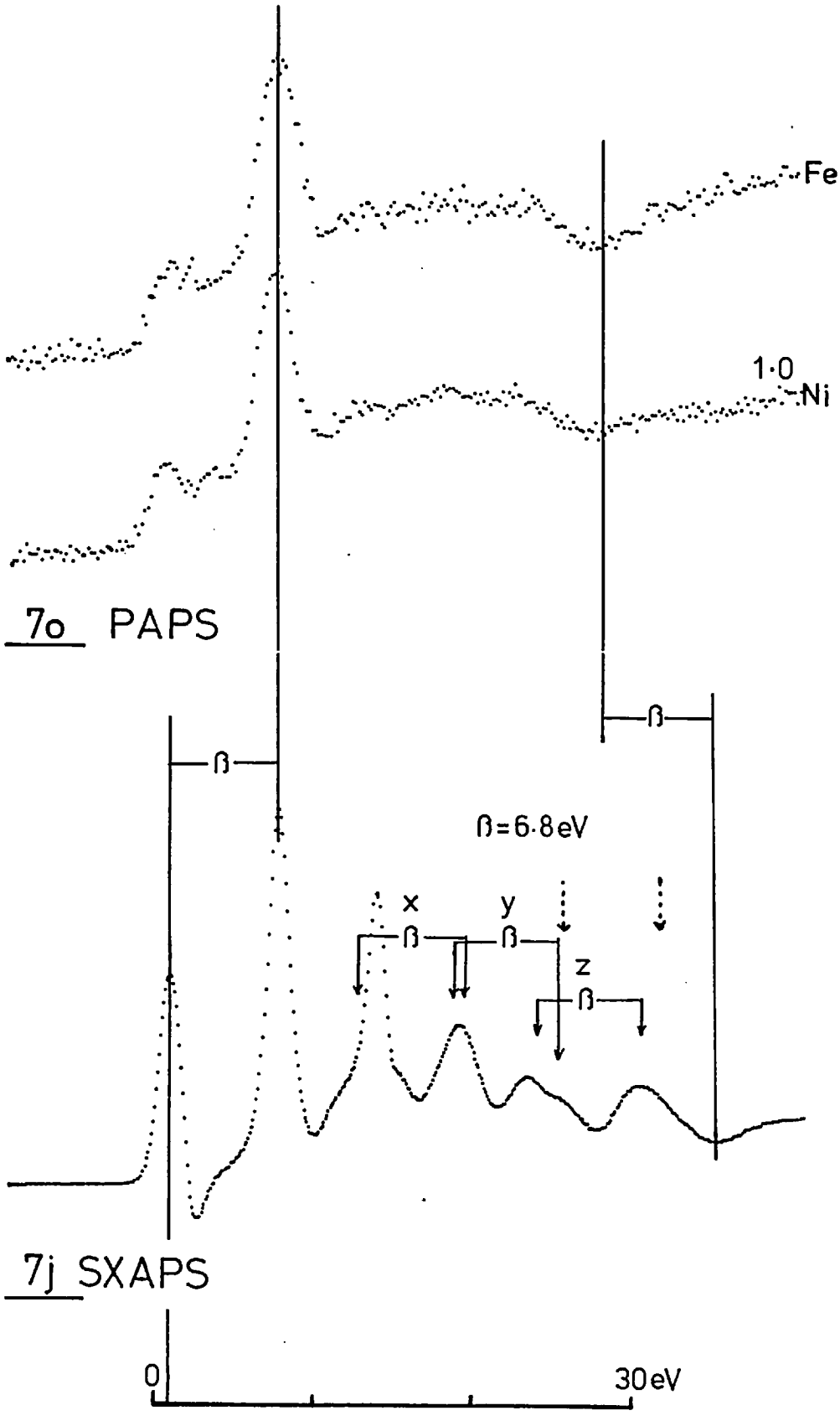
Fe
1·0
Ni
7o PAPS
ß
ß
ß=6·8eV
x
y
z
ß
ß
ß
7j SXAPS
0
30eV

that the poorer overlap of the 1s with orbitals of principal quantum number greater than 2 would indeed lead to a decreased probability for scattering to such states.

The extended calculation in the paper by Willis, Fitton and Painter[24] also shows the density of states histograms. Willis et al. smoothed only the higher energy regions, but it cannot be claimed that their SEE data correlates with the fine structure of the histograms or indeed that experiment would be expected to retrieve such detail. In order to make a useful comparison with SXAPS therefore these histograms were digitised and smoothed by successive applications of a 3-point smooth routine. Figure 7k shows the effect of four such applications and the basic structure up to about 24 eV evidently consists of five peaks in good qualitative agreement with the model of 7.5.3. Figure 71 tabulates the energies of these five as given by the SQM, deconvolution and theory (in eV rel. to Ef).

	p	q	r	s	t
SQM	0.9	7.6 (8.8)	12.7	18.7	23.5
Dec	0.9	7.6 (8.8)	13.5	18.9	23.5
Theory	3.0	8.4	13.3	16.7	21.3

figure 71

Quantitative agreement between APS and theory is not achieved, but the overall picture presented by each is close enough to suggest that both the intrepretation of the APS and the Painter and Ellis band scheme are basically correct. Peak s which is not essential to the SQM is rather weak in the theoretical curve, though q is not so dominant or sharp as APS (and SEE) would suggest and a doublet structure is not clearly evident. Again p is somewhat weaker than APS implies and this point will be referred to later.

Theory conduction band d.o.s.

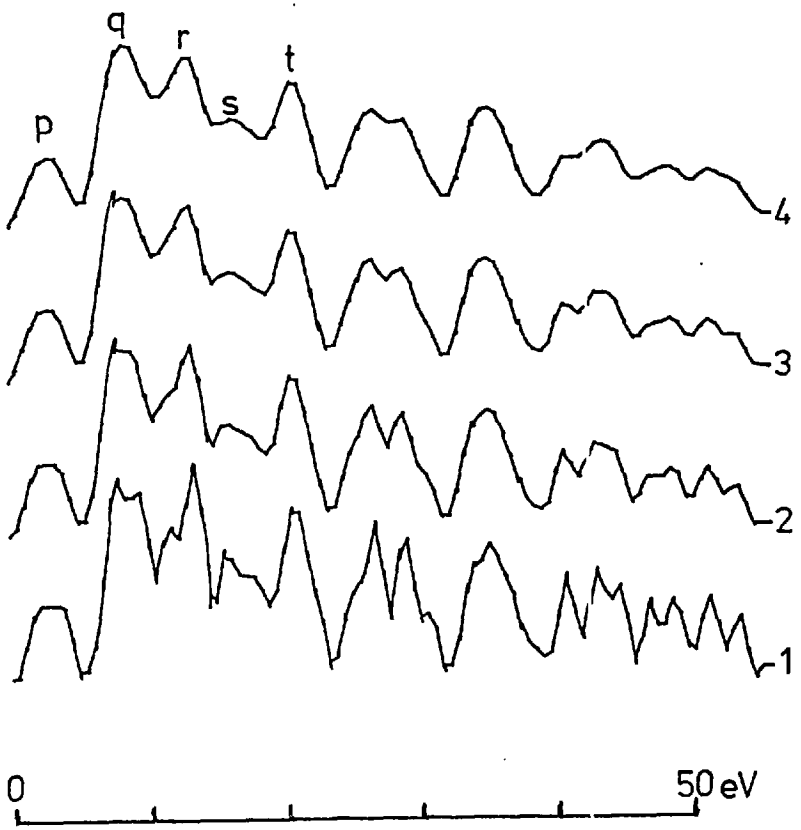

successive applications

of 3-point smooth routine

7k (from data of Willis et al)

7.5.5 Extended Structure

Beyond ζ there is a broad hump as noted previously and shown in figure 7g. Clearly it will not be possible to find an unambiguous interpretation for this. Basically it would seem likely to originate from either the convolution product of p/q with higher energy structure or the self-convolution of r/s/t or more probably both. The last feature of the latter would occur at ∿ 47 eV (η in figure 7g). This implies that higher energy features based on 3s 3p atomic orbitals at least contribute. As before the minimum around 60 eV leads us to a conduction band step close to 52 eV in rough agreement with the calculation of Willis et al. though they do not show the full extent of the energy bands.

7.5.6 Angular Results

In an attempt to obtain more oblique angles of incidence, a slightly modified experimental arrangement was employed in which the graphite sample was mounted at ∿ 45° to the usual orientation and a small grid was inserted between filament and sample as sketched in figure 7m. The grid was held at the same potential as the sample

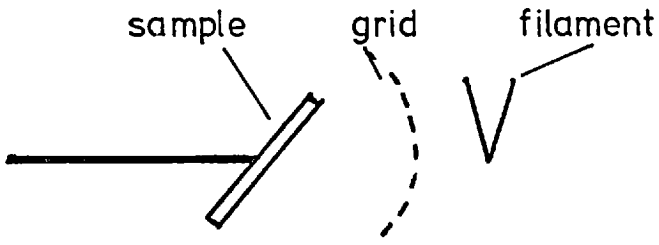

7m

(except for the potential modulation) so as to obtain a pseudo field-free region close to the surface.

The results obtained in this manner are shown in figure 7n for θ ∿ 35° (A) and ∿ 50° (B). A small amount of control over

Angular results

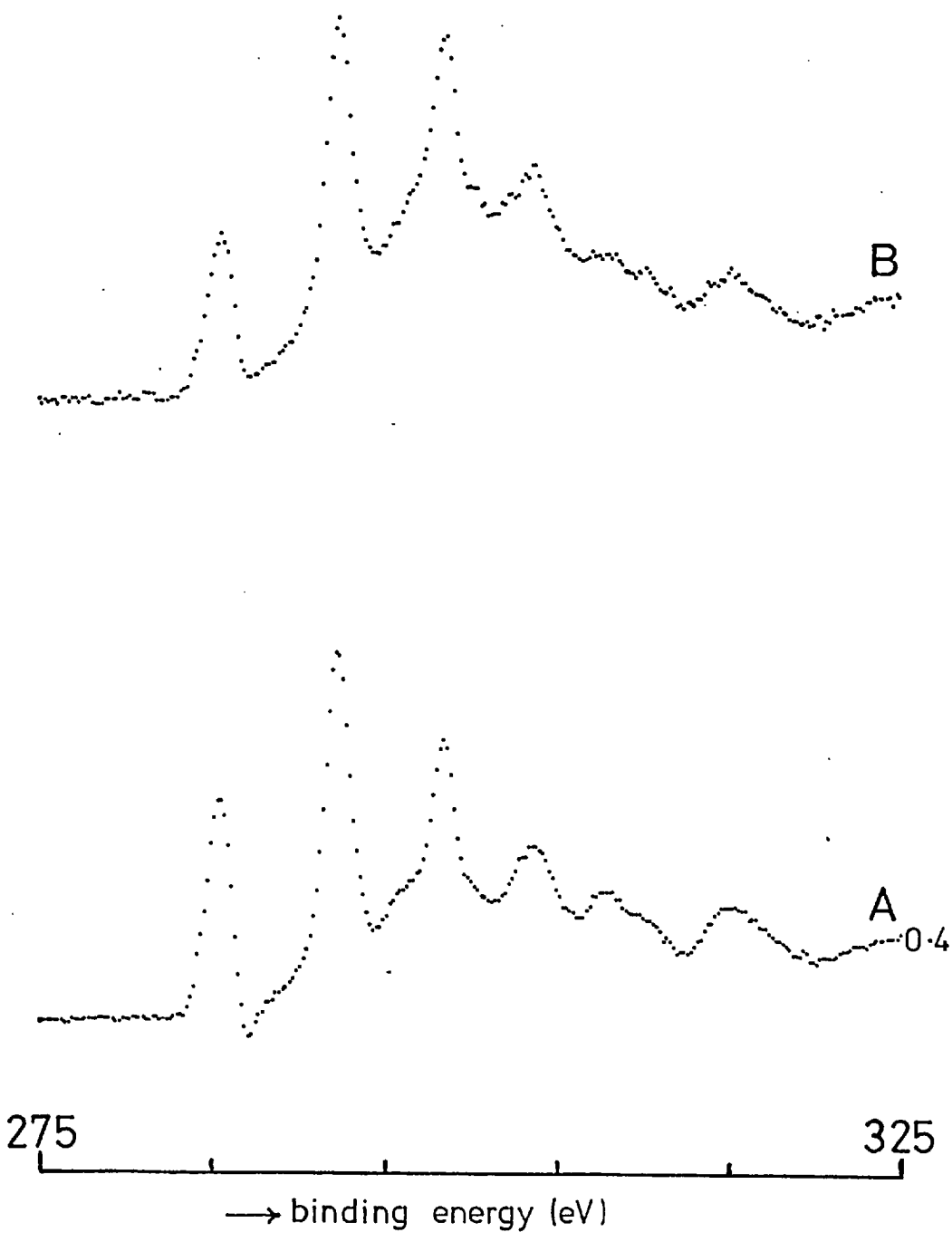

7n

θ was to be had via the rotary drive (simultaneously moving the sample away from the filament). This extremely crude set-up can hardly be expected to give anything like a collimated beam of electrons and the most that can be said is that B probably corresponds to a larger angle of incidence than A.

Trace A in fact is extremely like the spectrum of figure 7f though α seems slightly more intense and the splitting of ε more marked. In trace B, however, the spectrum differs appreciably with β and γ of similar height and α somewhat diminished. At the same time a marked shoulder develops on δ. It should be emphasized that these data cannot be relied upon to the same extent as those considered previously since they have not been reproduced, but the effect whereby the shoulder on δ becomes more marked at large angles of incidence was confirmed by repeated scans in this region.

The form of α, β, γ in trace B is in fact strikingly similar to a spectrum obtained by Bradshaw and Menzel[17] for a less well ordered graphite sample. While there are considerable uncertainties in the present data regarding the angles of incidence and those of Verhoeven and Kistemaker[120] are rather noisy, both seem to indicate a decrease of the first peak as the angle of incidence increases implying a reduced probability for scattering to the lower π state. It is evident that effects due to matrix elements are entering though any attempt here to interpret this or a similar observation in PAPS would almost certainly be too simplistic. Simultaneously with the weakening of α, the shoulder on δ develops. It is tentatively suggested that the latter corresponds to the weakening of the lower energy component which may therefore be best 'paired' with a higher energy feature in view of the correlation with α. This was assumed in figure 7j but clearly the energies derived by no means critically depend on this assumption.

It seems likely that a range of angles of incidence occur in the usual APS set-up and for a collimated electron beam normal to the surface the first peak would be larger than has been observed here as suggested by the data of Verhoeven and Kistemaker.

7.5.7 PAPS of Graphite

The PAPS of pyrolytic graphite was obtained using a slab approximately 3 x 1 cms., cleaved in air since the method is not surface sensitive. The signal was extremely weak and the data of figure 7o took many hours to acquire using Fe and Ni targets. After a small peak immediately above the onset a dominant peak again occurs close to 7.6 eV. The only other structure which can be clearly identified is a negative step at about 26.2 eV with a diffuse minimum close to 28.0 eV in very fair agreement with the interpretation given to the SXAPS.

It is noticeable that the peak at 7.6 eV is much stronger than in the spectrum obtained by Bradshaw et al.[45]. This may result from the use of an oriented graphite sample and thus reflects matrix elements effects.

7.5.8 Comparison of XPS and SXAPS

As noted by Ertl and Wandelt[67] in the case of iron and Nilsson and Kanski[72] for beryllium,when the Fermi level occurs close to a minimum in the density of states a 'slow onset' occurs in APS, and, for iron, this was revealed in the comparison with XPS[66]. Graphite's semi-metallic properties provide the classic example of such an occurrence and it is interesting to make such a comparison here. Figure 7p shows the differentiated XPS (A) superimposed on the first peak of the graphite SXAPS (B) and also from the 'angular' spectrum

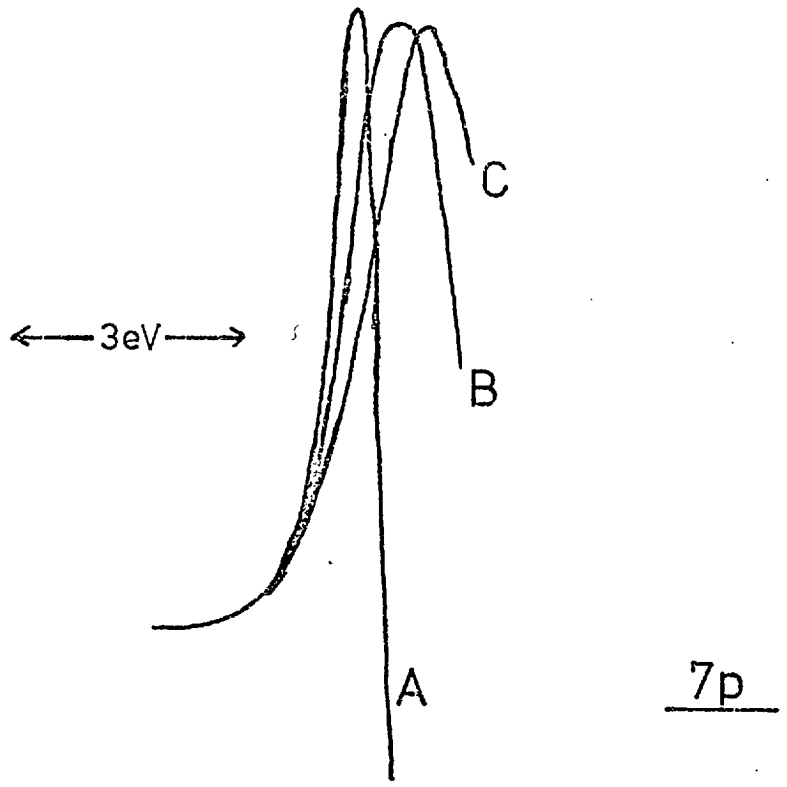

(top trace, figure 7n, the lower trace being near identical with B here). As can be seen the XPS does indeed show a sharper rise and the effect is even more marked in proceeding to the angular spectrum. As noted earlier the first peak is more intense than would be expected purely from a density of states standpoint and decreases as the angle of incidence increases. The implication is that the scattering to states close above the Fermi level is enhanced by matrix element effects at near normal incidence but is more nearly reflecting the true density of states as the angle increases and this accords with the observed trend in figure 7p.

7.6 Boron Nitride

7.6.1 XPS Results

Figure 7q shows XPS results for boron nitride and also graphite. As would be expected the loss peaks following the main

XPS results

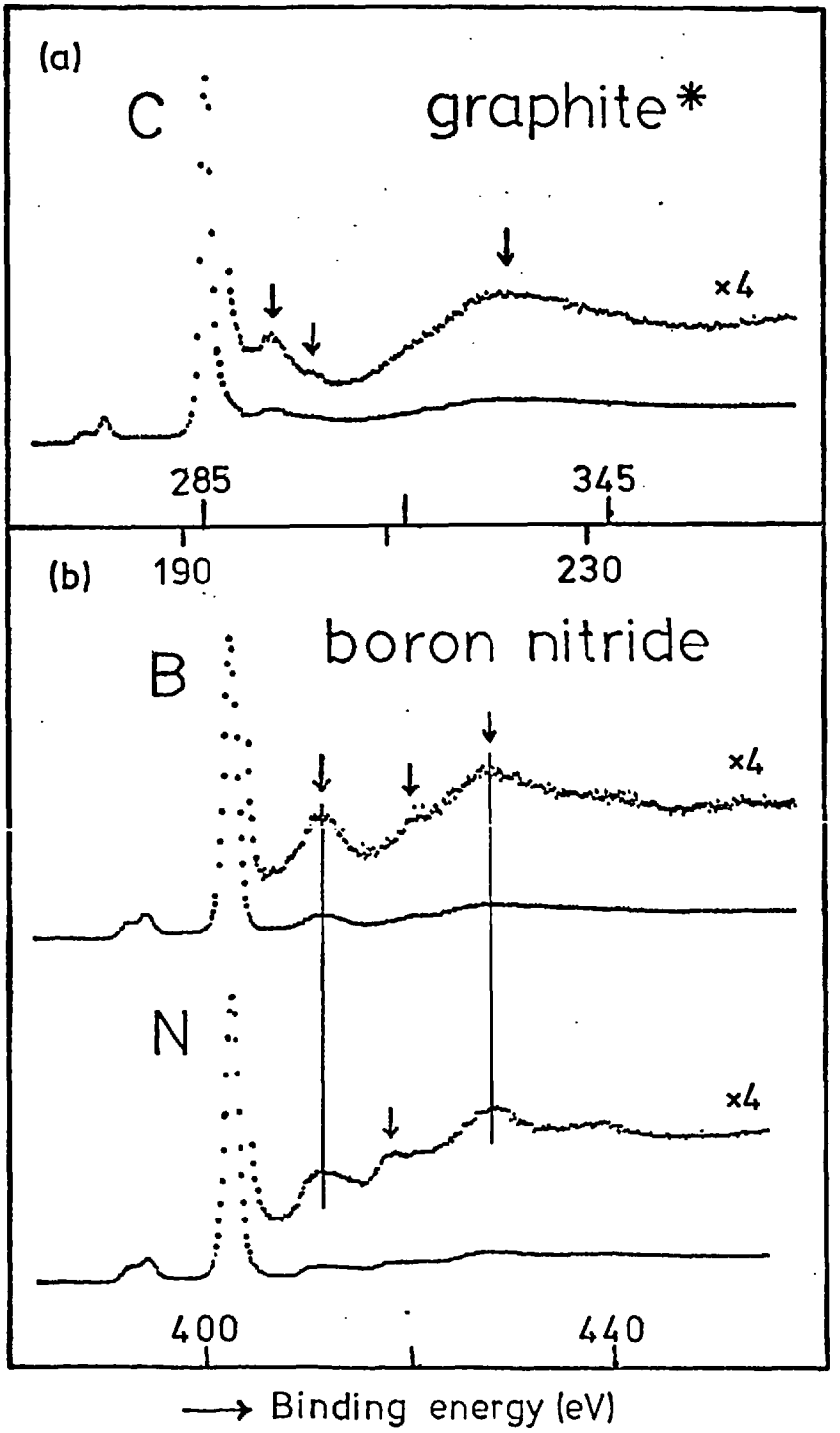

7q (*P. M. Williams)

1s core level peaks are very close for B and N and qualitatively similar to C. In accord with other observations the π and σ losses are observed in graphite at 7 and 28 eV respectively. A weaker feature occurs at about 10.5 eV which may be due to an interband transition.

For boron nitride comparison of the loss background is facilitated by alignment of the main peaks. For both B and N losses occur at 9 and 26 eV, and, in view of the close relationship to graphite, these may be interpreted as giving the π and σ plasmon energies in BN. Other structures occur as tabulated in figure 7r, at 18 and 15.5 eV for B and N respectively.

XPS		SXAPS	
B	N	B	N
9.0	9.0	6.0	5.0
18.0	15.5	-	6.5
26.0	26.0	12.0	13.5
37.0	37.0		

Figure 7r

(Energies in eV rel. 1st peak at 0)

These, as well as the weak features at about 37 eV, may be due to interband transitons. That different energies are possible for B and N suggests that the coupling is intrinsic to the core excitation and the differences reflect dissimilar local densities of states around B and N atoms. The π and σ losses, of course, involve the collective excitation of all the valence electrons and would be expected to occur at the same energy in each case as observed.

7.6.2 SXAPS Results and Implications

Figure 7s shows the SXAPS results for boron nitride. Energies of the peaks relative to the first at 0 eV are listed in figure 7r. Unlike graphite, there is no correlation whatever between the π loss at 9 eV and the various structures observed in APS although they are qualitatively similar to the APS of graphite. Clearly it is not possible to interpret the APS of boron nitride in terms of a simple plasmon coupling argument and it seems probable that a conduction band model is applicable as for graphite.

Experimentally the SXAPS of boron nitride is complicated by its insulating properties so that it may charge under the electron beam. Fortunately it displays a tendency to cleave very thinly on occasions minimising such charging effects and enabling the data of 7s to be obtained. These difficulties prevented the same degree of reproducibility as was found for graphite being achieved. It is, therefore, probably not so well justified to make a detailed dissection of these spectra, and, lacking guidance from other sources, this is in any case less easy. However, one or two general observations are possible. Firstly it is noted that while the B and N spectra are in very reasonable agreement in respect of peak positions they differ appreciably in actual shape. This we assume implies different local densities of unfilled states specific to B and N atoms as was observed in the XPS loss background and would indeed be anticipated.

By analogy with graphite we may reasonably associate the first peak of the spectrum with the lowest unfilled π states while the second probably has its origins in the lowest σ conduction bands. The separation ($\sim$ 6 eV) indicates a similar splitting of bands as in graphite. Because the Fermi level lies below the bottom of the conduction band and there are uncertainties regarding absolute binding

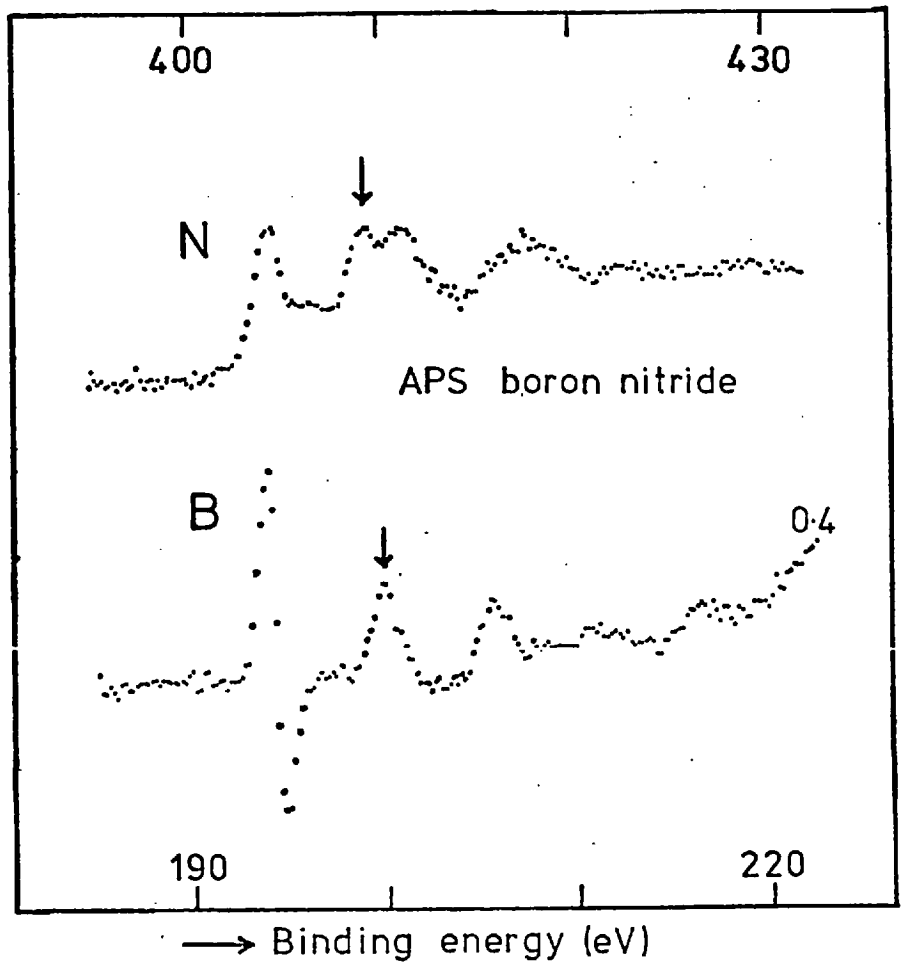

7s

energy scales in both XPS and SXAPS due to possible charging, it is not possible to deduce anything about the actual positions of the conduction bands. A final point worthy of note is that there is a marked negative dip following the first peak of the B 1s spectrum which is absent for N. This implies a larger density of unfilled π states at B sites in accord with expectation.

7.7 Summary

The SXAPS of pyrolitic graphite has been obtained revealing considerably more detail than was previously observed and this has enabled the previous plasmon coupling argument that was used to be shown unsatisfactory. At the same time it has proved possible to account in detail for the complexities of the spectrum in terms of the self-convolution model, the implications of which are in good general agreement with SEE and theory, as well as the PAPS data recorded. Finally XPS and SXAPS studies of the closely related boron nitride have shown there to be no correlation between the SXAPS and the π plasmon in this case, and it is almost beyond doubt that the SXAPS of graphite is dominated by conduction band effects. Some of the above results were presented[122] at the Warwick Surface Science Conference. In fact, Bradshaw and Krause[123] as well as Houston[124] have now abandoned the plasmon coupling argument though on the basis of less satisfactory SXAPS data.

CHAPTER 8

CONCLUSIONS

The present APS studies of layer materials have proved very rewarding. The varied spectra obtained have been found quite generally explicable on the basis of a simple self-convolution approach and deconvolution has enabled a good deal of information to be derived on the conduction bands of the materials studied.

The transition metal dichalcogenides, with their crystal field split d bands, provided a novel and challenging field of study for APS, and its successful application to these makes it a very strong candidate for future conduction band investigations of transition metal compounds. The magnitude of the crystal field splitting has been determined for Ti, V and Zr compounds; and for TiS_2, gives excellent agreement with the other experimental data available though calculations seem generally to predict values which are too small.

Plasmon influences were found to be unimportant in the t.m.d. materials only rather weak σ losses being observed in the Ti compounds. In contrast the spectacular SXAPS of pyrolitic graphite was previously thought to be dominated by multiple plasmon losses. However, the higher resolution data obtained during the present studies reveal considerable detail not previously observed which has been reconciled with an interpretation rather in terms of a self-convoluted conduction band d.o.s. That plasmon influences should again be relegated to very much the minor role was verified by XPS and SXAPS studies of the isoelectronic and isostructural boron nitride.

The presence of a sharp peak, as observed in SEE and PAPS, in the conduction band of graphite, together with another close to the Fermi level, gives rise to the three sharp peaks in the SXAPS. In addition the spacing of these features modulates the remainder of the spectrum leading to the observed dramatic effect. The deduced form of the conduction band was in excellent qualitative accord with Painter and Ellis's band scheme.

Like any other technique APS has its limitations and one of these is the deconvolution requirement. A deconvolution routine has been devised and shown to be very valuable in interpreting AP spectra. However, the difficulty that haunts all deconvolution problems is that small variations in the spectrum may lead to much larger ones in the original function. For complex spectra this can lead to unrealistic density of states functions. Of course, what may or may not be 'physically realistic' is a subjective decision (except in the extreme of a negative d.o.s.). But this cannot be avoided in deconvolution since, in rejecting the 'mathematical' solution, we choose to approximate and must also choose the degree to which we approximate. Physical reality has to be paid for by inaccuracy in the fit, but this does not prevent satisfactory results being achieved.

The other major disadvantage suffered by APS is its insensitivity to some elements. Park and Houston[19] suggested that there is no systematic dependence on Z, but it is proposed here that there is at least an underlying trend of decreasing sensitivity with increasing Z. The strong variation with $N(E_f)$ is superimposed on this so that, while no trend is obvious in passing along rows of the periodic table, it seems to be generally observed that (chemically similar) elements in the same columns reveal this dependence.

The sensitivity to transition elements is dictated by the large density of unfilled d states immediately above the Fermi level

and the AP spectra show relatively strong features over a narrow, energy range. Non-transition elements generally give strong structure over a much wider energy span but the present studies indicate that in both cases the self-convolution model provides a very plausible means of interpretation in either case. And, with the clarification of the graphite spectrum, a degree of uniformity is attained where plasmons may essentially be neglected.

Of great value during the present work has proved to be the availability of the photoelectron spectrometer. Because, in this case, final states are normally high above the Fermi level, information obtained does not relate to the conduction band and intercomparison enables such effects in APS to be identified. This emphasizes the advantages of utilising more than one technique; APS and XPS are particularly well paired because information relates primarily to unfilled and filled states respectively.

No doubt the future will see many more applications for APS. Experimental refinements such as X-ray filters have enabled Andersson and Nyberg to demonstrate that the technique can be applied to gas adsorption studies. Other areas may also be opened by such increases in sensitivity; notably it would probably be feasible to undertake an investigation of the 5d transition metal dichalcogenides. The use of an electron gun to give control over the incident angle of the beam is another intriguing prospect. The extra degree of freedom may enable ambiguities to be elucidated as was tentatively proposed for the graphite spectrum.

An obvious extension of the present studies, apart from the 5d compounds mentioned above, would be to intercalated layer materials. Experimental difficulties prevented any real attempt here but if these could be surmounted then, with present experience in mind, the results would almost certainly repay the effort.

APPENDIX

Deconvolve Programme

The actual programme, written in machine code for the PDP8/f, is long and tedious so that it is not reproduced here. Instead a simplified description of the mode of operation is given.

The 'package' also contains a number of data manipulation facilities such as compression of data into half the number of channels, useful where poor statistics are achieved since it enables a direct trade-off of resolution for S/N. With 'deconvolve' selected the switch register controls the mode of operation, setting e.g. the value of 'k', and also enables any data segment to be displayed on the oscilloscope. In addition the programme is compatible with 'MCS' utilising the same core space for data, while rapid programme interchange can be made using the cassette. The data section is divided into four quarters:

(i) Spectrum

(ii) Calculated convolution product of (iii) and (iv)

(iii) Function to be deconvolved

(iv) Trial function.

Each operation - e.g. convolve, differentiate, etc. - is in the form of a subroutine which permits considerable flexibility. Thus it was trivial when setting up the programme to make allowances for possible future requirements such as non derivative data or deconvolution of a known (e.g. instrumental) function. At the heart of operation is the convolve loop:

(1) Convolve (iii) and (iv)

* (2) Differentiate

(3) Normalise

* (4) Exit to display

(5) Match calculation with spectrum (sum squares of differences)

(6) Adjust or Smooth (iv)

* (7) Copy (iv) to (iii) (for self-deconvolution)

(8) Jump to (1)

* Optional - determined by switch register.

REFERENCES

1. see e.g. O.W. RICHARDSON and C.B. BAZZONI, Phil.Mag., 42, 1015 (1921)

2. C.H. THOMAS, Phys.Rev., 16, 739 (1925)

3. H.W.B. SKINNER, Proc.Roy.Soc., 135A, 84 (1932)

4. R.L. PARK, J.E. HOUSTON and D.G. SCHREINER, Rev.Sci.Inst., 41, 1810 (1970)

5. R.L. PARK and J.E. HOUSTON, Surf.Sci., 26, 664 (1971)

6. R.G. MUSKET and S.W. TAATJES, J.Vac.Sci.Tech., 9, 1041 (1972)

7. J.C. TRACY, J.Appl.Phys., 43, 4164 (1972)

8. J.E. HOUSTON and R.L. PARK, J.Chem.Phys., 55, 4601 (1971)

9. D.C. LANGRETH, Phys.Rev.Lett., 26, 1229 (1971)

10. G.E. LARAMORE, Phys.Rev.Lett., 27, 1050 (1971)

11. G.E. LARAMORE, Sol.St.Comm., 10, 85 (1972)

12. J.A. WILSON and A.D. YOFFE, Adv. in Phys., 18 193 (1969)

13. A.D. YOFFE, Adv. in Solid State Phys., 13, 1 (1973)

14. C. WEBB, M.Sc., Imperial College (1973)

15. K.J. CLOSE and J. YARWOOD, Vacuum, 22, 45 (1972)

16. J.E. HOUSTON and R.L. PARK,
Sol.St.Comm., 10, 91 (1972)

17. A.M. BRADSHAW and D. MENZEL,
Phys.Stat.Sol., 56, 135 (1973)

18. C.N. BERGLUND and W.E. SPICER,
Phys.Rev., 136, A1030 (1964)

19. R.L. PARK and J.E. HOUSTON,
J.Vac.Sci.Tech., 11, 1 (1974)

20. R.D. EVANS,
The Atomic Nucleus (McGraw-Hill)

21. A.M. BRADSHAW,
Surface and Defect Properties of Solids,
Vol. 4 (Chemical Society, London, 1974)

22. e.g. P.T. MATTHEWS,
'Introduction to Quantum Mechanics',
(McGraw-Hill)

23. E.O. KANE,
Phys.Rev., 159, 624 (1967)

24. R.F. WILLIS, B. FITTON and G.S. PAINTER,
Phys.Rev.B, 9, 1926 (1974)

25. E. BAUER,
Z.Physik, 224, 19 (1969)

26. D.W. LANGER,
Adv. in Solid State Phys., 13, 193 (1973)

27. F.R. SHEPHERD and P.M. WILLIAMS,
J.Phys.C, 7, 4416 (1974); ibid 4427

28. R.R. TURTLE and R.J. LIEFELD,
Phys.Rev.B, 7, 3411 (1973)

29. N.J. SHEVCHIK,
Phys.Rev.Lett., 33, 1336 (1974)

30. S. HUFNER and G.K. WERTHEIM,
Phys.Rev.B, 11, 678 (1975)

31. N.H. MARCH,
in Band Structure Spectroscopy of Metals and Alloys,
ed. D.J. FABIAN and L.M. WATSON (Academic Press)

32. L. HEDIN,
in X-ray Spectroscopy,
ed. L.V. AZAROFF (McGraw-Hill)

33. M.J. STOTT and N.H. MARCH,
in Soft X-ray Band Spectra,
ed. D.J. FABIAN (Academic Press)

34. J.A. CATTERALL and J. TROTTER,
Phil.Mag., 3, 1424 (1958)

35. B. SCHIFF,
Proc.Phys.Soc., A67, 2 (1954)

36. R.L. PARK, J.E. HOUSTON and G.E. LARAMORE,
Jap.J.Appl.Phys., Supp.2, Part 2 (1974)

37. G.D. MAHAN,
Phys.Rev., 163, 612 (1967)

38. P. NOZIERES and C.T. dE DOMINICIS,
Phys.Rev., 178, 1079 (1969)

39. H.W.B. SKINNER,
Phil.Trans.Roy.Soc. London, A239, 95 (1940)

40. S. HANZELEY and R.J. LIEFELD,
National Bureau of Standards,
Spec.Pub. No. 323, p. 319 (1971)

41. R.J. LIEFELD, A.F. BURR and M.B. CHAMBERLAIN,
Phys.Rev.A, 9, 316 (1974)

42. M.B. CHAMBERLAIN, A.F. BURR, and R.J. LIEFELD,
Phys.Rev.A., 9, 663 (1974)

43. e.g. C. KITTEL,
Introduction to Solid State Physics (Wiley)

44. A.M. BRADSHAW and W. WYROBISCH,
J.Elec.Spec. and Rel.Phen., 7, 45 (1975)

45. A.M. BRADSHAW, S.L. CEDERBAUM, W. DOMCKE and U. KRAUSE,
J.Phys.C., 7, 4503 (1974)

46. W.Y. LIANG and S.L. CUNDY,
Phil. Mag., 19, 1031 (1969)

47. S. ANDERSSON, H. HAMMARQVIST and C. NYBERG,
Rev.Sci.Inst., 45, 877 (1974)

48. S. ANDERSSON and C. NYBERG,
Surf.Sci., (To be published)

49. W.L. BAUN, M.B. CHAMBERLAIN and J.S. SOLOMON,
Rev.Sci.Inst., 44, 1419 (1973)

50. J.E. HOUSTON and R.L. PARK,
Phys.Rev.B, 5; 3808 (1972)

51. J.E. HOUSTON, R.L. PARK and G.E. LARAMORE,
Phys.Rev.Lett., 30, 846 (1973)

52. J. KIRSCHNER and P. STAIB,
Phys.Lett., 42A, 335 (1973)

53. P. STAIB and J. KIRSCHNER,
Appl.Phys., 6, 99 (1975)

54. W.E. HARTE, P.S. SZCZEPANEK and A.J. LEYENDECKER
Phys.Rev.Lett., 33, 86 (1974)

55. J.J. VRAKKING and F. MEYER,
Phys.Rev.A., 9, 1932 (1974)

56. E.J. McGUIRE,
Phys.Rev.A., 3, 587 (1971)

57. E.J. McGUIRE,
Phys.Rev.A., 5, 1043 (1972)

58. J.C. TRACY,
Appl.Phys.Lett., 19, 353 (1971)

59. R.G. MUSKET,
J.Vac.Sci.Tech., 9, 603 (1972)

60. D.M. WARD,
(Private Communication)

61. R.L. PARK,
Surf.Sci., 48, 80 (1975)

62. R.L. PARK, J.E. HOUSTON and D.G. SCHREINER,
J.Vac.Sci.Tech., 9, 1023 (1972)

63. R.L. PARK and J.E. HOUSTON,
Phys.Rev.B., 6, 1073 (1972)

64. J.A. BEARDEN and A.F. BURR,
Rev.Mod.Phys., 39, 125 (1967)

65. J.E. HOUSTON, R.L. PARK and G.E. LARAMORE,
Phys.Rev.Lett., 30, 846 (1973)

66. C. WEBB and P.M. WILLIAMS,
Phys.Rev.Lett., 33, 824 (1974)

67. G. ERTL and K. WANDELT,
Surf.Sci., 50, 479 (1975)

68. J.E. HOUSTON and R.L. PARK,
Electron Spectroscopy
ed. D.A. SHIRLEY, p. 895 (1972)

69. S. ANDERSSON and C. NYBERG,
Sol.St.Comm., 15, 1145 (1974)

70. G. ERTL and K. WANDELT,
Z. Naturforsch, 29a, 768 (1974)

71. D. ADLER and J. FEINLEIB,
Phys.Rev.B., 2, 3112 (1970)

72. P.O. NILSSON and J. KANSKI,
Surf.Sci., 37, 700 (1973)

73. G. STEPHENSON,
Mathematical Methods, P.168 (Longmans)

74. M.B. CHAMBERLAIN and W.L. BAUN,
J.Vac.Sci.Tech., 11, 441 (1974)

75. M.S. MURTHY and P.A. REDHEAD,
J.Vac.Sci.Tech., 11, 837 (1974)

76. R.J. SMITH, M. PIACENTI and D.W. LYNCH,
Phys.Rev.Lett., 34, 476 (1975)

77. P.S. SZCZEPANEK and W.E. HARTE,
Phys.Lett., 49A, 377 (1974)

78. J. SUGAR,
Phys.Rev.B., 5, 1785 (1972)

79. P.O. NILSSON, J. KANSKI and G. WENDIN,
Sol.St.Comm., 15, 287 (1974)

80. G. WENDIN,
Phys.Lett., 46A, 119 (1973)

81. R.L. PARK and J.E. HOUSTON,
Phys.Rev.A., 7, 1447 (1973)

82. D. CHADWICK,
(Private Communication)

83. P. PAATERO, S. MANNINEN and T. PAAKKARI,
Phil.Mag., 30, 1281 (1974)

84. A.F. JONES and D.L. MISELL,
Brit.J.Appl.Phys., 18, 1479 (1967)

85. J.J. LANDER,
Phys.Rev., 91, 1382 (1953)

86. H.D. HAGSTRUM,
J.Vac.Sci.Tech., 12, 7 (1975)

87. H.D. HAGSTRUM and G.E. BECKER,
Phys.Rev.B., 4, 4187 (1971)

88. e.g. S. ERGUN,
J.Appl.Cryst., 1, 19 (1968)

89. K. TAYLOR,
Astrosphysics and Space Science, 26, 327 (1974)

90. C. WEBB and P.M. WILLIAMS,
Phys.Rev.B., 11, 2082 (1975)

91. F.R. SHEPHERD,
Ph.D. Thesis, Imperial College (1975)

92. R.F. FRINDT,
Phys.Rev.Lett., 28, 299 (1972)

93. F.R. GAMBLE, J.H. OSIECKI, M. CAIS, R. PISHARODY,
F.J. DISALVO, T.H. GEBALLE,
Science, 174, 493 (1971)

94. H.E. BARZ et al.,
Science, 175, 884 (1972)

95. W.B. CLARK and P.M. WILLIAMS,
Phil.Mag., (To be published)

96. C.B. SCRUBY, P.M. WILLIAMS and G.S. PARRY,
Phil.Mag., 31, 255 (1975)

97. A.D. YOFFE,
Ann.Rev.Mat.Sci., 3, 147 (1973)

98. W.B. CLARK,
(Private Communication)

99. B.N. FIGGIS,
Introduction to Ligand Fields (Interscience)

100. L.F. MATTHEIS,
Phys.Rev.B., 8, 3719 (1973)

101. H.W. MYRON and A.J. FREEMAN,
Phys.Rev.B., 9, 481 (1974)

102. P.M. WILLIAMS and F.R. SHEPHERD,
J.Phys.C., 6, L36 (1973)

103. P.M. WILLIAMS,
(Private Communication)

104. D.W. FISCHER,
Phys.Rev.B., 8, 3576 (1973)

105. B. SONNTAG and F.C. BROWN,
Phys.Rev.B., 10, 12 (1974)

106. G. LEVEQUE, S. ROBIN-KANDARE and L. MARTIN,
Phys.Stat.Sol.(b)., 63, 679 (1974)

107. R.B. MURRAY, R.A. BROMLEY and A.D. YOFFE,
J.Phys.C., 5, 746 (1972)

108. R.G. MURRAY and A.D. YOFFE,
J.Phys.C., 5, 3038 (1972)

109. P.R. WALLACE,
Phys.Rev., 71, 622 (1947)

110. J.C. SLONCZEWSKI and P.R. WEISS,
Phys.Rev., 109, 272 (1958)

111. R. TAYLOR and C.A. COULSON,
Proc.Phys.Soc., A65, 834 (1952)

112. G.S. PAINTER and D.E. ELLIS,
Phys.Rev.B., 1, 4747 (1970)

113. A. ZUNGER,
J.Phys.C., 7, 96 (1974)

114. R.F. WILLIS, B. FEUERBACHER and B. FITTON,
Phys.Lett., 34A, 231 (1971)

115. R.F. WILLIS, B. FEUERBACHER and B. FITTON,
Phys.Rev.B., 4, 2441 (1971)

116. F.R. SHEPHERD and P.M. WILLIAMS,
'Vacuum Ultraviolet and Radiation Physics',
ed. E.E. KOCH ET AL. (Pergamon/Vieweg), p.508 (1974)

117. D.L. GREENAWAY, G. HARBEKE, F. BASSANI and E. TOSATTI,
Phys.Rev., 178, 1340 (1969)

118. P.M. WILLIAMS, D. LATHAM and J. WOOD,
J.Elec.Spec. and Rel.Phen., 7, 281 (1975)

119. K. ZEPPENFELD,
Z.Phys., 211, 391 (1968)

120. J. VERHOEVEN and J. KISTEMAKER,
Surf.Sci., 50, 388 (1975)

121. V.E. HENRICH,
Phys.Rev.B., 7, 3512 (1973)

122. C. WEBB and P.M. WILLIAMS,
Warwick Surface Science Conference, (March 1975),
Proceedings to be published:
Surf.Sci., 54, (1976)

123. A.M. BRADSHAW and U. KRAUSE,
Ber Bunsenges (in press)

124. J.E. HOUSTON,
Sol.St.Comm. (in press)